Doctoral Theses at NTNU 2004:159

Wibeke Nordhøy

Manganese and the heart

Intracellular MR relaxation and water exchange across the cardiac cell membrane

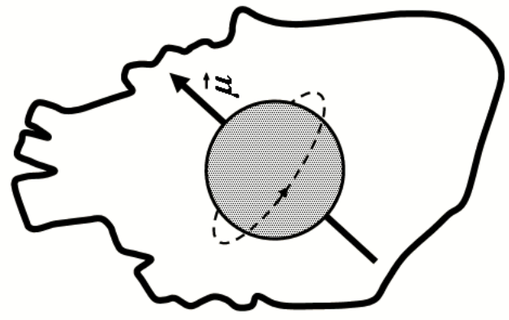

NTNU
Norwegian University of
Science and Technology
Doctoral thesis
for the degree of philosophiae doctor
Faculty of Medicine
Department of Circulation and
Medical Imaging

Wibeke Nordhøy

Doctoral thesis 2004:159

NTNU

ISBN 82-471-6548-1 (printed ver.)
ISBN 82-471-6547-3 (electronic ver.)
ISSN 1503-8181

MANGANESE AND THE HEART

Intracellular MR relaxation and water exchange across the cardiac cell membrane

PhD Thesis
in Medical Technology
by
Wibeke Nordhøy

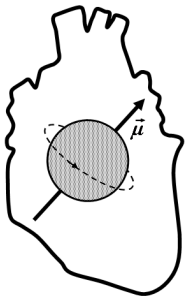

Department of Circulation and Medical Imaging
The Norwegian University of Science and Technology

20th July 2004

Acknowledgements

This work was carried out during the years 2000-2004 at the Department of Circulation and Imaging, Faculty of Medicine, the Norwegian University of Science and Technology (NTNU).

In 1999 when I worked on my Diploma thesis at the Department of Circulation and Imaging I was offered to start on a PhD in a new discipline and a heart physiology group headed by professor Per Jynge at the same department. I was fascinated by the idea of working in a multidisciplinary environment with heart physiology, contrast agents and MR technology. These past 4.5 years I have learned the challenges and advantages of working interdisciplinary. Per Jynge, who has been my supervisor, is an enthusiastic researcher and a warm person with a passionate interest for classical music, always full of scientific ideas and from whom I have learned the most. The other people who have been the main resources in this process are professor Jostein Krane from the Department of Chemistry, with whom I have had many interesting meetings, and who has supported me and believed in our project through the whole process. In the end he has been supervising me through my ambitious writing process. Henrik W. Anthonsen, an experienced analytical MR chemist, with whom I have had interesting and fruitful discussions and who has trusted me with a great deal of his knowledge and been a good friend. Morten Bruvold, who is a very handy person to have in the lab and who has been working together with me through most of my years in the lab, where we had friendly and professional discussions. Heidi Brurok, gave me theoretical support and supervision, especially in the writing process. Our research technician, Sissel Skarra, an experienced, skilful and tidy person in the lab with a special interest in opera, which I also have learned to love. Siri Garnes, a girl with lots of energy and who was cheerful to work with in the lab. Kirsti Berg, with whom I have shared office, together we have had many laughs and supported each other scientifically and through difficult times. I will acknowledge the people at the MR center, where I did some of my experiments together with Abdel Bidar and Olav Haraldseth. Arne Skjold, John Georg Seland and Geir Sørland are also people who have been friendly and supportive to me. Also, I would like to thank all the people at the Ultrasound group and in GE Vingmed Ultrasound for their friendly company, whom I have known since 1998.

The last 10 years, that is, almost my whole grown up life, I have lived in "trivelige" Trondheim studying at the University. During these years I have learned to know many nice people, both through my active speartime (Studentersamfundet, the Trønderopera choir, the Lindy Hop and Flamenco dance groups) and through my studies. All of these people have in a way contributed to my success of achieving first a Sivilingeniør degree in Biophysics and now probably a PhD in Medical Technology. I will never forget my life in Trondheim as I now have decided to move closer to my family nearby Oslo

again. Also, my aunt and her family, who have lived in Trondheim during all these years, have supported me both with invitations to nice Sunday dinners, a "family life" and good conversations.

I will also give a special thanks to all the people in the 5th floor at MTFS for nice lunch and coffee breaks. Thank you Olga Maltseva, Fekadu Yadetie, Anita Øren, Mari Gårseth, Cathrine Broberg Vågbø, Espen Remme, Sigve Hovda and Bjarne Bergheim for nice lunches and friendship at MTFS.

And last but not least I will give thanks to my family Inger, Bjørn and Kristin Nordhøy, who know how to appreciate a good conversation. They have lifted me up whenever I have had tough periods in my private or student life, and always supported and believed in me. A warm thanks to my grandparents, Bjarnhild Nordhøy, Ingeborg and Andreas Dyb, with whom I also appreciate a good conversation and whose experiences in life are valuable to me. Finn Arne Gangstad, who has given me skilled computer support and comforted me through this long and demanding period of writing.

I would also like to acknowledge three years of financial support from The research council of Norway (NFR), and one and a half year of financial support from the Department of Circulation and Imaging, the Medical Faculty, NTNU.

Thank you Trondheim!

July, 2004. Wibeke Nordhøy

Symbols and Abbreviations

ic	intracellular: inside the cells
ec	extracellular: interstitium and intravascular space
ρ	correlation coefficient
R^2	regression coefficient
χ^2/D_{0F}	reduced chi-square coefficient, where D_{0F} is the degree of freedom
σ, SD	standard deviation
J	spin or angular momentum
$\vec{\mu}$	individual dipole moment
S or I	electron or proton spin quantum number
γ	the gyromagnetic ratio
$h = \hbar \cdot 2\pi$	Planck's constant
ν_0	resonance or Larmor frequency in Hz
ω_0	resonance or Larmor frequency in rad/s
$\vec{B}_0 = B_0\hat{z}$	static magnetic field
$\vec{M} = M_0\hat{z}$	macroscopic net magnetization vector
$\hat{x}$, $\hat{y}$, $\hat{z}$	unit vectors
M_x, M_y, M_z	magnetization components of $\vec{M}$
M_0	Boltzmann equilibrium value
B_{eff}	effective field
RF	radio frequency
B_1	RF field
ω_1	precessional frequency that generates the RF field
xyz-plane	laboratory frame of reference
x′y′z-plane	rotating frame of reference
Θ	flip or pulse angle
ϕ	phase angle
$M_z(t)$	instantaneous longitudinal magnetization
M_{xy}(t)	instantaneous transversal magnetization
FID	free induction decay
n_s	number of scans
TR	relaxation delay, the waiting time between the pulse sequences in relaxography experiments
A_t	signal acquisition time
SNR	signal to noise ratio
TI	inversion time, the time constant in IR experiments between the 180° and 90° pulses. For SR experiments the time between the 90° and 90° pulses is named t
SR	Saturation Recovery T_1 experiment
IR	Inversion Recovery T_1 experiment

α	correction factor for deviation from a perfect 180° pulse
$M_+(t)$	complex representation of the transverse magnetization
TE	echo time, the time between the initial 90° pulse and the echo in a CPMG experiment
SE	Spin Echo T_2 experiment
$CPMG$	Carr-Purcell-Meiboom-Gill T_2 experiment
T_1	longitudinal (spin-lattice) relaxation time constant
$R_1 = 1/T_1$	longitudinal relaxation rate constant
T_2	transversal (spin-spin) relaxation time constant
$T_2^\star$	time constant for decay of the free induction decay signal in presence of magnetic field inhomogeneity
$R_2 = 1/T_2$	transversal relaxation rate constant
τ_c	correlation time
CA	paramagnetic contrast agent
r	the effectiveness of the contrast agent to reduce T_1 and T_2 as a function of its concentration
M	metal or paramagnetic ion
P_M	mole fraction of metal (M) ion
T_M	relaxation time of the bound water protons
τ_M	residence lifetime of the bound water on the paramagnetic ion
q	number of water molecules bound per metal ion
T_{1e}	electron spin relaxation time constant
IS	inner-sphere
OS	outer-sphere
$\Delta\omega$	the chemical shift difference between the paramagnetic complex and a diamagnetic reference
ω_I and ω_s	Larmor frequencies for nuclear and electron spin
τ_{ci} and τ_{ei}	correlation times for dipolar and scalar interactions
g	electronic Landé factor for the free electron
β	Bohr magneton
$A/\hbar$	electron-nuclear hyperfine coupling constant
τ_R	correlation time of rotation
NMRD	nuclear magnetic resonance dispersion
LVDP	left ventricular developed (systolic-diastolic) pressure
HR	heart rate

Apparent values:

Intracellular:

T_{1-1} or T'_{1ic}	longitudinal relaxation time constant
R_{1-1} or R'_{1ic}	longitudinal relaxation rate constant
T_{2-1}	transversal relaxation time constant
R_{2-1}	transversal relaxation rate constant
p_{01} or p'_{ic}	population fraction

Extracellular:

T_{1-2} or T'_{1ec}	longitudinal relaxation time
R_{1-2} or R'_{1ec}	longitudinal relaxation rate constant
T_{2-2}	transversal relaxation time
R_{2-2}	transversal relaxation rate constant
p_{02} or p'_{ec}	population fraction

Intrinsic values:

R_{1ec}	ec relaxation rate constant
r_{1ic}	ic relaxivity
R_{1ic0}	ic relaxation rate constant at $[CA]$=0 nmol/g dry wt.
τ_{ic}	ic lifetime
τ_{ec}	ec lifetime
p_{ic}	ic population fraction
p_{ec}	ec population fraction

Physiological test substances:

$MnCl_2$	manganese chloride
MnDPDP	manganese dipyridoxyl diphosphate
Manganese	$MnCl_2$ and gluconate
Manganese-Calcium	$MnCl_2$ and gluconate and $CaCl_2$ with a 1 Mn^{2+}:10 Ca^{2+} ratio
$CuSO_4$	copper sulphate

List of Papers

I. Nordhøy W, Anthonsen HW, Bruvold M, Jynge P, Krane J and Brurok H. Manganese ions as intracellular contrast agents: Proton relaxation and calcium interactions in rat myocardium. NMR in Biomedicine 16(2):82-95 (2003).

II. Nordhøy W, Anthonsen HW, Bruvold M, Brurok H, Skarra S, Krane J and Jynge P. Intracellular manganese ions provide strong T_1 relaxation in rat myocardium. Magnetic Resonance in Medicine 52:506-514 (2004).

III. Bruvold M*, Nordhøy W*, Anthonsen HW, Brurok H, and Jynge P. Manganese-calcium interactions with contrast media for cardiac MRI: A study of manganese chloride supplemented with calcium gluconate in isolated guinea pig hearts. Investigative Radiology, Accepted after revision.

*These two main authors have contributed equally to the study.

Contents

1. Clinical and diagnostic background

1.1 Ischemic heart disease and heart failure

Ischemic heart disease (IHD) with secondary heart failure is still the number one cause of death in the industrialized world. Atheromatosis, the underlying basic pathology in the coronary vessel wall, is characterized by lipid deposits, inflammation and formation of plaques that in the course of time may narrow coronary arteries. Acute coronary events may occur with rupture of vulnerable plaques or thrombosis at stenotic and endothelial-deficient points in the arterial tree. Accordingly, blood flow to the heart muscle (myocardium) may fall either gradually or abruptly. The accompanying regional ischemia, i.e. local imbalance between oxygen supply and oxygen demand, may be moderate for a long period of time and become symptomatic as angina pectoris. Another manifestation is hibernating myocardium [85] where the cardiac workload is reduced to match the low blood flow. If ischemia becomes severe due to closure of a coronary artery, myocardial infarction ensues with arrhythmias and with loss of contractile function and cell viability [4].

Cell death can be prevented if blood flow is restored by coronary interventions, thrombolysis or coronary bypass grafting before or early during severe ischemia. When such attempts at reperfusion are successful, injury and repair processes may still require some time before a full recovery to normal contractile function is obtained. This condition is called stunning [80], which indicates a reversible postischemic dysfunction of the myocardium. If reperfusion is unsuccessful or is not performed, the myocardium may, parallel to the loss of viable cells, undergo structural changes which with time leads to remodeling of the entire left ventricular wall [8]. The end result may be progressive contractile dysfunction and overt heart failure [8] with a high mortality rate. Whereas, the immediate consequences of myocardial ischemia have been lessened in some groups of patients due to changes in lifestyle, diagnosis and treatment, the loss of active cardiac cells (cardiomyocytes) and secondary heart failure remains an unsolved challenge in cardiology. Within an aging population IHD and associated heart failure represents a major challenge both to the health service and to the society.

1.2 Diagnostic imaging of the heart

The above scenario underlines a demand for diagnostic imaging to identify IHD in its different stages and forms. Also there is a need to diagnose heart failure developing after myocardial infarction, to identify other forms of heart failure, and to monitor the efficacy of drug treatment. The main overall infor-

mation needed is related to: pathology of the arterial wall; morphology of the coronary arteries (angiography); gross cardiac morphology; regional contractile function; myocardial perfusion and viability of cardiac cells.

Diagnostic imaging has developed greatly in the last decades from originally giving only morphological information to now also giving physiological information [8]. This has been accompanied by the development of new diagnostic modalities such as nuclear medicine, ultrasound and magnetic resonance (MR) imaging (MRI). At the same time x-ray examinations have been refined. At present neither modality can cover the whole spectrum of diagnostic needs. Thus x-ray has its main role as the tool of choice for coronary angiography. Ultrasound has its advantage in the study of cardiac morphology, intracardiac blood flow and regional contractile function and can be applied for bedside examinations. Nuclear medicine is mainly applied in the study of myocardial perfusion and in assessment of myocardial viability.

MRI as the youngest, less than 30 years old, of present modalities is perhaps the most promising tool by its overall versatility in free choice of image sections and in modifying resonances from excited protons. Thus it was stated in a recent review that "MRI accurately depicts cardiac structure, function, perfusion and myocardial viability with a capacity unmatched by any other single imaging modality" [34]. A detailed discussion of clinical possibilities with cardiac MRI [45] is beyond the scope of the present thesis, which deals with cell MR chemistry and biophysics in the myocardium and with the development of a new contrast principle based on the use of intracellular paramagnetic manganese. These two topics are therefore covered in more detail below.

2. MR theory and methodology

MRI is a nonionizing, noninvasive imaging technique primarily used in a medical setting to produce high quality images of the inside of the human body. The technique is based on the principles of nuclear magnetic resonance (NMR), a spectroscopic technique used by scientists to obtain microscopic chemical and physical information about molecules. The term nuclear has not been used since the late 1970's because of the negative connotation associated with this word. MR is based on fundamental properties inherent in the atoms, which can be described by quantum physics. A semiclassical description, that is, a combination of a microscopical view (spin quantum physics) and a macroscopical view (Newtonian physics), is common to use when describing the concept of MR, as outlined in this section [41, 43].

The theory in Section 2.1 and 2.2 is taken from the books of Farrar (1987) [36], Hashemi and Bradley (1997) [43] and of Haacke *et al.* (1999) [41].

2.1 MR theory

Spin is a fundamental property of nature like electrical charge or mass, that comes in multiples of 1/2 and can be negative or positive. Protons, electrons, and neutrons each possess a spin or angular momentum (J) of 1/2. In MR, it is unpaired nuclear spins that are of importance, a property belonging to certain atomic nuclei (see Table 2.1).

Table 2.1: List of selected nuclear species with their spins and their relative body abundances (1 M = 1 mol/liter).

Nucleus	**Spin**	**Abundance in human body**
Hydrogen ^{1}H	1/2	88 M
Sodium ^{23}Na	3/2	80 mM
Phosphorus ^{31}P	1/2	75 mM
Oxygen ^{17}O	5/2	16 mM
Fluorine ^{19}F	1/2	4 μM

Unpaired nuclear spins have an odd numbers of protons and/or neutrons, which do not *pair up* and cancel out each other so that their individual dipole moment ($\vec{\mu}$) becomes zero as in Figure 2.1.

$$\vec{\mu} = \gamma \vec{J} \neq 0 \tag{2.1}$$

where γ the gyromagnetic ratio intrinsic to each type of nucleus.

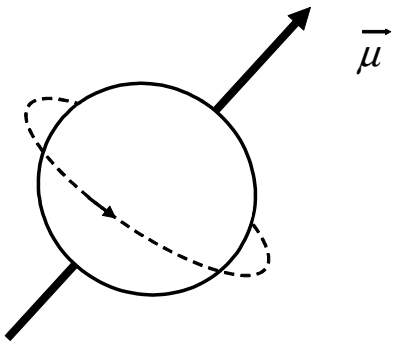

Figure 2.1: A spinning top.

In the absence of an external magnetic field the dipole moments are randomly oriented (Figure 2.2 a) and the vector sum of their magnetic moments is zero:

$$\vec{M} = \frac{1}{V} \sum_{\substack{\text{dipole} \\ \text{moments} \\ \text{in V}}} \vec{\mu}_i = 0 \tag{2.2}$$

where V is a volume element that contains a large number of protons.

In the presence of a static magnetic field, $\vec{B}_0 = B_0\hat{z}$, the moments become oriented along the direction of $\vec{B}_0$ (Figure 2.2 b). Each atomic nuclei has a specific energy level related to the property of the spin quantum number I (S for electrons), where number of energy levels equals $2I+1$. The hydrogen nucleus, with a spin quantum number I of 1/2, has two allowable energy levels that are aligned in opposite directions, either "parallel" or "antiparallel" to $\vec{B}_0$ corresponding to a low and a high energy state, respectively. Planck's law defines the energy difference between the two levels:

$$\Delta E = h\nu_0 = \hbar\nu_0 2\pi = \gamma\hbar B_0 \tag{2.3}$$

where $h = \hbar \cdot 2\pi$ is Planck's constant and ν_0 is the resonance or Larmor frequency in Hz.

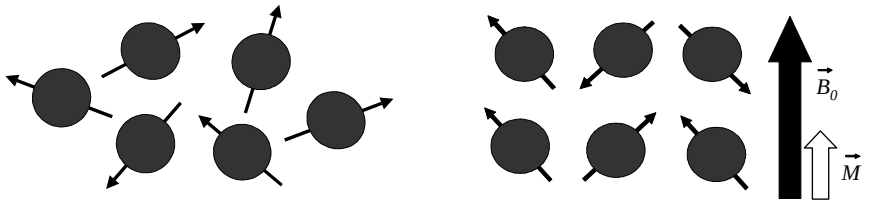

(a) (b)

Figure 2.2: Application of an external magnetic field, $\vec{B}_0$: (a) Randomly distributed spins without $\vec{B}_0$, (b) Spins aligned with the external field.

Since the parallel state is the state of lower energy, slightly more dipole moments reside in the parallel configuration. This net excess of parallel moments is represented by the macroscopic net magnetization vector, $\vec{M} = M_0\hat{z}$, where $\hat{z}$ is a unit vector (Figure 2.2 b). Since this is a macroscopic view it is important to remember that to be 'oriented along $\vec{B}_0$' does not mean that the direction of $\vec{\mu}$ for individual nuclei is collinear with $\vec{B}_0$. Rather, the nuclei precess about an axis that is collinear with $\vec{B}_0$. This phenomenon is due to the angular momentum that the nuclei possess. The combination of nuclear magnetic moment and angular momentum cause the nuclei to precess about $\vec{B}_0$ in much the same way as a rotating top precesses about the earth's gravitational field:

$$\frac{d\vec{\mu}}{dt} = \gamma\frac{d\vec{J}}{dt} = \gamma(\vec{\mu} \times \vec{B}_0) \tag{2.4}$$

Equation 2.4 tells us that the rate at which the nuclei precess in a magntic field is dependent on both the magntiude of $\vec{\mu}$ and $\vec{B}_0$. In any particular MR experiment their magnitudes are constant, i.e. the macroscopic magnetic moment ($\vec{M}$) will precess at a constant frequency about the direction of the magnetic field. This can be expressed as:

$$\frac{d\vec{\mu}}{dt} = \vec{\omega}_o \times \vec{\mu} = \gamma(\vec{\mu} \times \vec{B}_0) \tag{2.5}$$

Hence,

$$\vec{\omega}_0 = 2\pi\vec{\nu}_0 = -\gamma\vec{B}_0 \tag{2.6}$$

where $\vec{\omega}_0$ or $\vec{\nu}_0$ is the resonance frequency in radians per seconds or Hz, respectively. Equation 2.6 is called the Larmor equation. For hydrogen, $\gamma\!\!\!^{-} \equiv \gamma/2\pi$ = 42.58 MHz / T. That is, with a magnetic field of 0.47 T, the frequency is 20 MHz.

To keep the model as simple as possible two simplifications are used. Because it is difficult to be concerned with the motion of all the individual microscopic magnetic moments, the macroscopic view was introduced. Furthermore a rotating frame of reference will be introduced. Thus the motion of the magnetization is referred to a coordinate system that rotates about $\vec{B}_0$ in the same direction in which the nuclear moments precess, rather than the fixed coordinate system of the laboratory. This is called the rotating frame.

To derive the basic equation of the rotating frame, a simple and well-known result for the time derivative of a vector $\vec{M}$ in terms of its components will be presented. The vector $\vec{M}$ can be expressed as:

$$\vec{M} = \hat{x}M_x + \hat{y}M_y + \hat{z}M_z \tag{2.7}$$

After derivation of $\vec{M}$ with respect to time, the final expression will look like this:

$$\begin{aligned} \left(\frac{d\vec{M}}{dt}\right)_{fixed} &= \frac{\partial \vec{M}}{\partial t} + \vec{\omega} \times (\hat{x}M_x + \hat{y}M_y + \hat{z}M_z) \\ &= \left(\frac{\partial \vec{M}}{\partial t}\right)_{rot} + \vec{\omega} \times \vec{M} \end{aligned} \tag{2.8}$$

The total derivate represents the overall motion of $\vec{M}$ in the fixed (laboratory) frame, whereas the partial derivate represents the explicit dependence of $\vec{M}$ on time in the rotating frame. If $\vec{M}$ represents the magnetization vector, then from Equation 2.4:

$$\left(\frac{d\vec{M}}{dt}\right)_{fixed} = \gamma \vec{M} \times \vec{B} \tag{2.9}$$

and from Equation 2.8:

$$\left(\frac{d\vec{M}}{dt}\right)_{rot} = \gamma \vec{M} \times \vec{B} - \vec{\omega} \times \vec{M} \tag{2.10}$$

Rearranging terms in Equation 2.8 the following equation is obtained:

$$\left(\frac{d\vec{M}}{dt}\right)_{rot} = \gamma \vec{M} \times \left(\vec{B} + \frac{\vec{\omega}}{\gamma}\right) \tag{2.11}$$

where the term $\vec{\omega}/\gamma$ has the dimensions of a magnetic field and can be considered as a "fictitious" field that arises from the effect of the rotation. The field in Equation 2.11 is also referred to as the effective field:

$$\vec{B}_{eff} = \vec{B} + \frac{\vec{\omega}}{\gamma} \tag{2.12}$$

Equations 2.11 and 2.12 proves that the ordinary equations of motion applicable in the laboratory frame are valid in the rotating frame as well, provided $\vec{B}_{eff}$ is used in stead of $\vec{B}$. Thus, in the rotating frame, the magnetization precesses about $\vec{B}_{eff}$.

Now suppose, that in addition to $\vec{B}_0$ another field, $\vec{B}_1$, is applied perpendicular to $\vec{B}_0$ (i.e. in the x-y plane), and $\vec{B}_1$ rotates in the laboratory frame at ω (rad/s).

While $\vec{B}_0$ is a fixed magnetic field, the radio frequency (RF) field $\vec{B}_1$ is an oscillating magnetic field with a cos(ωt) wave form. Such an oscillating field can be treated as the sum of two fields rotating in opposite directions. Only the component rotating in phase with the nuclear precession has an effect on the magnetization vector. In the frame rotating at ω, the effective field becomes:

$$\vec{B}_{eff} = \vec{B}_0 + \frac{\vec{\omega}}{\gamma} + \vec{B}_1 \tag{2.13}$$

At resonance the fictitious field exactly cancels $\vec{B}_0$ ($\vec{\omega}$ = - $\gamma\vec{B}_0$) along the z-axis and leaves only $\vec{B}_1$ in the x-y plane to interact with $\vec{M}$:

$$\frac{d\vec{M}}{dt} = \gamma\vec{M} \times \vec{B}_1 \tag{2.14}$$

The rotating coordinate system is distinguished from the laboratory system by primes on the x- and y-axis, x′y′. Since $\vec{B}_1$ rotates at the same frequency as the frame, it can arbitrarily be assigned along the x′-axis. $\vec{M}$ will be 'flipped' about the x′-axis into the x′-y′ plane due to the applied $\vec{B}_1$ with at frequency given by:

$$\omega_1 = \gamma B_1 \tag{2.15}$$

Since $B_1 \ll B_0$, the precessional frequency ω_1 of $\vec{M}$ around the axis of $\vec{B}_1$ is much slower than the precessional frequency ω_0 of $\vec{M}$ around the axis of the external magnetic field $\vec{B}_0$. In a time τ (s) the flip or pulse angle Θ (rad) through which $\vec{M}$ precesses is given by:

$$\Theta = \gamma B_1 \tau \tag{2.16}$$

Once $\vec{M}$ is deflected, the RF field is switched off and the magnetization freely precesses about the main field, $\vec{B}_0$. After a $(\pi/2)_{-x'}$ or $90^\circ_{-x'}$ flip the magneti-

zation vector will end up in the x′-y′ plane, i.e. $\vec{M} = M_0\hat{y'}$ (from Figure 2.3 a to Figure 2.3 b). The subscript +/- x′ or +/- y′ on the RF pulses denotes the axis along which the pulse of RF energy is applied, i.e. the phase of the RF pulse. This is also commonly denotated by a phase angle, ϕ, where $\phi = 0$ corresponds to a rotation about the x′-axis. In Figure 2.3 c, a 180° RF pulse has been applied and induced a negative longitudinal magnetization vector $\vec{M} = -M_0\hat{z}$, where no transversal magnetization is present.

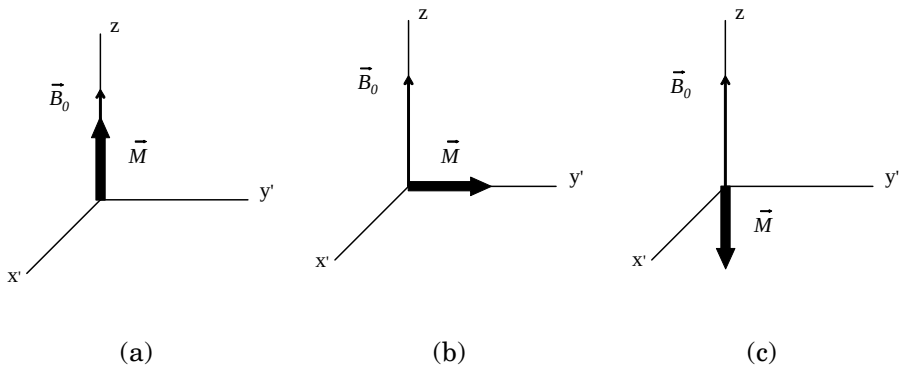

Figure 2.3: Position of the magnetization vector $\vec{M}$ (a) in the presence of a static field, $\vec{B}_0$, before application of an RF pulse, (b) immediately after a 90° pulse and (c) immediately after a 180° pulse.

If a receiver coil is aligned along the y′-axis the time dependent precession of $\vec{M}$ will, according to Faraday's law of induction, induce a current in the receiver coil. The resulting exponentially decaying voltage, referred to as the free induction decay (FID), constitutes the MR signal (Figure 2.4 a). Since precession occurs at the Larmor frequency, the resulting MR signal also has a frequency equal to the Larmor frequency (Figure 2.4 b).

Consequently, the Fourier Transform of the FID results in a frequency spectrum centered at ω_0 (Figure 2.5). According to Fourier transform theory, the area of the Fourier spectrum is equal to the initial magnitude of the FID and the initial magnitude of the FID is proportional to the number of nuclei in sample (or within the RF coil).

During the period of free precession the magnetization returns to its original equilibrium state by a process called relaxation characterized by two (intrinsic) time constants T_1 and T_2, which depend on certain physical and chemical characteristics of the sample.

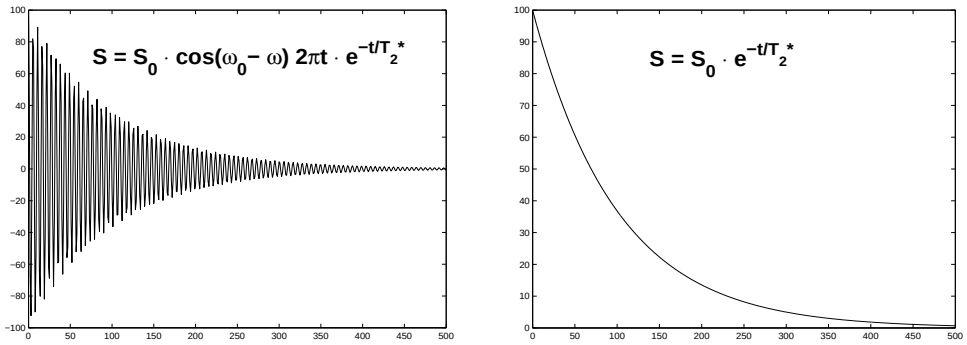

(a) (b)

Figure 2.4: The resulting FID signal: (a) out of resonance and (b) on resonance.

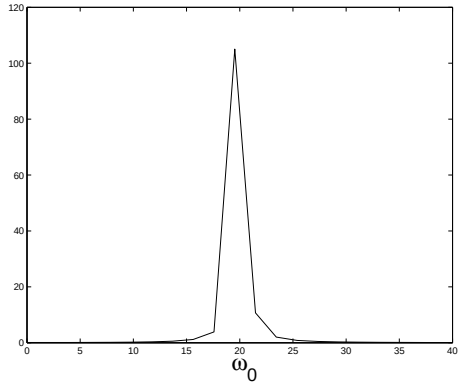

Figure 2.5: The Fourier transformed signal has a peak around ω_0 when on resonance.

2.2 T_1 and T_2 measurements

The two relaxation processes of T_1 and T_2 occur simultaneously only restriced by that the time constant T_2 being less than or equal to the time constant T_1, but they can be described and measured separately.

The Bloch equations are a set of coupled differential equations which can be used to describe the behavior of a magnetization vector under any conditions. When the Bloch equations are properly integrated, their solutions will yield the x, y, and z components of magnetization as a function of time.

Equation 2.9 can be expanded and expressed as individual vector components:

$$\frac{dM_x}{dt} = \gamma(M_y B_z - M_z B_y) \tag{2.17}$$
$$\frac{dM_y}{dt} = \gamma(M_z B_x - M_x B_z) \tag{2.18}$$
$$\frac{dM_z}{dt} = \gamma(M_x B_y - M_y B_x) \tag{2.19}$$

In a rotating frame of reference, which is common to use when describing the Bloch equations, Equation 2.9 is modified and expressed as in Equation 2.11. When a RF field $\vec{B}_1$, which is at rest in the rotating frame, is applied parallel to $\hat{x}'$, the resulting field $\vec{B}_{eff}$ in Equation 2.13 is $B_1\hat{x}'$. The components of spin magnetization are in-phase ($M_{x'}$) and out of phase ($M_{y'}$) with the RF-field, and parallel to the direction of the large static magnetic field (M_z). The component Bloch equations in the primed coordinates take the form:

$$\frac{dM_{x'}}{dt} = -\frac{M_{x'}}{T_2} \tag{2.20}$$
$$\frac{dM_{y'}}{dt} = \omega_1 M_z - \frac{M_{y'}}{T_2} \tag{2.21}$$
$$\frac{dM_z}{dt} = -\omega_1 M_{y'} + \frac{M_0 - M_z}{T_1} \tag{2.22}$$

2.2.1 T_1 relaxation time

At thermal equilibrium or before a RF pulse is introduced, the protons precess about the z-axis but they are *out of phase* and hence have no net transverse component. In this configuration (Figure 2.3 a), the z component of magnetization is $\vec{M} = M_z\hat{z} = M_0\hat{z}$. Introducing a RF pulse to the system causes the spins to begin precessing *in phase* with each other. After a $\pi/2$ pulse the vector sum of the in phase precessing protons lies in the x′-y′ plane (Figure 2.3 b). When the RF pulse is turned off the spins will return to the lowest energy state, but they will also get out of phase with each other.

M_z will recover to its equilibrium value, M_0, governed by the longitudinal relaxation time constant T_1. This is also called the spin-lattice relaxation time, because in order to go back to the equilibrium state the energy obtained from the RF pulse will be transfered to the surrounding lattice.

To find the equation governing the T_1 relaxation behavior, the first-order differential equation $dM_z(t)/dt$ in Equation 2.22 has to be solved. When the RF pulse is turned off, $\omega_1 = 0$:

$$\int \frac{dM_z(t)}{(M_0 - M_z(t))} = \int \frac{1}{T_1} dt \Rightarrow -ln(M_0 - M_z(t)) = \frac{1}{T_1} t + C \tag{2.23}$$

By use of $t = 0 \Rightarrow C = ln(M_0 - M_z(0))$ the following general T_1 function can be written:

$$M_z(t) = M_z(0) e^{\frac{-t}{T_1}} + M_0 (1 - e^{\frac{-t}{T_1}}) \tag{2.24}$$

If the net magnetization is placed along the y′-axis (Figure 2.3 b), it will gradually return to its equilibrium position along the +z-axis at a rate governed by T_1. By setting $M_z(0) = 0$ in Equation 2.24; M_z as a function of the time t after its displacement is:

$$M_z(t) = M_0 (1 - e^{\frac{-t}{T_1}}) \tag{2.25}$$

The time constant T_1 is defined as the time it takes for M_0 to recover with 63 %, i.e. $M_z(T_1) = M_0(1 - e^{-1})$.

If the net magnetization is placed along the -z axis (Figure 2.3 c), it will gradually return to its equilibrium position along the +z axis at a rate governed by T_1. This equation can be derived from the same Bloch equation as with Equation 2.25, but with the boundary condition: $M_z(0) = -M_0$; the equation governing this behavior M_z as a function of t is:

$$M_z(t) = M_0 (1 - 2 \cdot e^{\frac{-t}{T_1}}) \tag{2.26}$$

The pulse sequences saturation recovery (*SR*) and inversion recovery (*IR*) have been used to measure the longitudinal relaxation time constant. *SR* has only half of the dynamic range compared to *IR*. *SR* is much faster than *IR* as the repetition time (*TR*) can be shorter. A single *SR* pulse sequence is shown in Figure 2.6 a where the signal (the FID) is measured after the second RF pulse, t is the time between the two pulses.

The basic part of an *IR* sequence is a $180^\circ_{x'}$ RF pulse, that inverts $\vec{M}$, followed by a $90^\circ_{x'}$ RF pulse, that brings the residual $\vec{M}$ into the x′-y′ plane. A single *IR* pulse sequence is shown in Figure 2.6 b, where t is the inversion time (*TI*) between the two pulses and the signal is acquired after the $90^\circ_{x'}$ pulse and A_t is the signal acquisition time.

These single pulse sequences are repeated a number of times (n), with increasing *SR* or *IR* delay values (t), which is needed to collect a fully recovered curve. The regrowth of $\vec{M}$ is being measured in the x′-y′ plane where it is detected by a RF coil. When this curve has been acquired, T_1 can be calculated. To improve the signal to noise ratio (*SNR*) in these measurements, each pulse

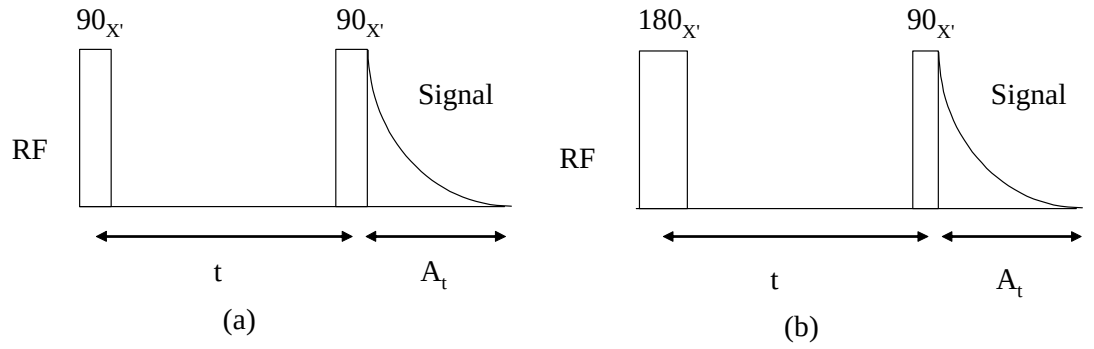

Figure 2.6: (a) a saturation recovery (*SR*) and (b) An inversion recovery (*IR*) pulse sequence.

sequence can be repeated by increasing the number of scans (n_s). The repetition time between successive pulse sequences (*TR*) has to be 5 times T_1 for the *IR* experiment to ensure complete relaxation between each repeated pulse sequence. *SR* sequences consist of multiple $90^{\circ}_{x'}$ RF pulses (applied along the x′-axis) at relatively short repetition times.

The *SR* experiment:

$$\{[90^{\circ}_{x'} - t\ (SR\ delay) - 90^{\circ}_{x'} - A_t - TR]_{n_s}\}_n \tag{2.27}$$

The saturation recovery can be described by the exponential function in Equation 2.25 as shown in Figure 2.7.

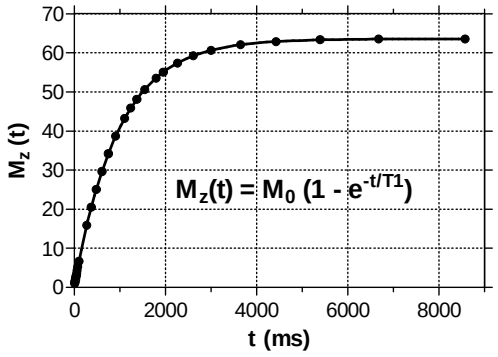

Figure 2.7: Demonstration of longitudinal magnetization recovery. T_1 is measured with a *SR* pulse sequence on doped water ($CuSO_4$ in water).

The *IR* experiment:

$$\{[180^{\circ}_{x'} - t\ (IR\ delay) - 90^{\circ}_{x'} - A_t - TR]_{n_s}\}_n \tag{2.28}$$

The inversion recovery can be described by the exponential function in Equation 2.26, which can also be plotted as a linear function:

$$ln(M_0 - M_z(t)) = ln(2M_0) - \frac{t}{T_1} \tag{2.29}$$

where $M_z(t)$ is the intensity of the signal following the 90° pulse at a time t and M_0 is the limiting value of $M_z(t)$ for a very long interval between the 180° and 90° pulses. T_1 is determined from the slope of the plot of $ln(M_0 - M_z(t))$ versus t (Figure 2.8).

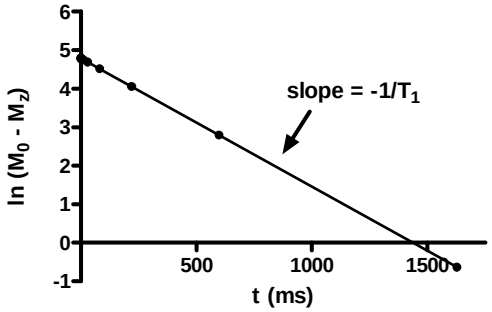

Figure 2.8: The relaxation rate is a slope of $ln(M_0 - M_z(t))$.

It is possible to get a rough estimate of T_1 by using Equation 2.26: $T_1 = t_{null}/ln2$, where t_{null} is when $M_z(t)$ equals zero, but it can lead to large errors. Single parameter fits are based on the assumptions that the T_1 experiment is ideal and that one has an accurate value for M_0. In fact, this might not always be a valid assumption. A more reproducible and accurate approach is to use a nonlinear three-parameter fit with the following equation:

$$M_z(t) = M_0(1 - 2 \cdot \alpha \cdot e^{\frac{-t}{T_1}}) \tag{2.30}$$

In this case the fitting routine is used to obtain the least squares best fit for the three parameters, M_0, T_1 and α. The α-factor adjusts for an imperfect 180° pulse. With nonlinear fitting of data from homogenous nonviscous samples it is no longer necessary to provide a value M_z ($t \rightarrow \infty$), and substantial measuring time can therefore be saved.

In homogenous solutions the monoexponential T_1 is easily determined. In more complex heterogeneous systems with several hidden exponential T_1 components care should be taken when the data are collected and analyzed. It is common to collect as few as 10 data points for a monoexponential decay, wheras 20 to 100 points may be beneficial for biexponential decays.

2.2.2 T_2 relaxation time

As earlier decribed, $\vec{M}$ is a vector sum of individual microscopic magnetizations arising from nuclei in different parts of the sample and hence experiencing slightly different values of the applied field, which is never perfectly homogenous. Therefore, immediatly after the flipping of $\vec{M}$ into the transversal plane the spins starts to dephase or fan out, as some nuclei are precess faster and some slower than the rotating frame. The transverse magnetization components, $M_{x'}$ and $M_{y'}$, will return to their equilibrium value or zero governed by the transverse or *spin-spin* relaxation time constant, T_2.

The spins lose phase coherence not only due to inhomogeneities in the external magnetic field which is a reversible prosess, but also because of the natural processes (spin-spin interactions) responsible for transverse relaxation which is an irreversible process (a *pure* T_2 effect). The combination of these two factors is what actually results in the decay of the transverse magnetization:

$$(T_2^\star)^{-1} = (T_2)^{-1} + (T_2')^{-1} \tag{2.31}$$

where $(T_2^\star)^{-1}$ is the total relaxation, $(T_2)^{-1}$ the irreversible and $(T_2')^{-1}$ the reversible contribution to the total relaxation.

The complex representation of the transverse magnetization, $M_+(t)$, is:

$$M_+(t) = M_{x'}(t) + iM_{y'}(t) \tag{2.32}$$

The direction in the x′-y′ plane of the transverse magnetization vector is given by the phase of the RF pulse, ϕ. In Figure 2.3 b, $\phi = 0$. From the Bloch Equation 2.20 and 2.21, $dM_{x'}/dt$ and $dM_{y'}/dt$, and thus dM_{xy}/dt, can be integrated to obtain the transverse magnetization behavior, where $M_{xy} = |M_+|$ and $M_{xy}(0) = M_0$:

$$M_{xy}(t) = M_0 e^{\frac{-t}{T_2}} \tag{2.33}$$

The time constant T_2 is defined as the time it takes for 63 % of M_{xy} to be lost, i.e. $M_{xy}(T_2) = M_0 e^{-1}$.

The first pulse experiment that measured T_2 was proposed by Hahn, and it was named the spin-echo (SE) experiment [42]. A SE experiment:

$$[90^\circ_{x'} - \tau - 180^\circ_{x'} - \tau]_{n_s} \tag{2.34}$$

where τ equals the echo time, TE, divided by two ($TE/2$). The $180^\circ_{x'}$ pulse rephases the spins which have started to dephase after the $90^\circ_{x'}$ flip into the

x′-y′ plane, which creates an echo after one TE (or 2τ) as shown in Figure 2.9. The FID, which is found after every $90^\circ_{x'}$ pulse, is not used.

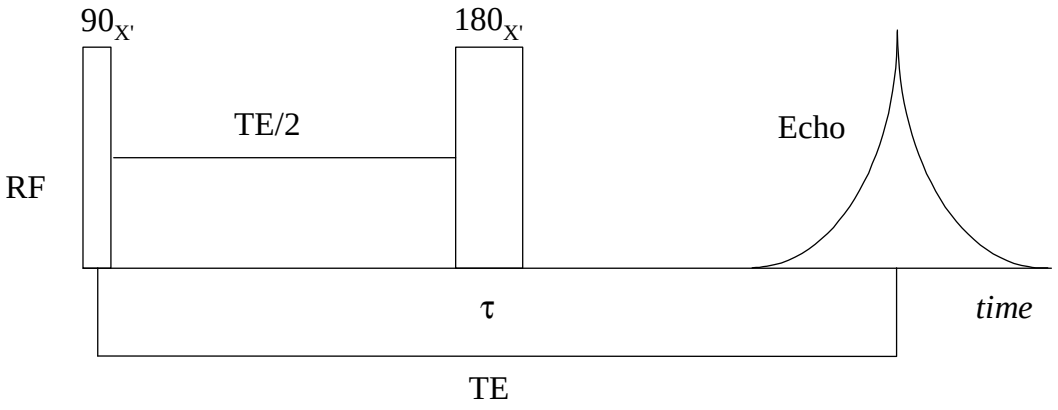

Figure 2.9: Hahn spin echo (*SE*) pulse sequence.

As in the *IR* measurement of T_1 it is necessary to wait an adequate time between pulse sequences (at least five times T_1) for restoration of equilibrium. The *SE* experiment is limited in its range of applicability because of the effect of molecular diffusion. The precise refocusing of all the spins is dependent upon each nucleus remaining in a constant magnetic field during the time of the experiment (2τ). Diffusion can cause the nuclei to move from one part of an inhomogenous field to another and reduce the signal. The time duration in which diffusion can occur is one of the factors that determines the effect of diffusion and it is particulary pronounced at large values of τ and thus strongly affects the measurement of long T_2's. Carr and Purcell [23] were the first to suggest a method to get rid of diffusion effects by introducing a train of $180^\circ_{x'}$ pulses at the end of the Hahn's spin echo, producing a series of alternately positive and negative echos.

Since imperfect 180° pulses will cause loss of signal, and error in the measured T_2, the Meiboom-Gill shift of phases should be used [78], where the first 90° pulse is applied along the y′-axis so that all of the subsequent refocusing is along the x′-axis producing a series of positive echos.

The *CPMG* pulse sequence consists of a $90^\circ_{y'}$ pulse followed by a train of $180^\circ_{x'}$ pulses: $90^\circ_{y'}$ - $(2n - 1)\,\tau$ - $180^\circ_{x'}$, where $n \in \{1,2,\ldots\}$. This produces a series of echos at $2n\tau$, where only each second echo is sampled ($4\tau, 8\tau, \ldots$) since the other echos do not have correct amplitudes. Thus echoes are formed when repetitive $180^\circ_{x'}$ pulses are applied at intervals τ longer than the effective relaxation time $T_2^\star$ but smaller than T_2 (Figure 2.10). Since the τ interval can be made quite short, the effects of spin diffusion can be eliminated. Therefore, the Carr-Purcell-Meiboom-Gill (*CPMG*) pulse sequence is more suited than the *SE* method to measure T_2.

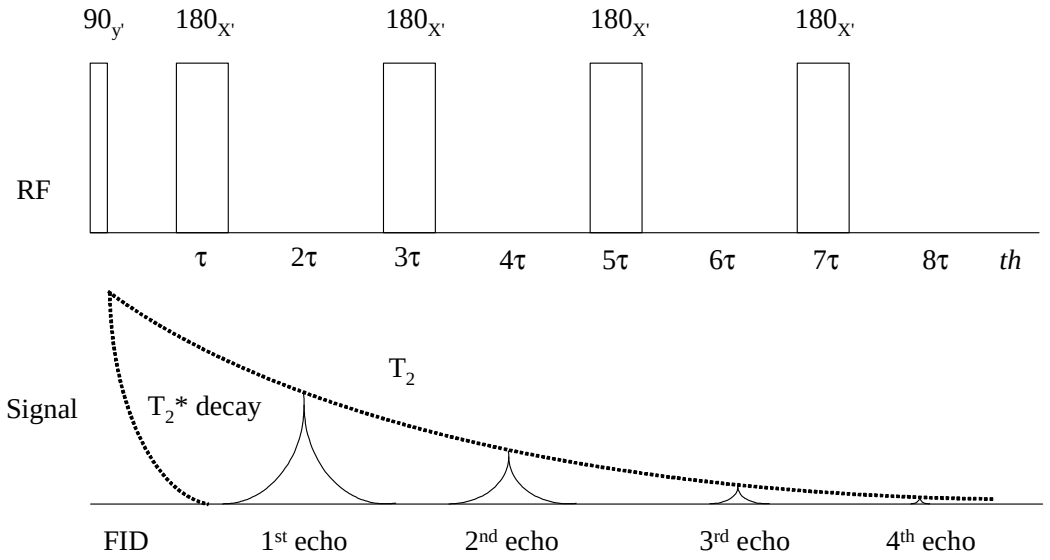

Figure 2.10: Carr-Purcell-Meiboom-Gill (*CPMG*) pulse sequence, where only every second echo is recorded.

A *CPMG* experiment:

$$\{90^{\circ}_{y'} - \tau - [180^{\circ}_{x'} - \tau]_n\}_{n_s} \tag{2.35}$$

In a T_2 experiment it is common to collect 100 data points for a monoexponential decay. For biexponential decays, 200 to 250 points may be beneficial.

2.2.3 *Dipole-dipole* interaction as relaxation mechanism

The primary relaxation mechanism for most spin-1/2 nuclei in molecules in liquids is the magnetic dipole-dipole or spin-spin interaction, i.e. small variations in the local field of a proton due to fluctuation of nearby protons (Section 3.4.2). Concidering two protons, A and B. Then the total field at A arises from the large magnetic field, B_0, and from the field, $\vec{B}_{loc}$, arising from nuclei B. This local field is given by:

$$|\vec{B}_{loc}| = \mu_B(3cos^2\theta - 1)/r^2_{AB} \tag{2.36}$$

where θ is the angle between the internuclear vector, $\vec{r}_{AB}$, and the $\vec{B}_0$ magnetic field. If the protons A and B are in the same molecule (i.e. a water molecule) and if the molecule rotates, the angle θ will change. This causes the local field, $\vec{B}_{loc}$, to fluctuate. For such rotational motions, the molecular correlation time,

τ_c, is the time required for the angle θ to change appreciably. It is the coupling between the nuclear precession and the lattice (or molecular) motions mediated by the dipole-dipole interaction that allows for thermodynamic heat transfer to take place between the nuclear spin system and the rotational motion of the molecules. The relaxation takes place only if the field, $\vec{B}_{loc}$, at nucleus A changes, and only if the changes take place with frequency components at the Larmor frequency. $\vec{B}_{loc}$ can be represented by a microscopic vector $\vec{h}$ that replaces $\vec{B}$ in Equation 2.17, 2.18 and 2.19:

$$\frac{dM_x}{dt} = \gamma(M_y h_z - M_z h_y) \tag{2.37}$$

$$\frac{dM_y}{dt} = \gamma(M_z h_x - M_x h_z) \tag{2.38}$$

$$\frac{dM_z}{dt} = \gamma(M_x h_y - M_y h_x) \tag{2.39}$$

From the these equations it can be seen that the z component of $\vec{h}$ only affects M_x and M_y, and has no effect on M_z at all. Since the z-axes are the same in the laboratory and rotating frame of reference, the $h_z(\omega_0)$ that is stationary in the rotating frame is also stationary in the laboratory frame. However, if h_x and h_y are stationary in the rotating frame, then they move rapidly in the laboratory frame (at the Larmor frequency).

By the time that the dipole moments have returned to their original positions and thus restored M_z to a value of M_0, there can be no components of $\vec{M}$ in the x-y plane. So, since h_x, h_y and h_z all affect M_x and M_y, they affect T_2 (Equation 2.33), but only h_x and h_y affect M_z and hence T_1 (Equation 2.25). Therefore, h_z has no effect on T_1. Since h_z is associated with very slow processes and h_x and h_y are associated with both very slow and very fast processes it is easy to see that:

- T_1 is only affected by very fast dynamic processes (at about the Larmor frequency).
- T_2 is affected by both fast and slow molecular processes.

Therefore, the time T_2 (or $T_2^\star$ if inhomogeneity effects are important) characterizing loss of M_x or M_y, can never be longer than T_1. However, T_2 (and $T_2^\star$) can be shorter than T_1:

$$T_2^\star \leq T_2 \leq T_1 \tag{2.40}$$

2.3 Water exchange

Since conventional (^{1}H) MRI basically is a study of water protons in tissue, understanding the translational (diffusion) and rotational water movements within and between the compartments in the cells is important to interpret what is being observed in the images. In the literature it is still quite common to operate with specific T_1 and T_2 relaxation time constants for each tissue type, that is, monoexponential signals, which in most cases are approximations. Tissue is not homogenous even on the smallest volume element common in MRI. There are different opinions on whether the water exchanges are fast or slow in a MR setting in different cell types. From now on the terms "cellular" exchange will be used for water exchange across the cellular membrane and "vascular" exchange for water exchange across the vascular membrane.

2.3.1 Water exchange theory

In this section the concept of water exchange is depicted. In Figure 2.11 a simplified cardiac tissue with the intra- and extracellular compartments are shown. The compartment sizes in the figures are not representative to the real situation where the intracellular volume is 60-70 % and the extracellular 30-40 % of the total volume in rat cardiac tissue (see Table 8.4). The extracellular compartment is both the space between the cells (interstitium) and the intravascular compartment (see Figure 2.12).

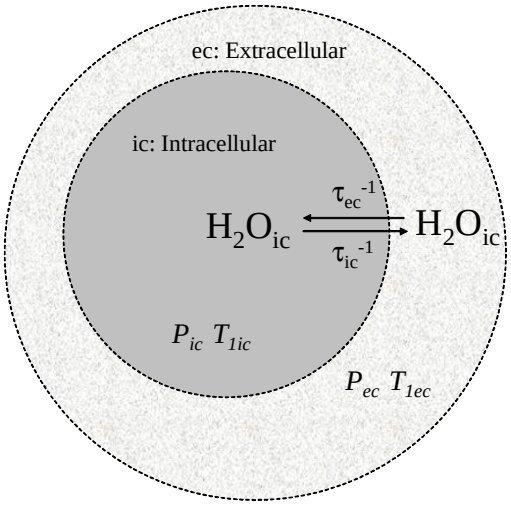

Figure 2.11: Cellular exchange between the intra- and extracellular compartment. The intrinsic compartmentalized T_1 values: p_{ic}, p_{ec}, T_{1ic} and T_{1ec} are shown.

The water exchange rate is defined as:

$$\frac{1}{\tau} = \frac{1}{\tau_{ic}} + \frac{1}{\tau_{ec}} \tag{2.41}$$

where τ_{ic} and τ_{ec} are the proton residence times (lifetimes) in the intracellular (ic) and extracellular (ec) environments in this example, and their inverse are the respective water exchange values. The intrinsic T_1 relaxation rates, that is the relaxation rates in the two environments without exchange are: $\frac{1}{T_{1ic}}$ and $\frac{1}{T_{1ec}}$.

Fast exchange

The water exchange is fast on a MR scale if it is much greater than the difference in the relaxation rates between the two compartments under study [77]:

$$\frac{1}{\tau} >> \left|\frac{1}{T_{1ic}} - \frac{1}{T_{1ec}}\right| \tag{2.42}$$

Then the measured monoexponential T_1 will be a weighted sum of the compartmental relaxation rates, where p_{ic} and p_{ec} are the intra- and extracellular population fractions of the nuclei:

$$\frac{1}{T_1} = \frac{p_{ic}}{T_{1_{ic}}} + \frac{p_{ec}}{T_{1_{ec}}} \tag{2.43}$$

Slow exchange

The water exchange is slow on a MR scale if it is much smaller than the difference in the relaxation rates between the two compartments under study:

$$\frac{1}{\tau} << \left|\frac{1}{T_{1ic}} - \frac{1}{T_{1ec}}\right| \tag{2.44}$$

If the water exchange is slow, the observed apparent biexponential T_1 components are sums of the intrinsic relaxation rates and water exchanges in each compartment, where the apostrophe ($'$) is used on the apparent relaxation data to distinguish between apparent and intrinsic values:

$$\frac{1}{T'_{1ic}} = \frac{1}{T_{1ic}} + \frac{1}{\tau_{ic}} \tag{2.45}$$

$$\frac{1}{T'_{1ec}} = \frac{1}{T_{1ec}} + \frac{1}{\tau_{ec}} \tag{2.46}$$

This biexponential relaxation will be detectable if the two rates differ from eachother to a sufficient degree and are of sufficient magnitude to be distinguished by the measurement method.

2.3.2 The two-site water exchange (2SX) model

Springer's group at the State University of New York, has published a series of Papers [64-66, 114] where they have used a set of modified Block equations that accounts for water exchange pioneered by McConnell (1958) [76]. For longitudinal magnetization (M_z), two sets of equations, corresponding to each compartment (ic and ec) were deduced:

$$\begin{aligned}\left(\frac{dM_z}{dt}\right)_{ic} &= -\omega_1(M_{y'})_{ic} + \left(\frac{M_0 - M_z}{T_1}\right)_{ic} - C_{ic}(M_z)_{ic} + C_{ec}(M_z)_{ec} \\ \left(\frac{dM_z}{dt}\right)_{ec} &= -\omega_1(M_{y'})_{ec} + \left(\frac{M_0 - M_z}{T_1}\right)_{ec} - C_{ec}(M_z)_{ec} + C_{ic}(M_z)_{ic}\end{aligned} \tag{2.47}$$

where $C_k = \frac{1}{\tau_k}$ and k = ic/ec. The Equations in 2.47 differ from the usual Bloch equations (Equation 2.20 - 2.22) by the addition of two terms to the right-hand side, $\pm C_{ic}(M_z)_{ic}$ and $\pm C_{ec}(M_z)_{ec}$. In the first equation $-C_{ic}(M_z)_{ic}$ represents the rate at which $(M_z)_{ic}$ decreases due to the transfer of M_z magnetization out of the ic space, and $C_{ec}(M_z)_{ec}$ measures the rate at which $(M_z)_{ic}$ increases due to the transfer of M_z magnetization into the ic space from the ec space.

The equilibrium exchange of isolated spins between two sites that have different T_1 values, i.e the two-site water exchange (2SX) model, was derived from the equations of Woessner (1961) [113] as outlined below:

The Equations 2.47 are linear homogenous differential equations. If ω_1 is neglected the solutions are exponentials: $e^{\lambda_i t}$, where λ_i are the eigenvalues of the matrix. Woessner [113] presents a function that describes the time dependence of M_z under the influence of longitudinal relaxation and the water exchange. This function is independent of whether there is a difference in the resonance frequencies in the intra- and extracellular compartment, i.e in ω_{ic} and ω_{ec}.

When $T_{1ic} \neq T_{1ec}$, the T_1 relaxation curves are the sums of two exponential functions whose coefficients and time constants are the apparent state populations and relaxation times, respectively. The longitudinal two-component relaxation equation can be given as:

$$M_z = M_0[1 - 2[p'_{ic}e^{(-tR'_{1ic})} + p'_{ec}e^{(-tR'_{1ec})}]] \tag{2.48}$$

where p'_{ic} and R'_{1ic} are the apparent intracellular (ic), p'_{ec} and R'_{1ec} the apparent extracellular (ec) longitudinal relaxation components. $p'_{ic} + p'_{ec} = 1$ and M_0 is the equilibrium magnetization vector.

Intermediate exchange

Fast- and slow water exchange are borderline situations. The in-between situation is also common:

$$\frac{1}{\tau} \sim |\frac{1}{T_{1ic}} - \frac{1}{T_{1ec}}| \tag{2.49}$$

In such instances multiexponential relaxation curves may be observed. For the intermediate exchange situation the observed or apparent relaxation rates would be more different from the intrinsic relaxation rates than is true in the case of slow exchange. This is because in the intermediate exchange case $1/\tau_{ic}$ and $1/\tau_{ec}$ would be closer in value to the intrinsic relaxation rates thereby contributing a more significant portion to the apparent relaxation rate (see Equations 2.45 and 2.46). The intermediate case can be solved by use of the 2SX model advocated by the Springer group.

The exact solutions for the apparent T_1 values based on the equations of Woessner [113], were first presented by Leigh (1971) [70] and McLauglin and Leigh (1973) [77] in the following form:

$$\begin{aligned} \frac{1}{T'_{1ic}}, \frac{1}{T'_{1ec}} =& A_1 \mp \left\{ A_1^2 - \left[\left(\frac{1}{T_{1ic}} + \frac{1}{\tau_{ic}} \right) \cdot \left(\frac{1}{T_{1ec}} + \frac{1}{\tau_{ec}} \right) - \left(\frac{1}{\tau_{ic}\tau_{ec}} \right) \right] \right\}^{\frac{1}{2}} \\ A_1 =& \frac{1}{2(\frac{1}{T_{1ic}} + \frac{1}{\tau_{ic}})} + \frac{1}{2(\frac{1}{T_{1ec}} + \frac{1}{\tau_{ec}})} \end{aligned} \tag{2.50}$$

Similar presentations are found in Hazlewood [44], and in Winkler and Mitchel [112]:

$$\begin{aligned} R'_{1ic}, R'_{1ec} =& \frac{1}{2} \Big\{ R_{1ic} + R_{1ec} + \frac{1}{\tau_{ic}} + \frac{1}{\tau_{ec}} \mp \\ & \sqrt{(R_{1ec} - R_{1ic} + \frac{1}{\tau_{ec}} - \frac{1}{\tau_{ic}})^2 + \frac{4}{\tau_{ic}\tau_{ec}}} \Big\} \end{aligned} \tag{2.51}$$

The physiological parameters τ_{ic} and p_{ic} are related to τ_{ec} and p_{ec} by equilibrium mass balance:

$$p_{ec} = 1 - p_{ic} \tag{2.52}$$

$$\tau_{ic} = \tau_{ec} \cdot \frac{p_{ic}}{p_{ec}} \tag{2.53}$$

where Equation 2.53 is called the McConnell relationship.

The apparent population fractions can be expressed as [112]:

$$p'_{ec} = 1 - p'_{ic} = \frac{R_{1m} - R'_{1ic}}{R'_{1ec} - R'_{1ic}} \tag{2.54}$$

where the average relaxation time R_{1m} has been introduced:

$$R_{1m} = \frac{p_{ic}}{T_{1ic}} + \frac{p_{ec}}{T_{1ec}} = \frac{p'_{ic}}{T'_{1ic}} + \frac{p'_{ec}}{T'_{1ec}} \tag{2.55}$$

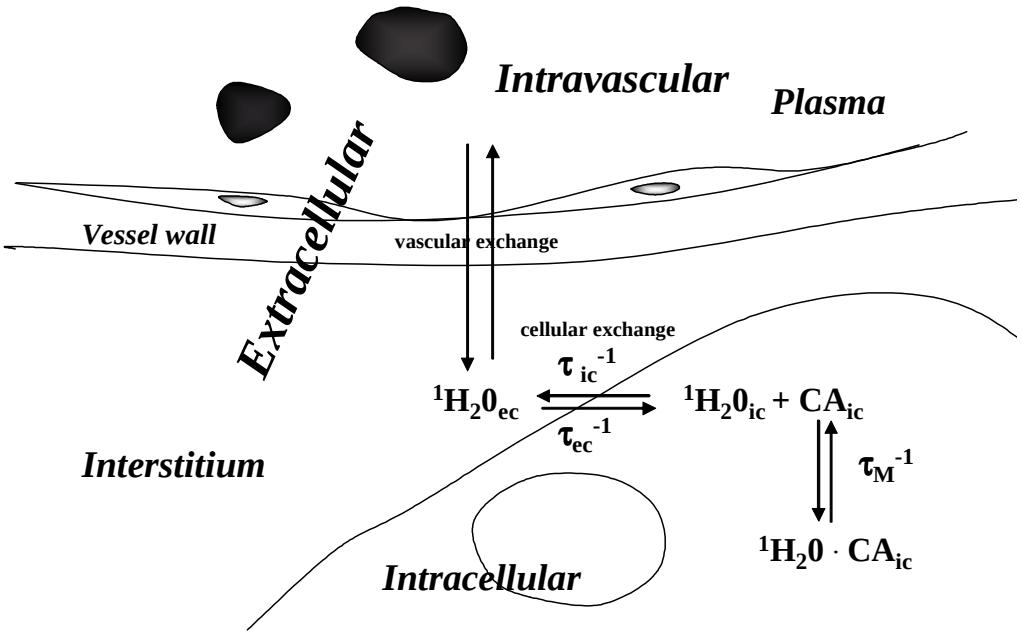

Figure 2.12: The distribution of an ic *CA* in tissue (cross sectional). Mn^{2+}-ions are quickly cleared from the ec space and enter the cells. The ec space is comprised of the interstitium and the intravascular space. The vascular space consists of red blood cells and plasma. In the vessel wall some endothelium cells are shown, and in the ic compartment the nucleus is shown. Inner-sphere τ_M^{-1} and cellular water exchange rates τ_{ic}^{-1} and τ_{ec}^{-1} are illustrated. Adapted from Landis *et al.* [65].

The 2SX water exchange model by Springer *et al.* is only presented by the use of an extracellular contrast agent ($GdDTPA^{2-}$). With manganese compounds, the contrast agent (Mn^{2+}-ions) resides intracellular. In Figure 2.12 all the different compartments in cardiac tissue are named and the water exchanges with an intracellular agent are shown.

It has also been universally assumed that the linear relationship between R_1 and $[CA]$ in homogenous solutions applies to biological tissue. However, the hyperfine mechanism dominates the CA increase of R_1, and requires molecular contact between CA and water. The theory behind these contrast mechanisms will be presented in Section 3.4.

$$R_{1ic} = R_{1ic0} + r_{1ic} \cdot [CA_{ic}] \tag{2.56}$$

where r_{1ic} is the intracellular relaxivity and R_{1ic0} the pre-CA rate constant. This relationship is true for a homogenous solution since the mean water lifetime, τ_M, is exceedingly short for paramagnetic ions ($10^{-9} - 10^{-7}$ s for Gd^{3+}-, Mn^{2+}- and Fe^{2+}-ions) [68].

In Equation 2.51 and 2.54, R_{1ic} was substituted with the right side of Equation 2.56 to obtain the 2SX equations. The other substitutions were done by using Equation 2.52 and 2.53. When the 2SX model is applied on the longitudinal relaxation data the measured Mn content (n mol/g dry wt.) in the ventricular heart specimens and the experimental apparent R'_{1ic}, R'_{1ec}, p'_{ic} and p'_{ec} data are included.

The 2SX equations of Springer *et al.* modified for an intracellular contrast agent (CA_{ic}) with the substitutions given are presented below.

The intracellular apparent relaxation rate constant:

$$\begin{aligned} R'_{1ic} = & \\ & \frac{1}{2}\left[R_{1ec} + r_{1ic}[CA_{ic}] + R_{1ic0} + \tau_{ec}^{-1} + \frac{p_{ec}}{\tau_{ec}(1-p_{ec})}\right] + \\ & \frac{1}{2}\left\{\left[R_{1ec} - r_{1ic}[CA_{ic}] - R_{1ic0} + \tau_{ec}^{-1} - \frac{p_{ec}}{\tau_{ec}(1-p_{ec})}\right]^2 + \right. \\ & \left. \frac{4p_{ec}}{\tau_{ec}^2(1-p_{ec})}\right\}^{\frac{1}{2}} \end{aligned} \tag{2.57}$$

The extracellular apparent relaxation rate constant:

$$R'_{1ec} =$$

$$\frac{1}{2}\left[R_{1ec} + r_{1ic}[CA_{ic}] + R_{1ic0} + \tau_{ec}^{-1} + \frac{p_{ec}}{\tau_{ec}(1-p_{ec})}\right] -$$

$$\frac{1}{2}\left\{\left[R_{1ec} - r_{1ic}[CA_{ic}] - R_{1ic0} + \tau_{ec}^{-1} - \frac{p_{ec}}{\tau_{ec}(1-p_{ec})}\right]^2 + \right. \tag{2.58}$$

$$\left. \frac{4p_{ec}}{\tau_{ec}^2(1-p_{ec})}\right\}^{\frac{1}{2}}$$

The apparent population fractions:

$$\frac{p'_{ic}}{p'_{ic} + p'_{ec}} = \frac{1}{2} - \frac{1}{2}$$

$$\cdot\left(\frac{\left[(R_{1ec} - r_{1ic}[CA_{ic}] - R_{1ic0})(1-2p_{ec}) + \frac{p_{ec}}{\tau_{ec}(1-p_{ec})} + \tau_{ec}^{-1}\right]}{\left\{\left[R_{1ec} - r_{1ic}[CA_{ic}] - R_{1ic0} + \tau_{ec}^{-1} - \frac{p_{ec}}{\tau_{ec}(1-p_{ec})}\right]^2 + \frac{4p_{ec}}{\tau_{ec}^2(1-p_{ec})}\right\}^{\frac{1}{2}}}\right) \tag{2.59}$$

From the 2SX model five intrinsic result parameters can be determined: p_{ec}, τ_{ec}, R_{1ec}, R_{1ic0} and r_{1ic}, and thereafter τ_{ic} and p_{ic} are calculated. R_{1ec} is the ec relaxation rate constant, r_{1ic} the ic relaxivity, R_{1ic0} the ic relaxation rate constant at [Mn]=0 nmol/g dry wt., τ_{ic} and τ_{ec} the ic and ec lifetimes, respectively, and p_{ic} and p_{ec} the ic and ec population fraction, respectively.

2.3.3 2SX and T_2

Zimmerman and Brittin [115] showed that a 2SX analysis is also valid for T_2 experiments. They confirmed that when a two-phase system exists for longitudinal relaxation phenomenon then a corresponding two-phase system exists for transverse relaxation and visa versa, due to the existence of the same two distinct average nuclear correlation times. However, they also claimed that in spite of the existence of such multiple phase systems, there is no guarantee that experimental measurements will resolve multiple T_1's and T_2's due to limited time resolution in the MR measurements, i.e. averaging processes between phases may occur. Woessner [113] also pointed out that if the T_1 values for the sites a and b are much greater than the respective T_2 values, it is

possible to have simultaneously $1/\tau_b \gg 1/T_{1b}$ for T_1 and $1/\tau_b \ll T_{2b}$ for T_2 where monoexponential longitudinal and biexponential transversal relaxation behavior can be observed.

McLaughlin and Leigh [77] formulated a rigorous method for obtaining approximate solutions for any well-defined set of physical assumptions. The exact solutions of 2SX for T_2 were complicated by having to include the influence that the shift of the resonance frequencies between the two environments ($\Delta\omega_{ab}$) has on the transversal relaxation times. The water exchange, $1/\tau_{ab}$, must be faster than $\Delta\omega_{ab}$ in order for the system to relax as a unit.

3. Contrast agents and mechanisms

3.1 Magnetic materials and susceptibility

Magnetic susceptibility is the degree to which a material becomes magnetized when placed in a magnetic field. Types of magnetism:

- Ferromagnetism
- Diamagnetism
- Paramagnetism
- Superparamagnetism

Ferromagnetic materials (Fe, Ni, Co) are the most magnetically active substances, with high magnetic susceptibilities. These materials are made of atoms with permanent dipole moments. When ferromagnets, placed in a external magnetic field, are removed from the field, the electrons in the bonds maintain the alignment and the magnetism remains. This means that ferromagnetic materials can remember their past magnetic history.

In a diamagnetic material (water, Cu, N, $BaSO_4$, and most tissues) the atoms have no permanent dipole moments. When they are placed in a strong magnetic field the atomic dipole moments appear directed oppositely to the direction of the magnetic field. The effect is weak, but its effect, is to cause repulsion where other forms of magnetism give attraction. Because this effect opposes the applied field, the susceptibilities of such materials are negative, and because the effect is weak the magnitudes of the susceptibilites are small.

In a paramagnetic material the atoms have permanent dipole moments, but without magnetic memory properties. If a magnetic field is applied to such a material, the dipole moments try to line up with the magnetic field, but are prevented from becoming perfectly aligned by their random thermal motion. Since the dipoles try to line up with the applied field, the susceptibilities of such materials are positive, but in the absence of the strong ferromagnetic effect, the susceptibilities are rather small. When a paramagnetic material is placed in a strong magnetic field, it becomes a magnet, and as long as the strong magnetic field is present, it will attract and repel other magnets in the usual way. However, when the strong magnetic field is removed, the net magnetic alignment is lost as the dipoles relax back to their normal random motion.

Superparamagnetism is halfway between ferro- and paramagnetism. Superparamagnetism can arise if the crystal containing regions of unpaired spins

is sufficiently large that it can be regarded as a thermodynamically independent, single domain particle. Such a particle has a net magnetic dipole that is large compared to the sum of its individual unpaired electrons. When placed in a magnetic field, the magnetic dipoles orient analogous to paramagnetic materials, but the resulting magnetic moment is much larger than that of a paragmanetic substance. Thus the specific susceptibilities can significantly exceed those of corresponding soluble paramagnetic species because of the magnetic ordering.

3.2 MR contrast agents

MR contrast agents are either paramagnetic (transition metal ions, lanthanides, free radicals, molecular oxygen) or superparamagnetic, where paramagnetic agents have received the most attention as useful contrast agents. The contrast agents are distributed intravascularly (blood pool agents) and extracellularly or can be tissue specific (Table 3.1).

MR contrast media either act predominantly on T_1 relaxation which results in signal enhancement and "positive" contrast, or on T_2 relaxation, which results in signal reduction and "negative" contrast. The positive contrast agents are typically small molecular weight compounds containing paramagnetic ions as their active element, which have unpaired electron spins in their outer shells and long electron spin relaxation time which make them good T_1 relaxation agents. Paramagnetic ions are T_1 agents due to the fact that the T_2's of tissues are very short and are not sizably decreased by reasonable (and safe) concentrations of the agent. Therefore, the transversal relaxation rate ($1/T_2$) enhancement is less emphasized in this thesis.

The other group of agents are small particulate aggregates often termed superparamagnetic contrast medium. These agents produce predominantly spin-spin relaxation effects, but very small particles smaller than 300 nm also produce substantial T_1 relaxation. The clinically introduced substances are either renally or hepatically excreted media, which stay in the intravascular or extracellular tissue compartment.

Paramagnetism arises from unpaired electron spins in either 3d (transition metal) or 4f (lanthanide) orbitals, a property shared by a number of metal ions. The number of unpaired electrons can range from 0 to 7, resulting in spin states from 0 to 7/2. Some transition metal ions are: Mn^{2+}, Mn^{3+}, Fe^{2+}, Fe^{3+} and Co^{2+}, and some lanthanide ions are: Eu^{2+}, Ho^{3+}, Dy^{3+} and Gd^{3+}. These paramagnetic ions are effective either as relaxation enhancers, resonant frequency shift or magnetic susceptibility agents. Metal ions such as Gd^{3+}, Mn^{2+} and high-spin Fe^{3+} that have a large number of unpaired electron spins, coupled with relatively long electron spin relaxation times (T_{1e} = 10^{-8} - 10^{-10} s), function primarily as relaxation agents. On the other hand, metal

Table 3.1: MR contrast agents.

Chemical name	Generic name	Brand name
extracellular agents:		
$Gd(DTPA)(H_2O)]^{2-}$	gadopentetate dimeglumine	Magnevist†
$Gd(DOTA)(H_2O)]^{-}$	gadoterate meglumine	Dotarem§
$Gd(DTPA\text{-}BMA)(H_2O)]$	gadodiamide	Omniscan*
$Gd(HP\text{-}DO3A)(H_2O)]$	gadoteridol	ProHance$^{\sharp}$
$Gd(DO3A\text{-}butrol)(H_2O)]$	gadobutrol	Gadovist†
$Gd(DTPA\text{-}BMEA)(H_2O)]$	gadoversetamide	OptiMARK^{‡,a}
blood pool agents:		
MS-325	gadophostriamine trisodium	AngioMARK^{‡,a}
NC100150 Injection	PEG-feron (USPIO)	Clariscan^{*,a}
MION	monocrystalline iron oxide nanoparticle	MION^{a}
hepatobiliary agents:		
$Gd(BOPTA)(H_2O)]^{2-}$	gadobenate dimeglumine	MultiHance$^{\sharp,b}$
$Gd(EOB\text{-}DTPA)(H_2O)]^{2-}$	gadoxetic acid disodium	Eovist†
MnDPDP	Mn dipyridoxyl diphosphate	Teslascan^{*,b}

*Nycomed-Amersham, †Schering, ‡Epix/Mallinckrodt, §Guerbet, $^{\sharp}$Bracco.
a = not approved, but in clinical trials, b = in addition extracellular.
USPIO: ultrasmall superparamagnetic iron oxide.

ions such as Dy^{3+}, Ho^{3+} and Eu^{2+} that have many electron spins but much faster relaxation characteristics, have negligible nuclear relaxation properties but are highly effective in altering the resonant MR frequency. Effectiveness as MR magnetic susceptibility contrast media is a function of net molecular magnetic moment. The most effective metal ions for this purpose are Dy^{3+}, Ho^{3+} and Gd^{3+}. [87]

The contrast agents are pharmaceutical substances with different routes or behaviors in the body. Since they act indirectly by influencing the magnetic moment of protons, how they distribute and interact with water is of key importance when exploring the efficacy and specificity of the contrast agent.

3.3 Manganese compounds as contrast agents

3.3.1 Physicochemical and relaxation properties

Manganese (Mn) is a trace metal needed to maintain vital functions in the body [56] and deficiency states have been reported. A main function is that divalent (Mn^{2+}) and trivalent (Mn^{3+}) ions act as a redox pair in enzymes. The radius of divalent Mn^{2+} (0.80 Ångstrøm (Å)) is close to that of ions like zinc (Zn^{2+}, 0.74 Å), ferrous iron (Fe^{2+} 0.76 Å) and intermediate between magnesium (Mg^{2+}, 0.65 Å) and calcium (Ca^{2+}, 0.99 Å) [26, 47]. Mn^{2+} and Mn^{3+} have respectively 5 and 4 unpaired electrons and possess paramagnetic properties with Mn^{2+} being the most efficient [87].

3.3.2 Mn-dipyridoxyl-diphosphate (MnDPDP)

At present there is only one commercially available Mn^{2+}-containing contrast medium (Teslascan, Amersham Health, Amersham, UK). Teslascan containing MnDPDP is clinically approved for MRI of liver. MnDPDP contains two vitamin B6 (pyriodoxal phosphate) moieties that through nitrogen and oxygen bounds (Figure 3.1) keeps Mn^{2+} in a chelate that is highly soluble and stable in pure water. It was developed for liver MRI based on the assumption of vitamin B6 mediated liver uptake of the entire molecule [86, 87].

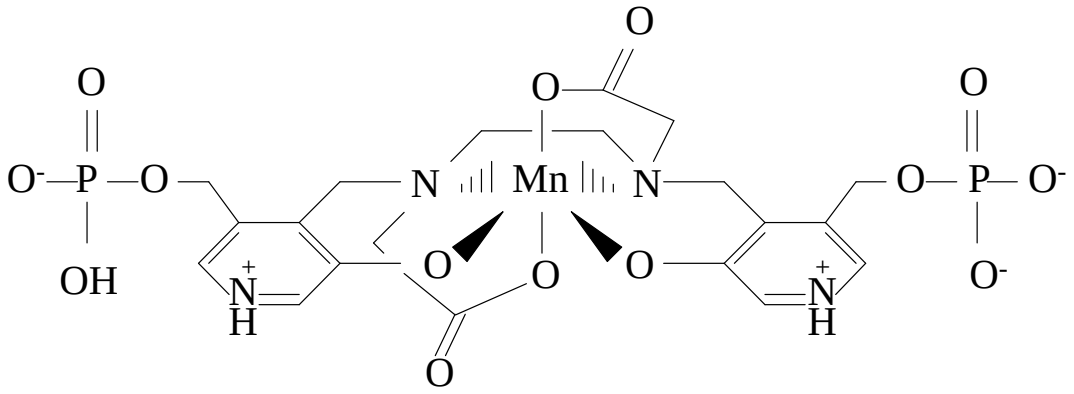

Figure 3.1: Structure of MnDPDP.

However, the stability constant ($\log K$) for MnDPDP (15.10) is lower than for ZnDPDP (18.95) and after intravenous administration MnDPDP undergoes rapid transmetallation with Zn^{2+} in plasma [86]. It also appears that other divalent cations like Ca^{2+} and Mg^{2+} may contribute to Mn^{2+} release from the chelate [93]. In plasma the chelator $DPDP^{2-}$ is simultaneously dephos-

phorylated to yield monophosphate ($DPMP^{-}$) and phosphate-free dipyridoxylethyldiamine ($PLED^{2-}$). Thus the overall *in vivo* metabolism follows two lines from MnDPDP: to ZnDPDP, ZnDPMP and ZnPLED; and, to MnDPMP and MnPLED.

After injection or infusion in humans [105], MnDPDP disappears quickly from plasma, and the initial plasma half-live ($t_{1/2\,\mathrm{intial}}$) of total Mn^{2+}-compounds following infusion of a low dose (5 μmol/kg body wt.) is less than 20 minutes. It also appears that MnPLED is the main metabolite being present in plasma over the first 30 minutes after intravenous administration.

3.4 Relaxation time constants and contrast mechanisms

3.4.1 Contribution to relaxivity

In MR images the contrast is the result of a interplay of several complex factors, including the relative T_1 and T_2 relaxation times of the water protons and the proton density of the imaged tissues, as well as instrumental parameters. The mechanisms behind T_i (i = 1,2) and contrast enhancement have to be carefully studied in order to understand how MR contrast agents function in solutions and tissues.

Relaxivity (r) is a parameter that describes the effectiveness of the contrast agent to reduce T_i as a function of its concentration. The addition of a paramagnetic solute causes an increase in the longitudinal and transverse relaxation rates, $1/T_1$ and $1/T_2$, respectively. The observed relaxation rate, $(T_i^{-1})_{obs}$, of such solutions is a sum of the diamagnetic and paramagnetic relaxation rates:

$$(T_i^{-1})_{obs} = T_i^{-1} + T_{ip}^{-1} \tag{3.1}$$

where T_i^{-1} is the (diamagnetic) solvent relaxation rate constant in the absence of a paramagnetic species and T_{ip}^{-1} represents the additional paramagnetic contribution. In the absence of solute-solute interactions, the solvent relaxation rate constants are linearly dependent on the concentration of the paramagnetic species ($[M]$):

$$(T_i^{-1})_{obs} = T_i^{-1} + r_i \cdot [M] \tag{3.2}$$

where r_i is the relaxivity defined as the slope of this dependence in units of $(\mathrm{s\ mM})^{-1}$. This relationship is true for a homogenous solution since the water

exchange on the metal ion, τ_M^{-1}, is exceedingly fast and effective for paramagnetic ions.

The electron spin interacts through dipole-dipole coupling with the nuclear spin residing in the paramagnetic complex (the inner-sphere case) as well as the outside of it (the outer-sphere case). Inner-sphere relaxation refers to relaxation enhancement of a solvent molecule directly coordinated to the paramagnetic ion (Figure 3.2 a), and outer-sphere relaxation refers to relaxation enhancement of solvent molecules in the second coordination sphere (Figure 3.2 b) and beyond (i.e. bulk solvent) (Figure 3.2 c).

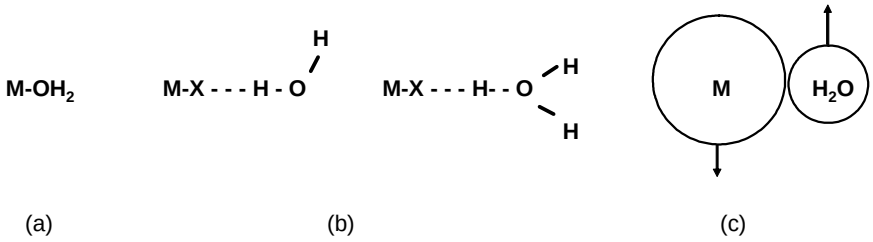

Figure 3.2: (a) Inner-sphere relaxation, (b-c) outer-sphere relaxation, where (b) is analytically treated as the inner-sphere relaxation [68].

Therefore, the measured ^{1}H relaxation rates T_{ip}^{-1} in the presence of paramagnetic complexes is considered as the sum of two terms:

$$T_{ip}^{-1} = (T_i^{-1})_{\text{inner-sphere}} + (T_i^{-1})_{\text{outer-sphere}} \tag{3.3}$$

where the first and second term of the equation correspond to the inner- and outer-sphere contribution to the relaxation rate, respectively. The first mechanism is well understood. The second mechanism is only less exploited, but it involves translation diffusion of the water molecule past the chelate (the metal ion in a complex). For further reading about the outer-sphere mechanism, see the review of Lauffer [68].

The inner-sphere (*IS*) longitudinal and transversal relaxation rates can also be expressed as in Equation 3.4, 3.5 and 3.6.

$$\frac{1}{T_1^{IS}} = \frac{P_M q}{T_{1M} + \tau_M} \tag{3.4}$$

$$\frac{1}{T_2^{IS}} = q P_M \frac{1}{\tau_M} \left[\frac{T_{2M}^{-1}(\tau_M^{-1} + T_{2M}^{-1}) + \Delta\omega_M^2}{(\tau_M^{-1} + T_{2M}^{-1})^2 + \Delta\omega_M^2} \right] \tag{3.5}$$

$$\Delta\omega_{obs}^{IS} = qP_M \left[\frac{\Delta\omega_M}{(1+\tau_M T_{2M}^{-1})^2 + \tau_M^2 \Delta\omega_M^2} \right] \tag{3.6}$$

where P_M is the mole fraction of metal (M) ion, q is the number of water molecules bound per metal ion and T_{iM} is the relaxation time of the bound water protons. $\Delta\omega$ refers to the chemical shift difference between the paramagnetic complex and a diamagnetic reference. From Equation 3.4 it can be seen that if the water exchange is fast enough so that $\tau_M \ll T_{1M}$, then the relaxation rate enhancement experienced by the bulk solvent will depend on the relaxation rate enhancement for the coordinated solvent molecule ($1/T_{1M}$).

T_{iM} was customarily considered in terms of the Solomon [98] and Bloembergen [12] equations, but they have been found inadequate in describing the magnetic field dependence of the longitudinal and transverse relaxivities in simple aqua solutions such as that of Mn^{2+} ($S > 1/2$). Bloembergen and Morgan [13] developed a theory for the field dependency of T_{ie} that accounted for these discrepancies.

3.4.2 The Solomon-Bloembergen-Morgan equations

The value of T_{iM} is now customarily considered in terms of the Solomon-Bloembergen-Morgan (SBM) equations, which represents the sum of dipolar ("through space") and scalar, or contact ("through-bounds"), contributions.

$$\begin{aligned} \frac{1}{T_{1M}} = & \underbrace{\frac{2}{15}\left[\frac{S(S+1)\gamma_I^2 g^2 \beta^2}{r^6}\left(\frac{3\tau_{c1}}{1+\omega_I^2\tau_{c1}^2} + \frac{7\tau_{c2}}{1+\omega_s^2\tau_{c2}^2}\right)\right]}_{\text{dipole-dipole term}} \\ & + \underbrace{\frac{2}{3}\left[\frac{S(S+1)A^2}{\hbar^2}\left(\frac{\tau_{e2}}{1+\omega_s^2\tau_{e2}^2}\right)\right]}_{\text{scalar term}} \end{aligned} \tag{3.7}$$

$$\begin{aligned} \frac{1}{T_{2M}} = & \underbrace{\frac{1}{15}\left[\frac{S(S+1)\gamma_I^2 g^2 \beta^2}{r^6}\left(4\tau_{c1} + \frac{3\tau_{c1}}{1+\omega_I^2\tau_{c1}^2} + \frac{13\tau_{c2}}{1+\omega_s^2\tau_{c2}^2}\right)\right]}_{\text{dipole-dipole term}} \\ & + \underbrace{\frac{1}{3}\left[\frac{S(S+1)A^2}{\hbar^2}\left(\tau_{e1} + \frac{\tau_{e2}}{1+\omega_s^2\tau_{e2}^2}\right)\right]}_{\text{scalar term}} \end{aligned} \tag{3.8}$$

where the variable S being the electron spin quantum number ($\frac{5}{2}$ for Mn-ions and $\frac{7}{2}$ for Gd-ions), γ_I is the nuclear gyromagnetic ratio, ω_I and ω_s are the Larmor frequencies for nuclear and electron spins, r is the proton-metal ion distance, and τ_{ci} and τ_{ei} are the correlation times for dipolar and scalar interactions, respectively. The remaining constants are g (2.0023), the electronic Landé factor for the free electron, β, the Bohr magneton, and $A/\hbar$ is the electron-nuclear hyperfine coupling constant.

The first part of Equations 3.7 and 3.8 contains a dipole-dipole term, dependent on $1/r^6$, and is modulated by the correlation time τ_{ci}:

$$\frac{1}{\tau_{ci}} = \frac{1}{T_{ie}} + \frac{1}{\tau_M} + \frac{1}{\tau_R} \tag{3.9}$$

where τ_R is the rotational tumbling time for the entire metal-water unit. The scalar relaxation mechanisms is modulated by the correlation time τ_{ei}:

$$\frac{1}{\tau_{ei}} = \frac{1}{T_{ie}} + \frac{1}{\tau_M} \tag{3.10}$$

In some cases the scalar mechanism is the dominant relaxation effect, as is the case with Mn^{2+}-aquaions. The equations of the field dependency of T_{ie} are not presented here, but can be found in the review of Caravan *et al.* [22], where also the different parameters in the Equation 3.7 and 3.8 are discussed in more details.

The dipole-dipole term

The figure below demonstrate the dipole-dipole relaxation rates as predicted by the SBM theory. In addition to showing whether R_1 and R_2 vary with the correlation times, their temperature and field dependencies are displayed. In nonviscous media as water ($\tau_c = 10^{-12} - 10^{-10}$ s), where $\omega_0\tau_c << 1$, R_1 equals R_2 and the proton-metal ion distanse (r) does not affect T_1. The $1/T_1$ is at its maximum for $\tau_c^{-1} = \omega_0$ ($\sim 10^{-9}$ s) at any particular operating field strength (0.15 to 2 T). From this viscous area moving towards solids (higher τ_c values), the longitudinal relaxation experience "dispersion", that is, T_1 increases with higher field strengths while T_2 continues to decrease. The temperature logically opposes the changes in correlation times, i.e. as the temperature decreases the correlation time increases. For nonviscous liquids moving towards low temperatures (τ_c increases) leads to more efficient relaxation. For viscous liquids a decrease in temperature may either increase or decrease T_1. For solids, a decrease in temperature will result in an increase in T_1. [74]

The set of relaxivity data measured over a large range of magnetic field strength values represents what is termed a nuclear magnetic relaxation dispersion

(NMRD) profile, whose experimental points are fitted through all the Equations above. König and coworkers have done NMRD studies with different contrast agents [60].

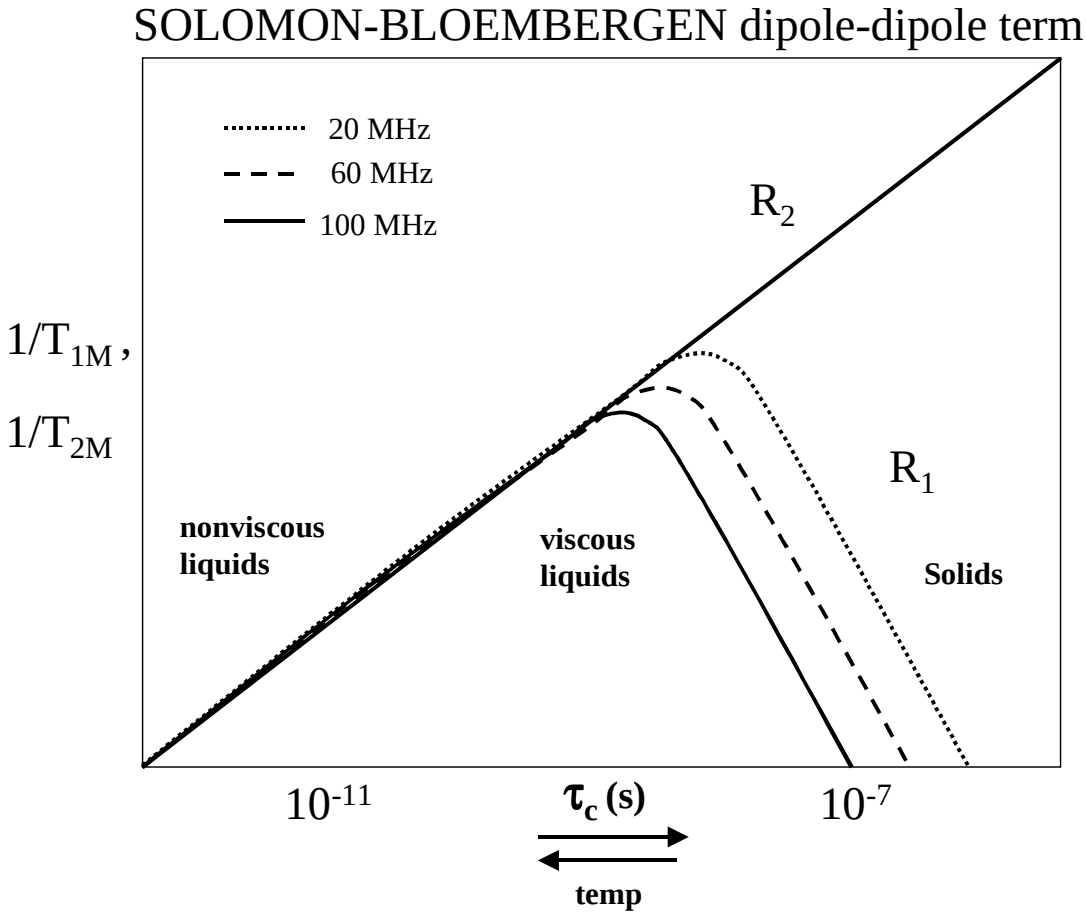

Figure 3.3: Correlation times, temperature and field dependency.

3.4.3 Relaxation enhancement

Relaxivity is a function of the number of electrons, but is also highly dependent on long electron spin relaxation times (T_{1e}). Paramagnetic agents possess a large magnetic moment from their unpaired electrons and generate a local magnetic field that is ~600-fold greater than protons. Without the influence of a paramagnetic agent, the principal relaxation mechanism of solvent nuclei is caused by dipolar interactions between nuclei, modulated by molecular tumbling or rotational motion. Introduction of a paramagnetic agent results in a magnetic field interaction between the electron magnetic dipole and the proton nuclear dipole, and T_1 is shortened by an electron-dipolar interaction mechanism. In addition, the tumbling paramagnetic ions with their large

magnetic moments act to augment variation in the local magnetic fields experienced by the protons thereby causing them to dephase faster. $T_2^\star$ is thus enhanced (shortened).

3.4.4 Manganse as T_1-agents

In a Paper by Aime *et al.* [1] the SBM equations have been applied to studies of some manganese complexes, which were both bound and unbound to high molecular weighted human serum albumin (HSA) complexes. The inner-sphere chelates with one coordinated water had higher relaxivity ($\sim$ 4 (s mM)$^{-1}$) than the outer-sphere chelate with q = 0 (r_1 = 1.6 (s mM)$^{-1}$) at 0.47 T, 25°C. When the chelates were bound to HSA the relaxivity increased as expected most drastically for the complexes with q = 1 due to the increased τ_R ($\sim$ 100 ps to 2-3 ns), i.e. r_1 = 48-55 (s mM)$^{-1}$. This proves that the binding itself increased the relaxivity drastically solely due to the increased rotational tumbling time. Their conclusion was, that since Mn^{2+}-complexes have the advantage of showing much faster exchange rates (τ_M^{-1}) for the coordinated water, these blood pool agents have relaxivities close to analogous Gd^{3+}-complexes in spite of the lower effective moment of manganese. The water exchange for Mn^{2+}-complexes is not the same as for Mn^{2+}-aquaions. The field dependency of T_{ie} concerning the same Mn^{2+}-complexes has been discussed further in the paper by Kruk and Kowalewski [63].

For all paramagnetic ions other than Mn^{2+}-aquaions, the total contribution to the relaxivity arises from the dipolar interaction which gives a characteristic NMRD profile. For Mn^{2+}-aquaions scalar relaxation gives a low-field (<1MHz) dispersion. However, no scalar contribution to $1/T_1$ is observed when Mn^{2+}-ions are complexed with protein, because the correlation times become about the same for the two interactions ($\tau_{c1} = \tau_{e1}$) due to the increased τ_R [59].

The longitudinal relaxivity of *in vitro* $MnCl_2$ is $\sim$ 7-8 (s mM)$^{-1}$ at 20 MHz and 37-40°C [35, 75, 82]. The relaxation effect is solely due to inner-sphere relaxation, where the Mn^{2+}-ions have six coordinated water molecules and fast water exchange ($\tau_M = 10^{-8}$ s) [58]. MnDPDP, which is a stable complex *in vitro*, is about 4 times less efficient compared to $MnCl_2$ [35, 75, 81, 87, 104]. MnDPDP is a low molecular weight complex, with a short rotational tumbling time (τ_R) and no inner-sphere relaxation, q = 0. That is, *in vitro*, $MnCl_2$ is a *pure* inner-sphere agent and MnDPDP a *pure* outer-sphere agent.

In liver and other tissues as the heart a marked increase in r_1 and r_2 was observed for both $MnCl_2$ and MnDPDP [35], which is quite different from the behavior of stable gadolinium chelates. $MnCl_2$ dissociates immediately in tissue, but the free Mn^{2+}-ions bind to macromolecules in plasma and some in the interstitium (see Section 4.3.2). Thereafter, the remaining ions are taken up into cells. Since MnDPDP also dissociates in tissue, free Mn^{2+}-ions enter

Table 3.2: *In vitro* relaxitivities at 20 MHz and 37°C and inner-sphere relaxation parameters.

Substance	r_1 $(\text{s mM})^{-1}$	q	τ_M s
$MnCl_2$	6.9	6	10^{-8}
MnDPDP	1.8	0	-

the cells simular to Mn^{2+}-ions dissociated from $MnCl_2$.

The NMRD-profiles of Mn^{2+}-ions in water show decreasing relaxation rates with increasing field strength, which also means that T_1 will increase with increasing field strength. König and co-workers, who have studied NMRD profiles of Mn^{2+}-ions in plasma and different tissues, have seen a change of pattern compared to *in vitro*. A maximum relaxivity (2-3 times more than *in vitro*) is found at 0.47 T for Mn^{2+}-ions as seen with Mn^{2+}-complexes with long τ_R. This is well investigated and proves, that Mn^{2+}-ions in plasma and tissues bind to (unknown) macromolecules, or structures, presumably cell membranes, and thereby increase their correlation time with water protons [60].

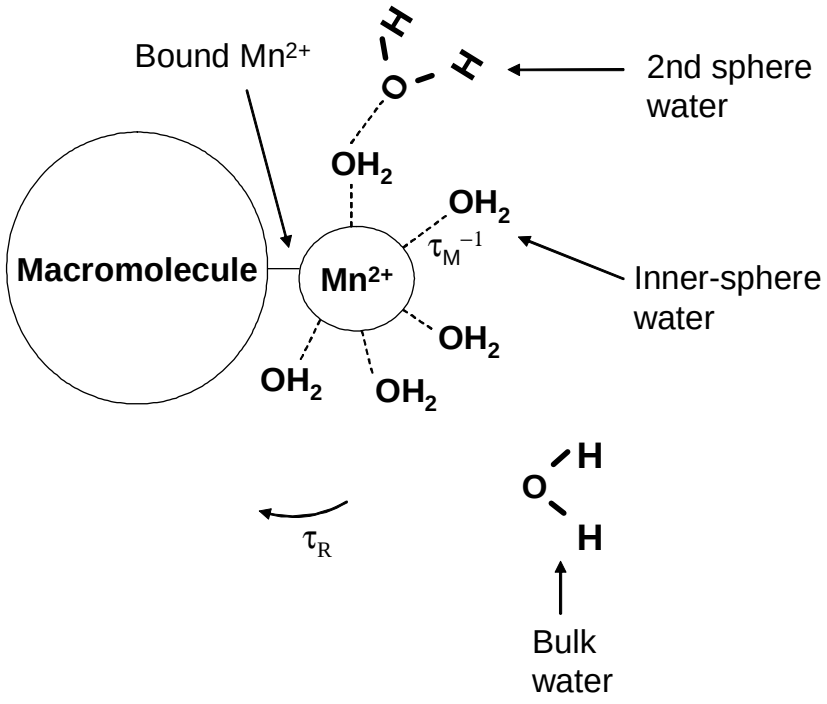

Figure 3.4: Mn^{2+}-ions bind to macromolecules and cell membranes in tissue.

The partial immobilization of the contrast agent increases the rotational correlation time between proton and electron spins, which becomes the dominant source of relaxation enhancement. In isolated hepatocytes from rats as little as 1-2 % of the total intracellular Mn^{2+} is free [101]. In Figure 3.4 the binding

of Mn^{2+}-ions to macromolecules is illustrated. The the paramagnetic agent rotates together with the macromolecule as a unit, and the large τ_R will lead to more effective proton relaxation enhancement.

4. Manganese and cardiac MRI

4.1 Early history and development

4.1.1 Cardiovascular safety

$MnCl_2$ was the first contrast medium tested for use in cardiac MRI [69] but was soon abandoned due to the fear of uncontrolled slow Ca^{2+} channel blockade in cardiomyocytes [79] and thus the rapid induction of an acute heart failure. Attempts to circumvent an apparent cardiotoxicity included addition of Ca^{2+} to Mn^{2+}-releasing media [91, 92] or use of preferably stable Mn^{2+}-complexes. One such complex [86, 87] MnDPDP was to become safely employed [95] for liver MRI. As earlier mentioned, it was also demonstrated that MnDPDP was unstable [39] but released Mn^{2+} in a slow manner that prevented contractile failure [17].

Parallel studies in *ex vivo* bovine arteries [3] showed that both $MnCl_2$ and MnDPDP induced a dose-dependent enhancement of nitric oxide (NO) mediated vasodilation, most probably due to their inherent SOD mimetic and NO conserving properties. Furthermore, experiments in conscious dogs did not reveal any sign of cardiotoxicity and it was shown that potential tendencies to depression of cardiovascular function was counteracted by a rise in sympathetic tone [53].

Altogether, the above results correspond well with NO-like facial flushing and transient cutaneous heat feeling, but not hypotension, being commonly observed during rapid infusion or injection of a high dose of MnDPDP [95]. In spite of the accumulated evidence to the contrary, cardiotoxicity is still a returning issue in contrast media pharmacology [103].

4.1.2 MR efficacy

Early studies [60, 101] showed potent proton R_1 enhancement in various rabbit tissue specimens and differences in field dependence (assessed by relaxometry) in addition to differences in pharmacokinetics between a freely dissociable Mn^{2+} salt and a slowly dissociable Mn^{2+} chelate. Intriguingly, two components were partly observed for R_1 in these relaxometry experiments.

Two studies from the same time period [91, 92] showed increased T_1 based signal intensity in normally perfused versus hypoperfused canine myocardium and perfusion deficits becoming more evident after infusion of the potent vasodilator dipyridamole. Then a series of *in vivo* studies with regional ischemia and reperfusion were carried out in a rat coronary occlusion and deocclusion

model by the Higgins' group in San Francisco, and it was shown that MnDPDP could be used for assessment of viability of nonreperfused or reperfused myocardium [14, 89, 111].

4.2 Research in Trondheim

Brurok and Jynge studied Mn^{2+}-releasing agents in isolated rat and guinea pig hearts with emphasis on mechanisms in the cardiac handling of Mn^{2+} as an intracellular contrast agent (MnMRI). Basic concepts were proposed in 1994 and were in 1997 incorporated into a patent application for cardiac MnMRI.

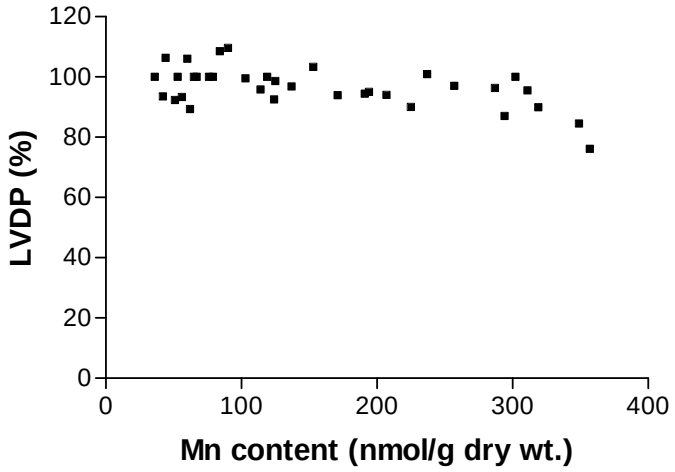

Figure 4.1: Left ventricular developed pressure (LVDP) in individual hearts during perfusion (washin) with $MnCl_2$ (0-30 μM) versus myocardial Mn content after washout. Adopted from Brurok [18].

Some main results, inferences and conclusions form these studies were:

- Depression of contractile function, as assessed by LVDP, did not occur (Figure 4.1) below [Mn^{2+}] 30 μM [18]. Still hearts were able to increase their Mn content by four-five times.
- High concentrations of Mn^{2+} are unlikely *in vivo* due to strong Mn^{2+} plasma protein binding [87, 93, 106]. Controlled infusion of Mn^{2+}-releasing compounds may thus be safely undertaken with minimal if any impairment of cell Ca^{2+} influx and cardiac function in humans.
- MnMRI may be used to monitor Ca^{2+} channel activity. The cellular content of Mn metal was proportional to the depression of contractile func-

tion during the preceding infusion of a Mn^{2+}-releasing compound [16, 18, 19].

- There is a rapid uptake of Mn^{2+} during a washin phase. After an initial minor washout phase the myocardial Mn metal content remains elevated, and cell retention makes delayed imaging possible.
- Entry and retention of Mn^{2+} cease early after the onset of ischemia [16], but resume in viable cells on reperfusion. MnMRI can be therefore be used to assess viability and to indicate perfusion of the myocardium.
- Close concordance existed between myocardial Mn content and monoexponential T_1 values [16].
- MnDPDP functions as a slow releaser of Mn^{2+} when compared to $MnCl_2$, with the latter about 10 times more effective [16, 17, 19].
- Both MnDPDP and MnPLED, a metabolite of MnDPDP, possess SOD mimetic properties *in vitro* [20].

Altogether it was shown that there are close relationships between Ca^{2+} channel activity, Mn^{2+} entry and retention, metabolic activity, and MR relaxation properties.

4.3 Recent MnMRI studies

Mechanisms of cardiac uptake of Mn^{2+}-ions were also studied by others. Thus van der Elst *et al.* [108] in *ex vivo* rat heart experiments demonstrated line broadening of the ^{31}P MR resonances of adenine nucleotides following Mn^{2+} uptake. Their main findings were that $MnCl_2$ was more effective as a relaxation agent than MnDPDP and that Mn^{2+} uptake was greatly reduced by the slow Ca^{2+} channel inhibitors verapamil and nifedipine.

Recent *in vivo* experiments have shown a considerable potential for MnMRI in the assessment of myocardial function and viability. Thus Hu and Koretsky [48] in anesthetized mice showed a close concordance between positive (dobutamine) and negative (diltiazem) inotropic interventions during $MnCl_2$ infusion and recorded changes in MR signal intensity in the cardiac left ventricular wall. Flacke *et al.* [37] examined myocardial late contrast enhancement [57] in rats and showed that three Mn^{2+}-releasing compounds, in contrast to an extracellular Gd^{3+} chelate, demonstrated a time resistent close correlation between infarct size determined by MnMRI and by tetrazolium staining. By slight variations in T_1 based MRI techniques and infusion of $MnCl_2$, Krombach *et al.* [62] were able to demonstrate (hypo- or hyperintense) regions of rat myocardium stunned by short coronary artery occlusions.

In parallel with these heart studies the Koretsky group in 1997 [71] laid the ground for a series of later animal studies of brain neural tract imaging with use of $MnCl_2$ as a Ca^{2+} seeking probe and introduced the term Mn-enhanced-MRI (MEMRI).

4.3.1 Ca^{2+} supplemented Mn^{2+}-containing media

In order to prevent depression of cardiac contractile function during intravenous infusion of a Mn^{2+}-containing and rapidly Mn^{2+}-releasing medium, it has been proposed to supplement these media with Ca^{2+}. In early studies, Schaefer *et al.* [91, 92] employed experimentally Mn^{2+}-gluconate enriched with Ca^{2+}-gluconate in a 1:1 ratio. In development for clinical use are new contrast media [103, 116] based on rapidly dissolving Mn^{2+} and Ca^{2+} salts, preferably with Mn^{2+} and Ca^{2+} gluconates in a ratio of 1:8 or 1:10 (Eagle Vision Pharmaceuticals Corporation, Exton, PA, USA). One such medium EVP 1001-1 has been developed for perfusion and viability assessments in the myocardium [103].

4.3.2 Distribution of Mn^{2+}-ions after release from non-stable contrast media

The below diagram presents major pathways for Mn^{2+} released from contrast media to the heart and to subcellular sites in cardiomyocytes. It is indicated that Mn^{2+}-ions are released either in a rapid, intermediate or slow manner after intravenous administration of the medium.

Mn^{2+} binds extensively to plasma proteins with albumin as the main ligand and α-macroglobulin and possibly also transferrin as contributing ligands [56, 87, 93]. Accordingly, the free ionic activity of Mn^{2+} in plasma is low, preferably at or below 1-5 μM. The major initial distribution occurs to liver and only a minor fraction is available for uptake in the heart. In cardiomyocytes Mn^{2+} influx occurs mainly via slow Ca channels and partly and probably via the Na^{+}-Ca^{2+} exchanger (NCX) in the sarcolemma [9, 27, 33, 49, 56, 71]. Subsidiary pathways for a much slower uptake may be via transferrin mediated endocytosis [40] or via divalent metal transporter (DMT1) proteins [2]. However, little is known about these pathways in cardiomyocytes.

Inside cardiomyocytes Mn^{2+} binds to protein and membrane phospholipid sites and to small molecules including ATP [56, 108]. From the cytosol Mn^{2+} may distribute to different organelles of which mitochondria, partly due to a high volume fraction of about 35 % [55], appears as most essential for MR contrast purposes. Mitochondrial entry and exit seem to occur in competition with pathways for Ca^{2+} [38, 49].

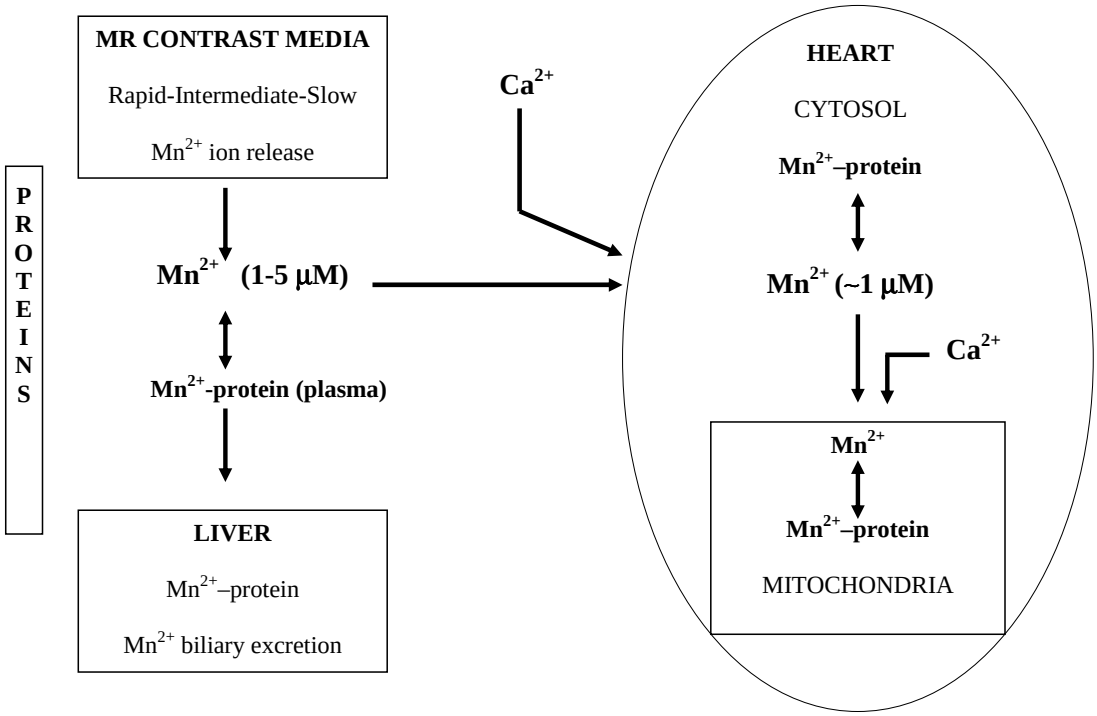

Figure 4.2: Distribution of Mn^{2+} after intravenous administration.

Although there is a lack of measurements of intracellular free Mn^{2+}, it seems likely that there is, as indicated in the diagram, a considerable gradient with lower Mn^{2+} activity from the extracellular compartment to the cytosol and from the cytosol to the mitochondria which act as a main cellular store [38, 49, 56]. The large content and tight packing of potential Mn^{2+}-binding macromolecules in mitochondria may provide a reasonable explanation for the ability of Mn^{2+}-ions to be retained intracellularly for hours. In contrast to what could be expected, it appers that an acute elevation in rat myocardial Mn content to 25 times the normal level was well tolerated without persistent depression of cardiac function or reduction in ATP [18].

5. Background and aims

5.1 Background

The present studies and thesis originated from the research on manganese ions (Mn^{2+}) as intracellular contrast agents for cardiac MRI carried by professor Per Jynge and Heidi Brurok at the Department of Physiology and Biomedical Engineering. At the completion of the above work a physiological basis for potential future use of Mn^{2+}-releasing compounds in cardiac MRI was more or less established. However, among the remaining questions to be clarified from the basic mechanistic side, two appeared as essential. The first issue concerns the efficacy of intracellular Mn^{2+}-ions as T_1 (and T_2) shortening agents and the second the need for a detailed characterization of the interplay between Ca^{2+} and Mn^{2+} when competing for cell uptake and thus for MR efficacy.

The MR group headed by professor Jostein Krane at the Department of Chemistry, Faculty of Natural Sciences and Technology had applied a two-component T_2 analysis of data from MR relaxography [94, 99]. Their materials were sediments from oil drilling, and biexponential T_2 analysis was used to describe in more detail relationships between oil and water in rock. After joining forces with this group the question arose whether two-component T_1 analysis could reveal important information about water distribution and the efficacy of intracellular Mn^{2+}-ions in heart tissue. This led to the start of the first study in the present thesis and during its completion the other two studies were gradually advanced.

5.2 Aims

1. The first aim was to assess whether studies of tissue T_1 relaxation could be improved by applying a biexponential function instead of, as commonly applied, a monoexponential function for analysis of measured T_1 values. (I-III)

2. Since it was then found that tissue T_1 relaxation parameters could be dissolved in two components with possible intracellular and extracellular origins, the second aim was to assess the influence of water exchange upon the apparent T_1 data sets. (I-III)

3. The third aim was with use of tissue relaxography and secondary analyzes to be able to obtain information about the intracellular efficacy and work mode of Mn^{2+}-ions. (I-III)

4. The fourth aim was to examine in more detail the influence of interactions between Mn^{2+} and Ca^{2+} in uptake and retention of manganese. (I, III)

6. Materials and Methods

The main experimental design of the present thesis was the *ex vivo* perfused heart from rats (Paper I and II) or guinea pigs (Paper III) followed by relaxography of exiced cardiac tissue at the end of the experiments.

6.1 Preparations of the isolated heart

Guidelines by the local ethical committee for animal research were followed. Male Wistar rats (230-300 g body wt.) were anesthetized by diethyl ether (Paper I and II) and male guinea pigs (340-435 g body wt.) were anesthetized by intraperitoneal injection of sodium thiopentone (100 mg/kg body wt.) (Paper III), and heparinized. The hearts were rapidly excised, placed in cold (4°C) perfusion medium, and within one minute mounted onto the aortic cannula of the modified Langendorff perfusion system.

The standard Langendorff perfusion system as seen in Figure 6.1 consists of water-jacketed and temperature controlled reservoirs and perfusion lines, where perfusion is based on the use of non-recirculating perfusate [67]. The cardiac temperature was monitored with a digital thermistor in the right ventricle and maintained at 37°C. The hearts were perfused in a retrograde mode, which means that buffer passes through the coronary arteries that supply the myocardium with oxygen and substrates, leading to spontaneously beating hearts. The perfusate is drained into the right atrium and exits from a hole in the right pulmonary artery. The perfusate was glucose-containing Krebs Hensleits bicarbonate buffer (KHBB) equilibrated with 95 % O_2 and 5 % CO_2 to obtain a pH of 7.35-7.40 [61]. KHBB contained (in mM): $NaCl_2$ 118.5; $NaHCO_3$ 25.0; KCl 4.7; KH_2PO_4 1.2; $MgSO_4$ 1.2; $CaCl_2$ 1.25 and glucose 11.1. During exposure to Mn-containing substances, a modified buffer was used where chloride replace phosphate- and sulfate-ions in order to prevent precipitation of Mn-salts.

This system provides experimental control and has many advantages as it is cheap, easy to handle, good for demonstrations and a large number of experiments can be performed in a short time period. The model is widely used in acute laboratory heart experiments including physiological, pathophysiological, pharmacological and toxicological studies. Nevertheless, there are some experimental limitations to keep in mind for these experiments; the nervous system is cut off and the circulation is not normal, blood is not present and the flow has to be kept artificially high (10 ml/min for rats and 15 ml/min for guinea pigs) to provide enough oxygen to the tissue because of the lack of oxygen transporting erythrocytes. There are also no plasma proteins present leading to a low viscosity buffer. In addition, the buffer contains no Zn^{2+}-

and Fe^{2+}-ions. The flow rate can either be pressure or volume regulated. In the experiments described here the flow rate was volume regulated by use of flow-adjustable pumps. Contrast agents were infused through a sideline of the aortic cannula with a flow rate of 0.5 ml/min (see Figure 6.1).

A water-filled latex balloon (0.15 ml) placed in the left ventricle (LV) was connected to a pressure transducer for the recording of LV pressures (LVP), LV developed (systolic-diastolic) pressure (LVDP) and heart rate (HR). Analogue signals were amplified, digitally converted and processed in a computer.

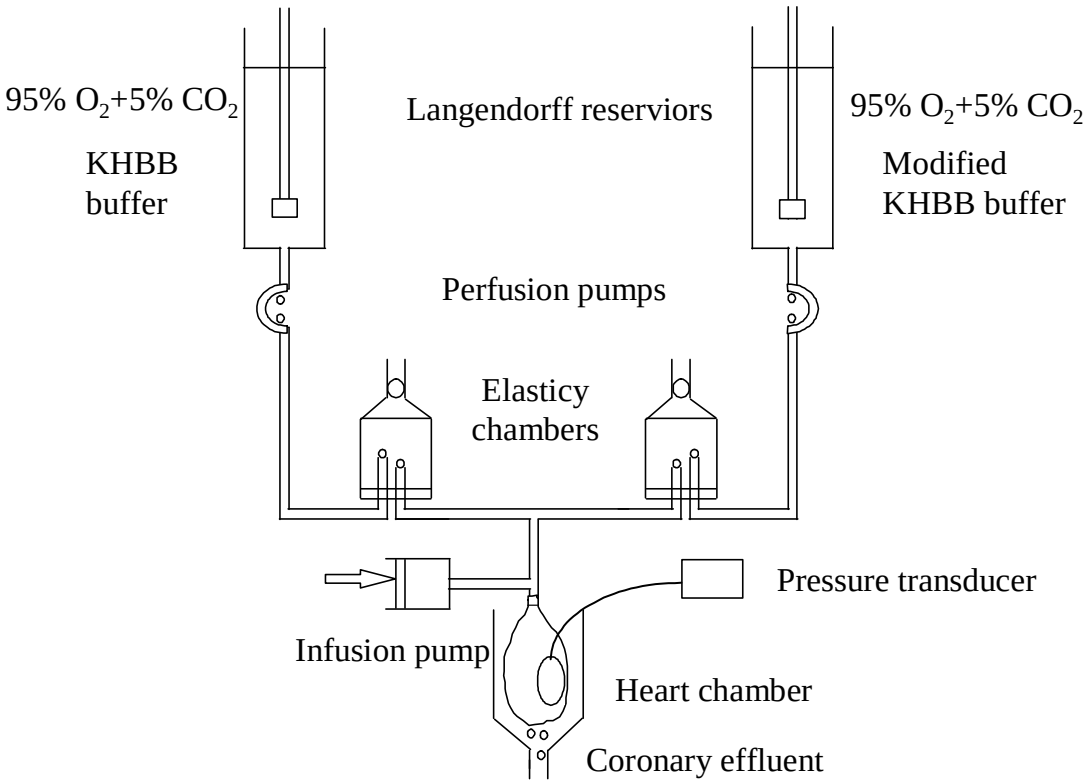

Figure 6.1: The Langendorff perfusion apparatus.

6.2 Mn-administration

Rat hearts in Paper I and II were subjected to the same protocol:

- initial control perfusion period for 10 or 15 minutes
- 5 minutes perfusion with the contrast media present ('Mn-washin' of $MnCl_2$ or MnDPDP)
- 15 minutes period of recovery ('Mn-washout')

In paper III the protocol was different. Three different experimental groups were used, to each a specific test substance was given:

- control, receiving KHBB during washin period
- Mn^{2+}-ions in KHBB plus ascorbic acid during washin
- Mn^{2+}-ions plus Ca^{2+}-gluconate in a 1 Mn^{2+}:10 Ca^{2+} ratio plus ascorbic acid during washin

Each of the above group was subjected to ascending concentrations of its test substance (10, 50, 100 and 500 μM) with a 5 minutes washin phase followed by a 10 minutes washout phase.

The experiments in Paper I-III were designed so that the hearts were loaded with Mn^{2+}-ions during the washin phases. Thereafter, the extracellular Mn^{2+}-ions were removed during the washout phases. Relaxography and biochemical analyses on all the *ex vivo* hearts were done.

6.3 Relaxography and biochemical analyses

At the end of experiments the left plus right ventricular tissue was blotted dry for extraneous water. Immediately thereafter proton relaxation analysis followed.

A low field (0.47 T) Bruker Minispec spectrometer (Bruker AG, Reinstetten, Germany) with a 10 mm bore opening calibrated at 37°C was used for relaxography measurements (see Figure 6.2). The pulse sequence inversion recovery (*IR*) was used to measure T_1 and the Carr-Purcell-Meiboom-Gill (*CPMG*) was used to measure T_2. Care was taken to keep temperature constant (37°C) during experiments. Pulse angle calibrations (90°, 180°) were performed on suitable reference samples.

Finally the ventricular specimens were frozen (liquid nitrogen) and freeze-dried for Mn metal content analyses with flame atomic absorption spectroscopy (FAAS) [73] (Paper I and II) or inductive coupled plasma (ICP). High performance liquid chromatography (HPLC) was used to measure the concentrations of phosphocreatine (PCr) and adenosine-triphosphate (ATP) (Paper III).

(a)

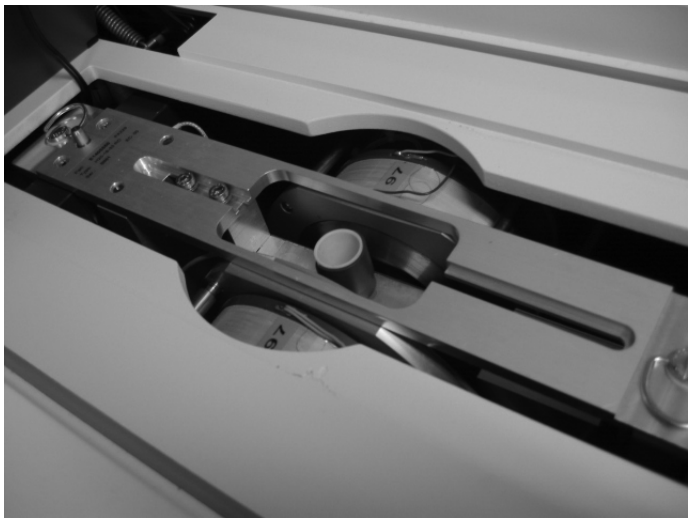

(b)

Figure 6.2: (a) The outside and (b) the inside of a Bruker Minispec pulsed NMR spectrometer where the probe holder and magnet can be seen.

6.3.1 Judicious choice of appropriate inversion times (TI) in mono- and biexponential T_1 decays

The Bruker T_1 application

A. The T_1 data in Paper I-III were measured by use of a standard IR pulse sequence application on the Minspec instrument developed by Bruker (Bruker AG, Reinstetten, Germany), where among other things the first (TI_0) and last inversion time (TI_N) and the number of data points (N) had

to be given. The program calculates a delay factor (DF):

$$DF = (TI_N/TI_0) \cdot e^{1/N} \tag{6.1}$$

and the data points are chosen like this:

$$TI_i = TI_{i-1} \cdot DF \tag{6.2}$$

where $i = 1 : N$.[1]

In Figure 6.3 a homogenous solution with ideal pulse angles, T_1 = 300 ms, M_0 = 60 and α = 1 is simulated. The data were fitted with the *IR* function (Equation 2.30). A $DF = (TI_N/TI_0) \cdot e^{1/(N-1)}$ was used to collect the data, where the data were spanning from 10 to 3000 ms and N = 10. Figure 6.3 b shows the Gaussian distribution of the chosen TI values in this example, which is the partial derivation of $M_z(t)$ with respect to T_1, where the minimum is the T_1 value of 300 ms:

$$\frac{dM_z(t)}{dT_1} = \frac{2 \cdot M_0}{T_1^2} \cdot t \cdot e^{-t/T_1} \tag{6.3}$$

The results from the three parameter nonlinear curve fitting are (see Figure 6.3 a): χ^2/D_{0F} = $1.4 \cdot 10^{-6} \simeq 0$, R^2 = 1, M_0 = $99.99 \pm 8 \cdot 10^{-4}$, T_1 = $299.99 \pm 4 \cdot 10^{-3}$ ms, α = 1. These results prove that the model and the fit are good.

B. A control heart with two independent compartments, i.e. a slow exchange situation, was simulated. The biexponential T_1 values were 650 ms for the short component T_{1-1} and 2600 ms for the long component T_{1-2} with population fractions of 60 % and 40 %, respectively. The Bruker *IR* application was used to measure T_1, where the TI data were spanning from 5 to 16000 ms collecting 30 data points. The regression analysis (Figure 6.4 a) estimated parameters that were the same as the simulated values, where R^2=1 and χ^2/D_{0F}= $1.74 \cdot 10^{-7}$ prove that both the model and fit are excellent for the biexponential data. In Figure 6.4 b the Gaussian curves for each of the T_1 values are displayed, demonstrating that the chosen data points covers both the components.

C. Two-component data with the same intra- and extracellular T_1 value: T_{1-1} = T_{1-2} = 500 ms, but different population fractions, are simulated. The p_{01} and p_{02} values are the same as for the heart cells: 60 % and 40 %. The Bruker *IR* application with TI values spanning from 10 to 3000 ms was used.

The regression analysis (Figure 6.5) shows that the model and fit are excellent for these data. The data were fitted with a monoexponential

[1] In this application the last data point chosen by the operator is not included in the data set. If DF had been $(TI_N/TI_0) \cdot e^{1/(N-1)}$ instead this had been avoided.

regression function assuming a one compartment system. The data contain information about two compartments and biexponential T_1's, which is not revealed in the fitting procedure. Applying a biexponential regression analysis confuses the program and large uncertainties in the estimated parameters are displayed. This proves that if the T_1 values of the intra- and extracellular compartment are the same, the data will be treated as a one compartment system with an average T_1, even though the compartment sizes are different.

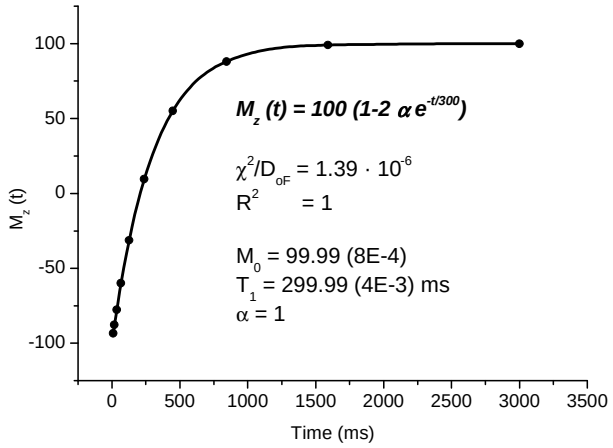

(a)

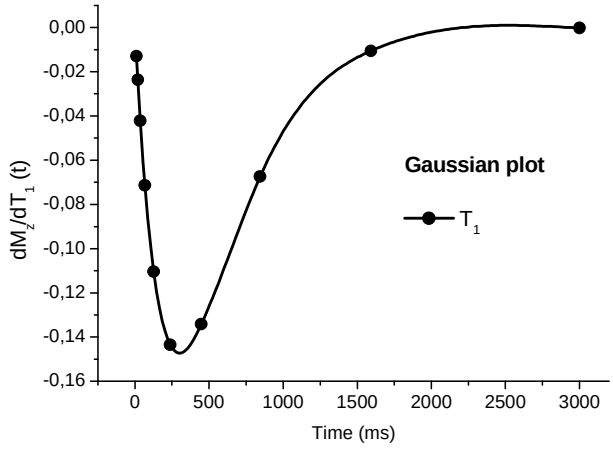

(b)

Figure 6.3: Simulated data from a homogenous solution analyzed with nonlinear regression plotted in (a), and it's Gaussian curve is plotted in (b).

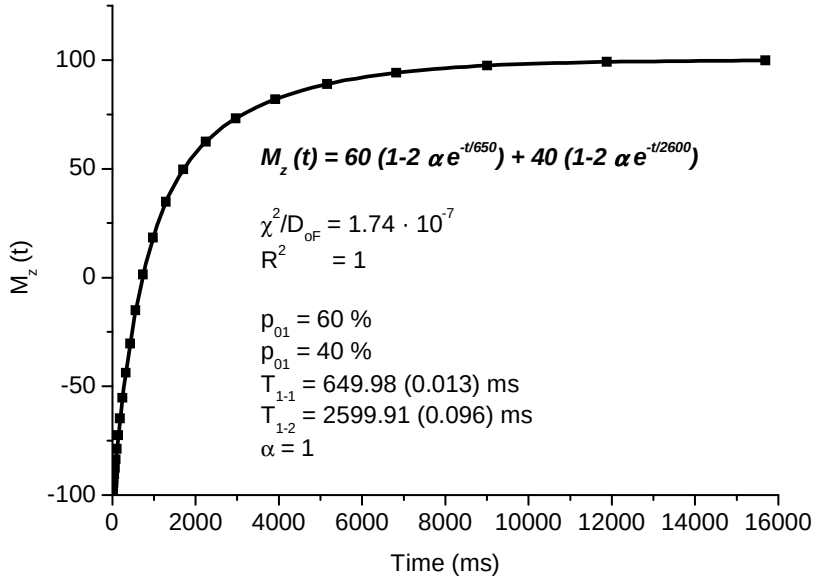

(a)

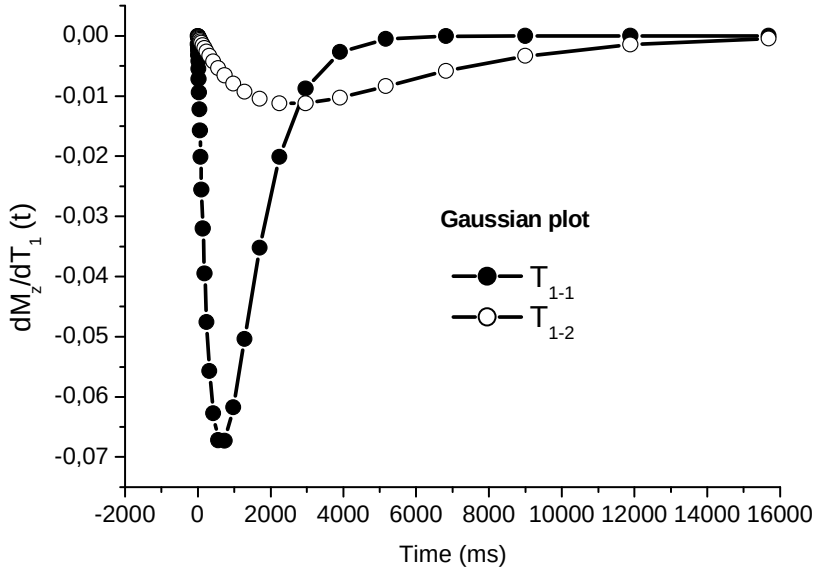

(b)

Figure 6.4: Simulated control heart data fitted with nonlinear regression plotted in (a) and its Gaussian curve in (b).

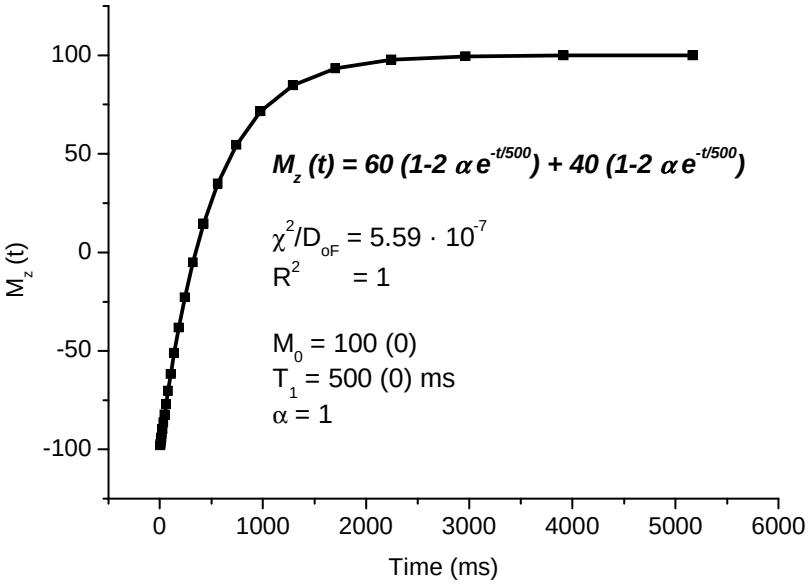

(a)

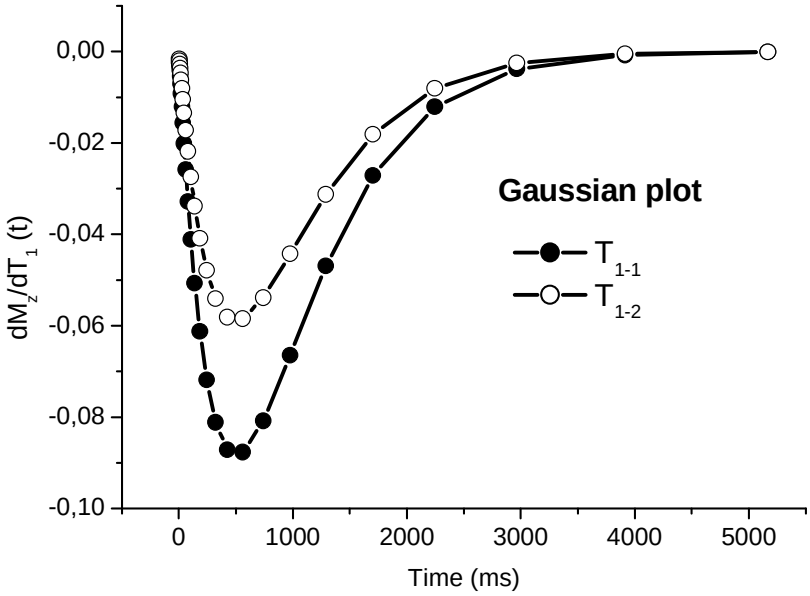

(b)

Figure 6.5: Simulated two-component data with T_{1-1} = T_{1-2} = 500 ms and p_{01} = 60 % and p_{02} = 40 % fitted with nonlinear regression plotted in (a) and its Gaussian curve in (b).

Modifications of the Bruker pulse sequences

Since selection of the proper inversion times in the *IR* experiment is crucial for the identification of multicomponent T_1's in a inhomogeneous sample, the data points should preferable be in this interval: $0.3 \cdot T_1 - 2.7 \cdot T_1$. This is the area on the Gaussian curve -70 % and $+70$ % away from the minimum value, where the minimum value for each Gaussian curve is the T_1 component value [5]. If there are three T_1 values, three Gaussian curves can be displayed: $dM_z(t)/dT_{1-1}$, $dM_z(t)/dT_{1-2}$ and $dM_z(t)/dT_{1-3}$. This knowledge can be used to collect inversion times that covers all the expected T_1 component values in advance of the measurements.

For this purpose a semiautomatic T_1 application routine was developed, i.e. a modified *SR* pulse sequence. The operator can make a guess of which T_1 values the sample contains, and appropriate TI's will be collected:

$$TI(N) = -T_1 \cdot ln(0.78 - 0.71 \cdot i/N) \tag{6.4}$$

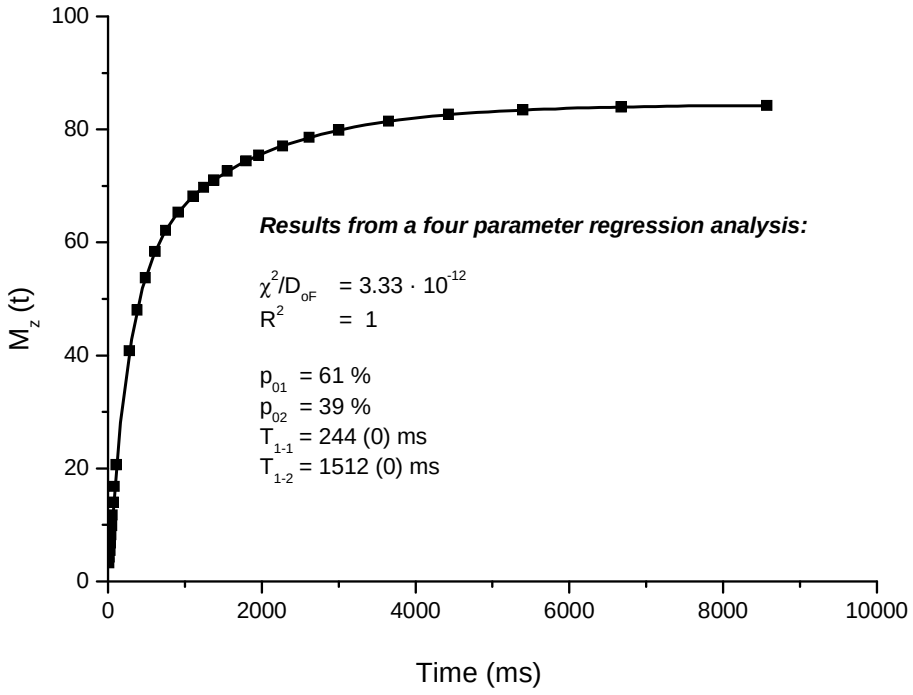

Figure 6.6: A two compartments system with two separated solutions of $CuSO_4$ in a MR probe, one of the solutions with a T_1 of 244 ms and the other one of 1512 ms.

A phantom with two isolated compartments, each containing a homogenous solution of $CuS0_4$ was analyzed with this routine. The phantom was made by placing a concealed small glass container with a 0.49 mM $CuSO_4$ solution into

the MR probe containing a 4.91 mM $CuSO_4$ solution. The T_1 values that were expected to be measured based on the concentration of the paramagnetic salt were 244 and 1512 ms. The pulse lengths were 4.24 μs for the 90° pulse and 8.36 μs for the 180° pulse.

With nonbiased knowledge of the T_1 values, three initial T_1 values could for example be expected: T_{1-1} = 50 ms, T_{1-2} = 1000 ms and T_{1-3} = 4000 ms. Then the TI values would be chosen from these three intervals: 14-133, 279-2659 and 1117-10637 ms. The other parameters used were: N = 30, TR = 10 s, n_s = 1 and the gain was 60-70 % of the maximum FID. The resulting TI values were spanning from 14 to 8571 ms, which covers all the three suggested T_1 values.

The regression analysis (Figure 6.6) estimated parameters that were the same as the theoretical values. R^2=1 and χ^2/D_{0F}=3.33·10^{-12} prove that both the model and fit are excellent for the two compartment data when these TI values are used. The prefered dynamic range for both T_{1-1} (68-649 ms) and T_{1-2} (422-4021 ms) are covered in the collected data points.

6.3.2 *In vitro* experiments

In vitro relaxography experiments were carried out on the test substances that were used on the *ex vivo* rat and guinea pig hearts. This baseline information about proton relaxation under the influence of $MnCl_2$ (I), MnDPDP (II), *Manganese* and *Manganese-Calcium* (III) was obtained with the dry substances dissolved in pure N_2-equilibrated water at 37°C and with relaxography (T_1 and T_2). Monoexponential regression analysis of T_1 and T_2 confirmed that the salts were dissolved in a homogenous solution, i.e. a single compartment. The standard plots also indicate whether the instrument has an acceptable accuracy when comparing the relaxivities with literature values.

The T_1 relaxation behavior in solutions with increasing concentrations of $MnCl_2$ (steeper and steeper curve) is shown in Figure 6.7 and in Paper I the linear plot of the inverted T_1 (R_1) versus $MnCl_2$ of the same data is shown. This has been carried out for all test substances used in Paper I-III.

As shown in Figure 3.3 $R_1 = R_2$ for nonviscous liquids such as water. Since $R_1 = R_2 \simeq 0.3$ s^{-1} at 20 MHz and 37°C in pure water these equations can be used to calculate T_1 and T_2 in an *in vitro* solution with specific r_1 and r_2 values:

$$T_1(ms) = \frac{1000}{(r_1[Mn(mM)] + 0.3)}$$
$$T_2(ms) = \frac{1000}{(r_2[Mn(mM)] + 0.3)} \tag{6.5}$$

Even though these equations should determine the relaxation times exactly,

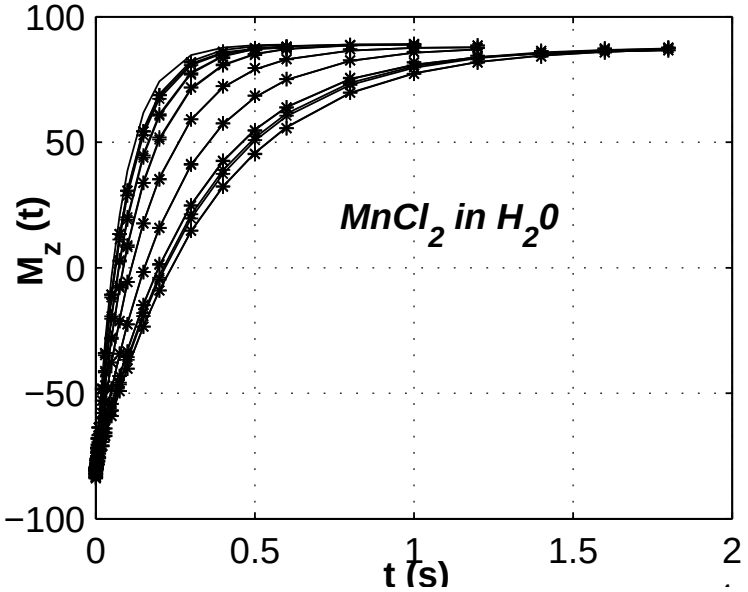

Figure 6.7: *In vitro* $MnCl_2$ relaxography. The curves are getting steeper and steeper with increasing concentrations of $MnCl_2$.

some experimental errors must be accounted for if the values achieved are diverging from the ones obtained with these equations.

6.3.3 Excised myocardium

Fresh ventricular specimens were placed in 10 mm NMR tubes. As earlier explained the samples were temperature calibrated before the relaxographic measurements were performed. Measurements of T_2 followed by T_1 were started 10-30 minutes after end of experiment, and completed within a maximum of 60 minutes using the Minispec spectrometer at 37°C. T_1 was measured by the *IR* experiment of Bruker collecting at the most 22 logarithmically chosen data points, 4 scans and 2 duplicates. TR was always fives times T_1. The TI data were chosen by the use of pilot measurements to ensure that the collected data were spanning from around $-M_0$ to as close to $+M_0$ as possible. In Paper I and II TI values from 0.1 to 14000 ms at most were collected, and in Paper III TI values from 5 to 8400 ms were collected. T_2 was measured using the *CPMG* experiment collecting 200-350 data points, 4 scans and 2 duplicates.

Nonlinear regression analysis

First the data were fitted to a monoexponential regression curve resulting in one T_1, but the model was not suitable for the data. By transforming a tech-

nique developed for multicomponent analysis in the oil and rock industry, the data were fitted to a biexponential regression curve containing five parameters:

$$M_z(t) = p_{01}(1 - 2 \cdot \alpha \cdot e^{\frac{-t}{T_{1-1}}}) + p_{02}(1 - 2 \cdot \alpha \cdot e^{\frac{-t}{T_{1-2}}}) \tag{6.6}$$

where the five parameters were: p_{01}, α, p_{02}, T_{1-1} and T_{1-2}. This model, which suited the data, resulting in one short and one long relaxation component (T_{1-1} and T_{1-2}; or T_{2-1} and T_{2-2}) containing approximately 60-70% and 30-40% of data points, respectively. Apparent relaxation rate constants (R_{1-1}; R_{1-2}; R_{2-1} and R_{2-2}) and population fractions (p_{01} and p_{02}) were calculated. Since α was close to 1 in all the experiments, it was set to 1 to decrease the number of variables in the fitting procedures. The T_2 data measured with the *CPMG* pulse sequence were fitted to a biexponential regression curve with four parameters:

$$M_{xy}(t) = p_{01} \cdot e^{\frac{-t}{T_{2-1}}} + p_{02} \cdot e^{\frac{-t}{T_{2-2}}} \tag{6.7}$$

where the four parameters were: p_{01}, α, p_{02}, T_{2-1} and T_{2-2}. The result parameters from these analyses were the apparent relaxation values. Their real or intrinsic values were retrieved from the two-site water exchange (2SX) analysis.

2SX analyses

The relaxation data are influenced by cellular water exchange as described in Section 2.3. The two-component T_1 values, i.e. the apparent ic R_{1-1}, ec R_{1-2}, ic p_{01} and ec p_{02} values, were analyzed according to a two-site water exchange (2SX) model in order to obtain their intrinsic values. The 2SX model presented in Equations 2.57, 2.58 and 2.59, was used to examine the five intrinsic parameters: R_{1ec}, r_{1ic}, R_{1ic0}, τ_{ic} and p_{ic}. The apparent values were accommodated by a simplex minimalization routine [84], which was modified to allow for locking of selected parameters and keeping them at constant values by varying the five intrinsic 2SX model parameters. Thereafter p_{ic} and τ_{ic} were calculated from the Equations 2.52 and 2.53.

Validation of 2SX results

In Paper II, the 2SX parameters τ_{ic} and p_{ic} were validated with a root mean square (RMS) plot [84]. This was done by varying the 2SX variables τ_{ic} and p_{ic} while holding the other variables constant. The resulting RMS errors were then plotted as a function of τ_{ic} and p_{ic}.

A χ^2 plot [84] minimizes the sum of squares of the deviations between the calculated and the experimental values:

$$\chi^2 = \sum_{i=1}^{N} \left(\frac{y_i - y(x_i; a_1 \ldots a_M)}{\sigma_i}\right)^2 \tag{6.8}$$

y_i is the i^{th} data point and $y(x_i; a_1 \ldots a_M)$ is the value of the model function with M independent model parameters (five). In our case we have to summarize the three equations for R_{1-1}, R_{1-2} and p_{01}, where each parameter has its specific standard deviation, σ_i, to evaluate our data properly (i.e. the simplex minimalization method has to be used).

If the experimental measurement errors are known, they should be used as σ_i. This provides an uneven weighting of different experimental points: the smaller the measurement error for a particular experimental point, the larger the weight of that point in χ^2. If the measurement errors (σ_i) are excluded from the χ^2 equation, i.e. $\sigma_i = 1$, a root mean square (RMS) plot is achieved.

6.4 Data analysis

The nonlinear regression method that is used is the Levenberg-Marquart method [84]. Linear curve fitting analysis can only be applied on monoexponential data (see Equation 2.29). The programs that are used for the regression analysis are; a program coded in C implemented from the book Numerical Recipes in C [84], which is open for modifications and is able to handle many data files together; a program called Originlab with manual analysis and a graphical interface (http://www.originlab.com). Other programs that have been used for data handling are Excel (2SX model), together with a minimalization routine that also was programmed in C, Graphpad Prism (figures and statistics), Matlab (figures with residuals), SPSS and Vibestat (non-parametric statistics).

6.5 Statistics

In Paper I non-parametric statistical tests were used on the experimental data. Since the number of animals in each group was less than eight , it is not correct to assume that the data have a normal (Gaussian) distribution. This use of the statistics reveals possible outliers hidden in the data which can lead to misinterpretation of the data, and the whole range of data is shown when non-parametric statistics is used instead of parametric. All results were expressed as weighted median values and range of values. Comparison between groups was made by use of the non-parametric Kruskall-Wallis test for k-independent samples. The parametric Pearson correlation test was used (n > 8).

In Paper II parametric statistical analysis was used on the experimental data. This was done in compliance with one of the Referee's request and since the parametric mean and the non-parametric median were insignificantly different. Therefore, all table results were expressed as mean and standard deviations. Comparison between groups was made by use of the parametric one-way ANOVA test for k-independent samples and the post Tukey test within groups. A root mean square (RMS)-plot of p_{ic} and τ_{1ic} was used to validate the fitted parameters in the 2SX model.

In Paper III the results were expressed as mean values in the text, as the mean $\pm$ SEM in figures and as the mean $\pm$ SD in tables. Comparison between groups was made by use of one-way ANOVA and subsequently by Fischer´s Protected Least Significant Difference (PLSD) for the physiology data and the post-hoc test Tukey for the relaxation data. Differences are noted as significant for $p < 0.05$.

7. Summary of Papers

Paper I. Paramagnetic manganese ions (Mn^{2+}) are taken up into cardiomyocytes where they are retained for hours. Relaxation parameters, T_1 and T_2, and Mn content were measured in right plus left ventricular myocardium excised from isolated perfused rat hearts. In the experiments 5 minutes washin of $MnCl_2$ were followed by 15 minutes washout to remove extracellular (ec) Mn^{2+}.

25 μM and 100 μM $MnCl_2$ elevated tissue Mn content to 6 and 12 times the level of control (0 μM $MnCl_2$). Variations in perfusate calcium (Ca^{2+}) during washin of $MnCl_2$ and experiments including nifedipine showed that myocardial slow Ca^{2+} channels are the main pathway for Mn^{2+} uptake and that Mn^{2+} acts as a pure Ca^{2+} competitor and a preferred substrate for slow Ca^{2+} channel entry.

Inversion recovery analysis at 20 MHz revealed two components for longitudinal relaxation: a short T_{1-1}; and a longer T_{1-2}. Approximate values for control and Mn-treated hearts were in the range 600-125 ms for T_{1-1} and 2200-750 ms for T_{1-2}, respectively. The population fractions were about 59 % and 41 % for the short and the long component, respectively. The intracellular (ic) R_{1-1} and R_{2-1} correlated best with tissue Mn content.

Applying two-site exchange (2SX) analyzes on the obtained T_1 data yielded results in parallel to, but also differing from, results reported with an ec contrast agent. The calculated lifetime of ic water (τ_{ic}) of about 10 s is compatible with a slow water exchange in the present excised cardiac tissue. The longitudinal relaxivity (r_1) of Mn-ions in ic water (60 (s mM)$^{-1}$) was about one order of magnitude higher than that of $MnCl_2$ in water *in vitro* (6.9 (s mM)$^{-1}$) indicating that ic Mn-protein binding is an important potentiating factor in relaxation enhancement.

Paper II. The efficacy of Mn^{2+}-ions as intracellular (ic) contrast agents was assessed in rat myocardium. The same perfusion protocol (5 minutes washin and 15 minutes washout) as in Paper I was used, except that the test substance $MnCl_2$ was replaced by MnDPDP. MnDPDP was infused in the following concentrations: 0, 30, 100, 300 and 1000 μM. After the perfusion experiments relaxation parameters and Mn content were measured in right plus left ventricular myocardium excised from the rat hearts as in Paper I.

Inversion recovery analysis at 20 MHz revealed two T_1 components: an ic and short T_{1-1} (650-251 ms); and an ec and longer T_{1-2} (2712-1042 ms). Population fractions were about 68 % and 32 %, respectively. Tissue Mn content correlated particularly well with ic R_{1-1}. Two-site water exchange analysis of T_1 data documented slow-intermediate water exchange with ic and ec lifetimes of 11.3 s and 7.5 s, respectively, and no differences between apparent

and intrinsic relaxation parameters. The relaxivity induced by Mn^{2+}-ions in ic water was as high as 56 $(s\ mM)^{-1}$, about 8 times and 36 times higher than with Mn^{2+}-aquaions and MnDPDP *in vitro*, respectively. This is as high as yet reported for any synthetic protein-bound metal chelate. Increased rotational correlation time (τ_R) between proton and electron (Mn^{2+}) spins, and maintained inner-sphere water access, might make ic Mn^{2+}-ions and Mn^{2+}-releasing contrast media surprisingly effective for T_1 weighted imaging.

Paper III. Mn^{2+}-ions enter cardiomyocytes via calcium (Ca^{2+}) channels and enhance ic proton relaxation. To prevent negative inotropy new Mn^{2+}-releasing contrast agents have been supplemented with high Ca^{2+}. The study aim was to investigate how this affects cardiac function and MR efficacy.

$MnCl_2$ based contrast agents, *Manganese* and *Manganese-Calcium* (Ca^{2+} to Mn^{2+} 10:1), were infused during 4 repeated washin-washout sequences in perfused guinea pig hearts. $[Mn^{2+}]$ were 10, 50, 100 and 500 μM. After the perfusion experiments relaxation parameters, phosphocreatine (PCr) and adenosine-triphosphate (ATP) and Mn content were measured in right plus left ventricular myocardium excised from the guinea pig hearts. During washin *Manganese* depressed left ventricular developed pressure (LVDP) by 4, 9, 17 and 53 % whereas *Manganese-Calcium* increased LVDP by 13, 18, 25 and 56 %. After experiments tissue Mn contents (nmol/g dry wt.) were: Control < 40, *Manganese* 3720 and *Manganese-Calcium* 1620. High energy phosphate compounds were at the normal level for guinea pig myocardium signifying that cell metabolism was well maintained in all three groups of hearts.

Inversion recovery analysis at 20 MHz revealed two T_1 components: an ic and short T_{1-1}; and an ec and longer T_{1-2}. T_{1-1} was reduced from 596 ms with 92 % to 47 ms in the *Manganese* group and with 86 % to 83 ms in the *Manganese-Calcium* group. T_{1-2} was reduced from 2017 ms with 66 % to 683 ms in the *Manganese* group and with 49 % to 1025 ms in the *Manganese-Calcium* group. The ic population fraction was 46 % in the control group, but 59 % and 61 % in the *Manganese* and *Manganese-Calcium* group, respectively. The 2SX analysis revealed lifetimes for ic and ec water of 9.6 s and 5.9 s, and intrinsic population fractions for ic and ec water of 62 % and 38 %, respectively. The study showed that high Ca^{2+} supplements to Mn^{2+}-releasing contrast media may be counterproductive by inducing a strong positive inotropic response and by reducing the MR efficacy.

8. Discussion

8.1 Main findings of the thesis

The results of the individual studies in this thesis have been discussed in the various papers (I-III). Thus, the present discussion mainly concerns the general findings:

1. Myocardial T_1 relaxation was resolved in two components corresponding to ic and ec water proton environment, respectively.
2. Two-site water exchange analysis revealed concordance between apparent and intrinsic T_1 data sets. The calculated long lifetimes of ic and ec water were compatible with slow-intermediate water exchange across the cardiac cell membrane.
3. It was confirmed that myocardial Mn^{2+} uptake is dependent on slow Ca^{2+} channel function and Mn^{2+}-Ca^{2+} competition, of which the latter is a determinant of both safety and MR efficacy.
4. Ic Mn^{2+}-ions provided a particularly strong proton relaxation enhancement due to macromolecular adduct formation. These powerful ic T_1-agents contribute strongly to future cardiac MRI at low μM Mn^{2+}-concentrations.

8.2 Biexponential T_1 in rat myocardium

8.2.1 Nonlinear and linear regression analyses

In Paper I dealing with 0 μM, 25 μM and 100 μM $MnCl_2$, mono- and biexponential fits were demonstrated and verified with residual analyses in Figure 4-6 of the Paper. In Paper II quantitative analyses of the mono- and biexponential fits were not reported due to the thorough analysis carried out in Paper I, where the conclusion was that the biexponential fits matched the experimental data properly. Only qualitative results of the mono- and biexponential fits were displayed in Figure 2 of the Paper. All the mono- and biexponential T_1 data of Paper III are listed in its Table 2, where T_1 was more adequately described by a biexponential behavior.

In this section quantitative estimates of the goodness of fit and of how well the model fits the data of Paper II are shown. Nonlinear regression and residual analyses were used on the data. In addition, linear and monoexponential regression analyses were applied to a single control heart.

The goodness of fit, the choice of model, and errors in the fitting parameters are all factors to be considered when doing regression analysis. The goodness of fit is validated by the regression coefficient, R^2, and the choice of model is validated by the reduced chi-square coefficient χ^2/D_{0F}. Regression plots and their residuals provide good insight into the quality of the fitted data, and reveal proper information about the fitting procedure. Residuals are the deviations of the data points from the fitted curve (M_z(experimental) - M_z(fitted)). Perhaps the most important information obtained is whether there are any hidden variables, i.e. if more parameters are needed to fit the experimental data properly. Normally, if the curve fits the data well, the data point deviations are expected to be randomly distributed around the fitted curve, that is, no trend in the residuals. Therefore, the curve fitting implies when, but not how, the chosen model needs improvement.

As seen in the residual analyses (Table 8.1) there were no significant differences between the single exponential fits with or without MnDPDP. There was also a trend in the residuals (Figure 8.1) indicating that the model needed more parameters to fit the data properly. Increasing the number of parameters from three (α, T_1 and M_0) to five (α, p_{01}, p_{02}, T_{1-1} and T_{1-2}) decreased the range of the residuals from around 7.3 % (Table 8.1) to 0.9 % (Table 8.2) of the maximum proton signal, M_0, where the residuals were calculated (in %) as follows:

$$Residuals = [max(abs(Residual)) + min(abs(Residual))] \cdot 100\%/(2 \cdot M_0) \qquad (8.1)$$

Table 8.1: Residuals, R^2 and χ^2/D_{0F} from the monoexponential regression analysis in Paper II. The residuals are expressed as mean $\pm$ standard deviations (SD) and n is the number of hearts in each group.

MnDPDP (μM)	*n*	*Residuals* (%)	R^2	χ^2/D_{0F}
0	4	6.9 ± 0.2	0.998	4.94
30	4	7.0 ± 0.4	0.998	4.43
100	6	7.4 ± 0.5	0.998	3.60
300	6	7.6 ± 0.7	0.997	6.88
1000	4	7.4 ± 0.3	0.997	5.69

The average regression and reduced chi-square coefficients (see vertical entries R^2 and χ^2/D_{0F} in Table 8.1 and 8.2) were: 0.998 and 5.0 ± 1.2 for monoexponential fits and 0.999 and 0.12 ± 0.01 for biexponential fits, respectively. The errors of the fitted parameters in % were: 1.8 ± 0.4 for M_0, 3.6 ± 0.5 for T_1 in the monoexponential analysis; and, 4.2 ± 1.1 for p_{01}, 7.8 ± 1.8 for p_{02}, 3.4 ± 0.5 for T_{1-1} and 7.2 ± 0.8 for T_{1-2} in the biexponential analysis.

Even though the regression coefficients in Table 8.1 were close to one for the monoexponential fits, both the residuals and the reduced chi-square coeffi-

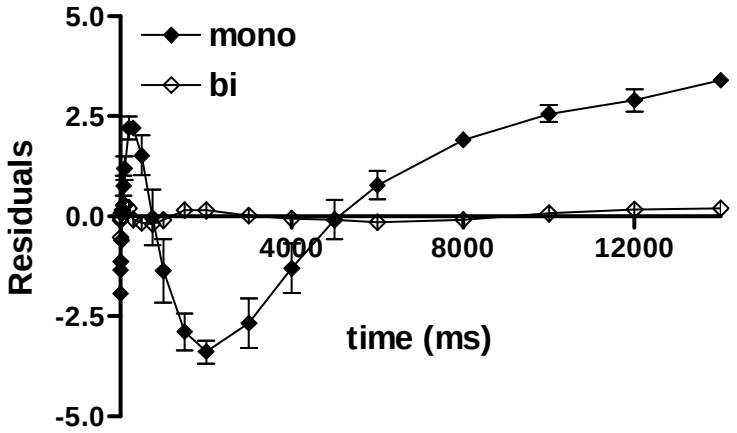

Figure 8.1: Mean residuals ± SD of all the mono- and biexponential T_1 data in Paper II.

Table 8.2: Residuals (Mean ± SD), R^2 and χ^2/D_{0F} from the biexponential regression analysis in Paper II, *n* is the number of hearts in each group.

MnDPDP (μM)	*n*	*Residuals* (%)	R^2	χ^2/D_{0F}
0	4	0.99 ± 0.03	1.000	0.114
30	4	0.78 ± 0.04	0.999	0.122
100	6	0.87 ± 0.06	0.999	0.105
300	6	0.95 ± 0.09	0.999	0.117
1000	4	0.87 ± 0.04	0.999	0.133

cients reveal that another model should be chosen to fit the data. Figure 8.1 and Table 8.2 confirmed that the biexponential model was a good choice.

Monoexponential and linear analyses

The T_1 values in control rat hearts were close to the published values of approximately 1000 ms in isolated hearts at 0.47 T [20, 100]. In Figure 8.2 an example of a monoexponential curve fit with T_1 = 941 ms is shown. The fit is good (R^2 = 0.998), but the χ^2/D_{0F} value is large (~ 5) indicating that another model is required.

In Figure 8.3 a linear regression curve fit of the same T_1 data is shown. The linear function in Equation 2.29 (displayed in the figure) was used to fit the data. The T_1 value (1972 ms) is larger than the expected value of 1000 ms as indicated in the figure with a dotted line, and the data do not look linear. Nevertheless, the calculated R^2 and χ^2/D_{0F} values are indicating a good fit ($R^2 \sim 1$ and $\chi^2/D_{0F} \sim 0$). This can be explained by the observation that the

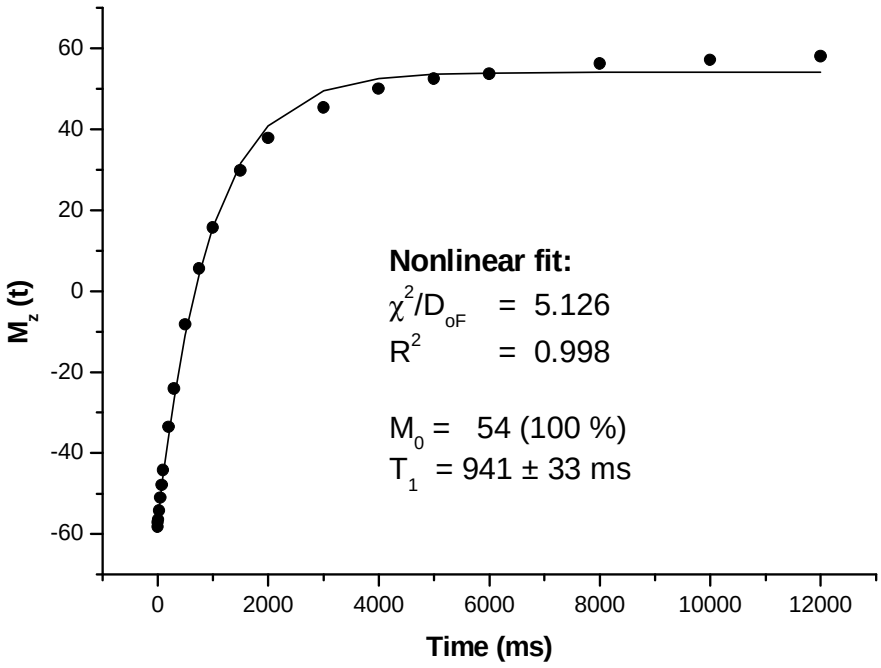

Figure 8.2: Monoexponential regression analysis of the T_1 data from a control heart, where the resulting T_1 equals 941 ms.

experimental data are symmetrically distributed around the linear regression curve, which will be treated as random noise by the program. Therefore, it is valuable to look at the plotted graphs, which in this case should suggest that the model is not appropriate for the data.

From Figure 8.2 it can be seen that the monoexponential curve fits the initial data well (67 % of the curve), but that the fit is poor from about 2000 ms (33 % of the curve). Therefore, the estimated T_1 value is closer to the short component from the biexponential analysis ($\sim$ 650 ms) than to the long component ($\sim$ 2700 ms). In Figure 8.3 the initial curve seems to have one slope, and the remaining curve another, in concordance to one short and one long T_1 value, respectively. The average curve is then somewhere in between the slope of the short and long components.

In conclusion, the results in this section show that nonlinear regression with residual analysis is the best tool for T_1 analysis and that a biexponential approach is justified on basis of the data. In addition, these results show that when monoexponential and linear regression analyses are used, important information about the data can be lost due to wrong approximations. Therefore, careful regression analyses should be carried out on the T_1 data, analyzing the data with more than one T_1 component.

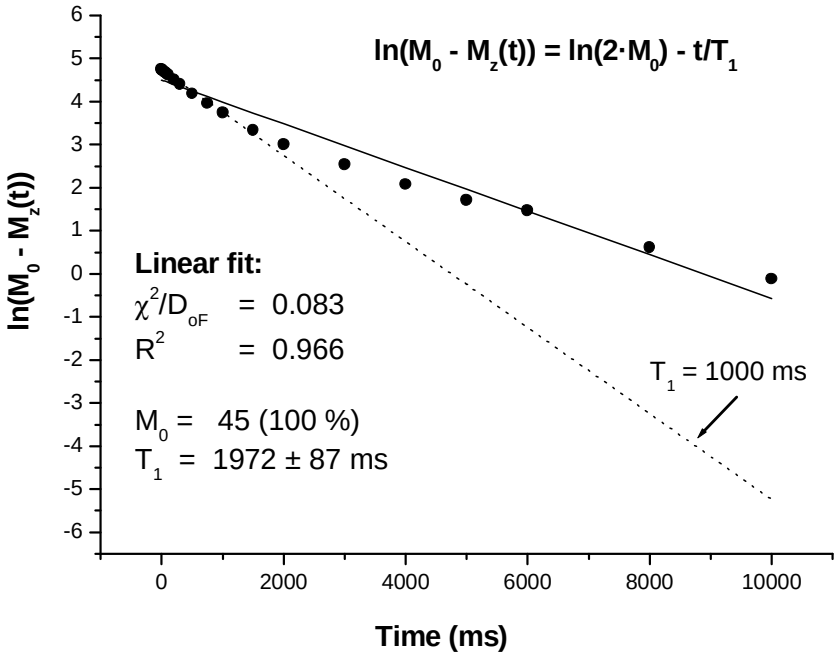

Figure 8.3: Linear fit of the T_1 data from the same control heart as in Figure 8.2, where the resulting T_1 equals 1972 ms. The dotted line represents a T_1 value of 1000 ms.

8.2.2 Three T_1 components

In Paper I, Figure 4-6, there was an indication of a third initial relaxation component in the residuals of the biexponential fits. Since the fitting of the data was improved with inclusion of more T_1 components, the data in the group with 100 μM $MnCl_2$ in Figure 6 (Paper I) was reanalyzed with one, two and three T_1 components.

In Figure 8.4 the results from the nonlinear regression and residual analyses for these hearts (n = 4) are shown. The result parameters displayed in the figures show that all the estimated mono- and biexponential parameters do not differ much within the group, i.e. small SD's. With three components, however, large SD's are found for p_{01} (SD = 64 %) and the corresponding T_{1-1} (SD = 80 %).

The errors in the estimated mono-, bi- and three exponential curves are shown in Table 8.3. Monoexponential curve fitting revealed large chi-squared ($\sim$ 21) and residual values, but the regression coefficients were almost ideal (=1) and the errors of the fitted parameters were insignificant (see Figure 4-6 a in Paper I). As shown previously, the monoexponential fit was good, but the model needs more parameters to describe the data properly, and the average T_1 values are gross approximations of the real T_1 values. The fitting of the T_1 data were improved with a biexponential analysis, with 98 % further reduction of

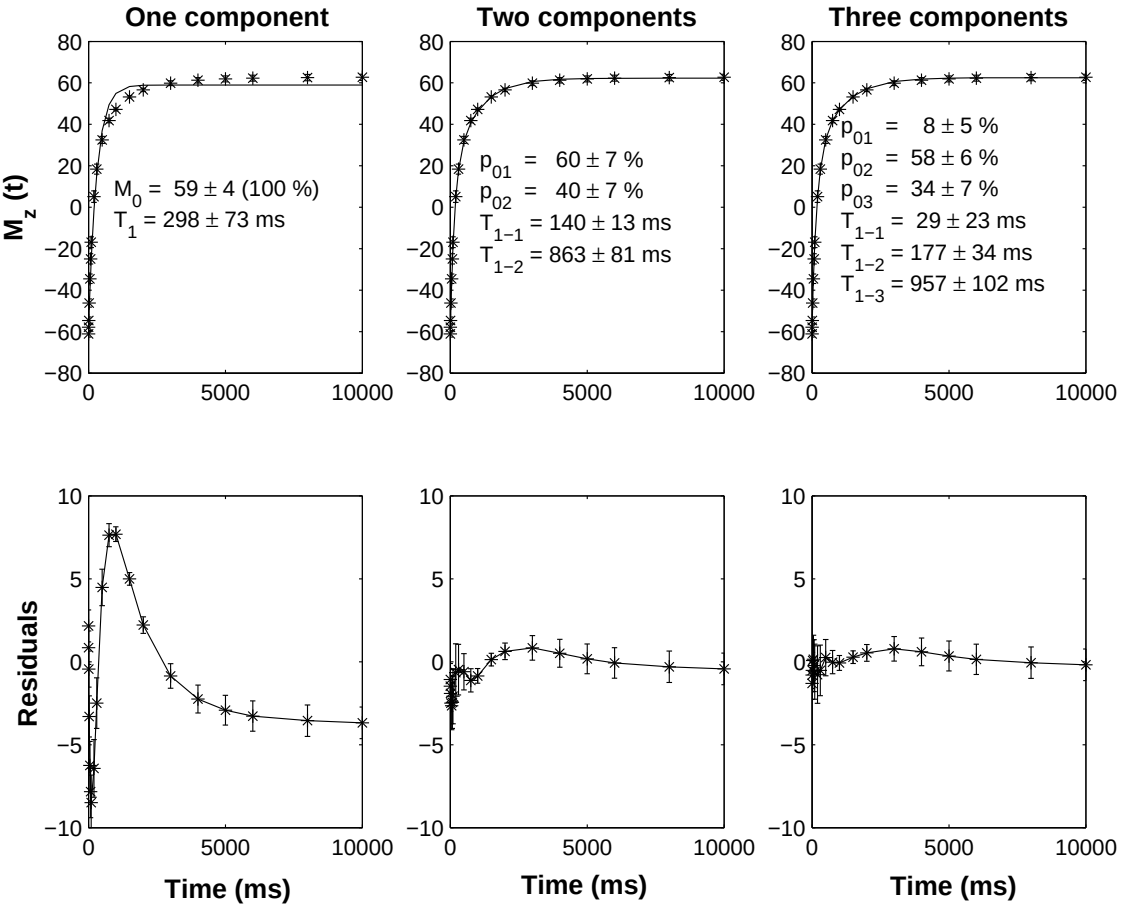

Figure 8.4: Hearts loaded with 100 μM $MnCl_2$ fitted with one- two- and three components (upper panel) with their successive residual plots (lower panel). The results are expressed as mean $\pm$ SD.

χ^2/D_{0F} and 87 % further reduction of the residuals. Application of a three exponential analysis to the data gave a insignificant reduction of the mean χ^2/D_{0F} values and the residuals with 1 % and 2 %, respectively, but the SD for the χ^2/D_{0F} value is large (92 %).

Table 8.3: The errors in the estimated regression curves from Figure 8.4. The values are given in mean $\pm$ SD.

components	χ^2/D_{0F}	R^2	*Res*(*min*)	*Res*(*max*)
1	20.52 ± 4	0.992	-7.611 $\pm$ 0.427	5.218 $\pm$ 0.643
2	0.38 ± 0.14	0.999	-0.886 $\pm$ 0.195	0.840 $\pm$ 0.126
3	0.24 ± 0.22	0.999	-0.412 $\pm$ 0.086	0.988 $\pm$ 0.622

These results show that on the basis of the collected data, i.e. the number of data points, the range of *TI* values, and the signal-to-noise ratio, it was

not statistically significant to extract three T_1 components from the *ex vivo* hearts with confidence. Therefore it would be wrong to assign the short third T_1 component to a physically meaningful ic water compartment.

8.2.3 Physical conformity of two-compartmental data

Even though a third component may be hidden in the data, the detected two component T_1 data can relate directly to the ic and ec (T_{1ic} and T_{1ec}) cell water. Their population fractions (p_{ic} and p_{ec}) are in accordance with cell comparment fractions in the literature. Clarke *et al.* [25] have, in addition to calculating volumes *in vivo*, calculated water contents and volumes in *ex vivo* blotted, freeze-clamped and crystalloid perfused rat hearts (see Table 8.4). In this study the blotted *ex vivo* hearts had an ic water content of 60 %. This is close to all the estimated population fractions of the short T_1 components found in this thesis, and close to the commonly accepted *in vivo* ic volumes of 73 % - 74 % determined as inulin space [24, 28] and 70 % determined as mannitol space in rat myocardium [28].

Table 8.4: Water content and volumes in *ex vivo* and *in vivo* rat hearts, where the volumes are expressed in ml/g wet wt. (% of the total water in parenthesis).

Rat hearts	**Refs.**	**wet/dry wt.**	$\mathbf{V}_t$	$\mathbf{V}_{ec}$	$\mathbf{V}_{ic}$
In vivo	[25]		0.77	0.21 (27%)	0.56 (73%)
In vivo	[24]		0.79	0.21 (26%)	0.58 (74%)
In vivo	[28]		0.79	(28%)	(72%)
Blotted	[25]	5	0.80	0.32 (40%)	0.48 (60%)
Freeze-clamped	[25]	6.67	0.87	0.51 (59%)	0.36 (41%)
Freeze-clamped	[25]	7.1	0.89	0.54 (61%)	0.35 (39%)
NMR analysis	[25]	10	0.92	0.71 (77%)	0.22 (23%)

In addition to water volumes, the NMR analyses of Clarke *et al.* [25] with isolated rat hearts, wet/dry wt. values from different perfusion and post-perfused conditions were calculated (Table 8.4). These experiments were sensitive to the rate of perfusion being used. In Paper I and II most of the hearts were weighed before and after freeze-drying. The wet/dry wt. was 5, which is identical to the value given by Clarke *et al.* [25] for blotted hearts. This factor has been used as a converting factor to obtain molar concentrations in tissue water.

Different studies have shown that the relaxation times measured in tissue kept at a stable temperature did not change within one hour. Brurok *et al.* [20] showed that the relaxation time constants in control hearts experiencing global subtotal ischemia (flow < 1 % of normal flow) in 95 min did not change

even though ATP decreased with 80-85 %, only that uptake of new Mn^{2+}-ions was greatly reduced. Kang and Gore [54] did not find any changes in the T_1 values within 1 hour. In these two studies where monoexponential T_1 values were extracted no changes were detected. If Mn^{2+}-ions leak out of the ic compartment due to cell membrane disintegration, the biexponential fit would be more sensitive to redistribution of ic and ec relaxation agents. Belton and Ratcliffe [7] in a review article listed T_1 values in different tissue over a period of time and observed no changes in one-compartment systems, and small or no changes in two-compartment systems. In the present studies some T_1 measurements were done immediately, and others two hours later, after excision of hearts no changes in the T_1 values were observed.

8.3 2SX analysis of T_1 data

In Paper I-III a 2SX analysis was applied to the measured apparent biexponential T_1 data (T'_{1ic}, T'_{1ec}, p'_{1ic} and p'_{ec}) to obtain their intrinsic values (T_{1ic}, T_{1ec}, p_{1ic} and p_{ec}) and to estimate the lifetime of water in the ic compartment (τ_{ic}). This has previously not been done in cardiac tissue or with Mn-compounds as *CA*'s. As one of the Referee's on Paper I stated, the use of ic Mn^{2+}-agents will make for a new, and very important, application of the 2SX theory. All other published papers dealing with the 2SX model used Gd-based *CA*'s that were trapped in the ec space.

8.3.1 Slow-intermediate water exchange

Since Mn^{2+}-ions reside inside the cells the cellular water exchange is of main concern. If Equation 2.44 holds, then the water exchange is considered slow. The 2SX model can be used to analyze all the possible exchange situations including intermediate exchange. When using the 2SX model it was postulated that the vascular exchange was fast (Figure 2.12). The cellular water exchange values in all three Papers were smaller than the differences in the relaxation rate constants between the two compartments under study (Table 8.5). It was observed that not only the apparent R'_{1ic}, but also R'_{1ec}, correlated with Mn content in the hearts. Therefore, a slow-intermediate exchange model was tested for description of the R'_1 values by using the 2SX model.

These results were supported by the findings of Labadie *et al.* [64] and Landis *et al.* [65, 66], who calculated water exchange parameters in yeast and skeletal muscle tissue with the *CA* on the outside of the cells by using the 2SX model. A linear relationship between the accumulated Mn and the intrinsic ic relaxation rate constants (R_{1ic}) was found. Biexponential T_1 values were confirmed for both control and Mn-enhanced hearts due to the long ic lifetime of

Table 8.5: Results from the 2SX analysis in Paper I-III: Intrinsic ic and ec relaxation rate constants, ic population fractions and ic water exchange.

Paper	R_{1ec} (s^{-1})	R_{1ic0} (s^{-1})	p_{ic} (%)	τ_{ic}^{-1} (Hz)
I	0.44	0.88	55	0.10
II	0.40	1.16	59	0.09
III	0.44	1.15	62	0.10

water. However, the results obtained here differ from those of Labadie *et al.* [64] and Landis *et al.* [65, 66] in control tissue and at low concentrations of *CA*. In their studies they observed a monoexponential T_1 at low ec [Gd-agent]. This might be due to a smaller efficacy of the ec *CA* compared to ic Mn^{2+}-ions and that the water exchange is an order of magnitude smaller than in yeast and muscle cells.

In control heart tissue the difference in T_1's between ic and ec water was large, i.e. $T'_{1ec} \sim 2700$ ms (close to the T_1 of the applied perfusion medium) and $T'_{1ic} \sim 650$ ms, where the ic space was ~ 60 % and the ec space ~ 40 % of the cell volume. In skeletal muscle tissue, for example, with a ec population fraction of ~ 10 % ec cell volume, which makes it more difficult to obtain biexponential T_1 values in control tissue.

The difference in the mean relaxation values of control hearts is: $\Delta R_1 = |R'_{1ic} - R'_{1ec}|$ = 1000/650 - 1000/2700 = 1.16 s^{-1}, which is larger than the mean water exchange value of 0.1 s^{-1} (Table 8.5), i.e. slow-intermediate water exchange is confirmed. Since the R'_{1ic} is expected to increase more than R'_{1ec} with increasing addition of Mn^{2+}, ΔR_1 increases and is never smaller than the water exchange value. In order words, based on this criterium a slow exchange situation appears. Even in a more *in vivo* like situation where blood is the perfusion medium, T_1 range of 1600-1000 ms [31, 109], a situation where T_1 becomes monoexponential will not occur due to the fact that: $|R'_{1ic} - R'_{1ec}|$ = 1000/650 - 1000/1000 = 0.54 $>$ 0.1 s^{-1}, i.e. slow-intermediate exchange.

In Paper II the p_{ic} and τ_{ic} values were validated by a RMS plot (Figure 5, Paper II), which confirmed slow-intermediate cellular exchange. The RMS plot had a minium around p_{ic} = 0.59 and τ_{ic} = 11.3 s. The distribution around p_{ic} is almost symmetric and the uncertainty in the estimated value is small, whereas for τ_{ic} the error distribution is asymmetric, i.e. $\tau_{ic} > \sim 8$ s. The uncertainty is small below, but infinite above, the minimum value of 11.3 s. This means that the ic lifetime parameter is not very dependent on the analysis, and has to be long.

These findings are important since if the cellular water exchange in the myocardium is slow-intermediate, this will have implications on the characterization of the myocardial microcirculation. Myocardial perfusion is an impor-

tant factor of microcirculation as is determination of regional intracapillary myocardial blood volume (RBV) [10, 107, 109].

8.4 Comparison with other studies

As described in Section 2.2.1, the T_1 process is exponential and in the literature it is common to present monoexponential T_1 values from tissue. Some examples of average T_1 values in control heart tissue are listed in Table 8.6.

Table 8.6: Monoexponential T_1 literature values from myocardium in different species, where all the experiments were done on isolated hearts except from the *in vivo* human hearts.

References	T_1 (ms)	**Field strength** (T)	**Species**
Southon *et al.* [100]	800	0.47	pig
Brurok *et al.* [20]	1000	0.47	guinea pig
Skjold *et al.* [96]	1000	1.5	human
Wacker *et al.* [109]	1200	1.5	human
Donahue [29]	1100	4.7	rat
Judd *et al.* [51]	1100	4.7	canine (dog)
Ward *et al.* [110]	1700	7	porcine (pig)

In the present studies more detailed T_1 analyses of relaxographic data at 0.47 T revealed that T_1 was biexponential in excised rat myocardium. Some authors have tried to apply a biexponential analysis on their T_1 data from heart specimens by the use of relaxography [75], field-cycling relaxometry ($2.5 \cdot 10^{-4}$ - 1.2 T) [101] and imaging (4.7 T) [29, 52].

Spiller *et al.* [101] measured NMRD profiles on different non-perfused tissues (liver, heart, pancreas, spleen, skeletal muscle, fat and kidney) excised from rabbits, before and after intravenous injection of $MnCl_2$. They were in particular studying whether the T_1 data could be resolved in more than one relaxation component due to compartmentalization of tissue water and contrast agent. Therefore they chose 15 data points ranging in time up to $1.5 \cdot T_1$ and 7 data points at $7 \cdot T_1$ for the monoexponential T_1 analyses, but increased the number of data points to 106 for the biexponential T_1 analyses. The uncertainty of the monoexponential fits increased with increasing $[MnCl_2]$, and no Mn was detected in the skeletal muscle tissue and fat by ICP. The most interesting finding in this study was that although most of the tissues were well described by monoexponential T_1's at any given fields, except from varying results in the renal cortex and fat, the monoexponential NMRD profiles of normal hearts from different rabbits varied significantly, by as much as 100 % at low fields. That is, two longitudinal relaxation rates were required at

each field to describe proton relaxation in heart tissue from control rabbits. This was explained by restricted or slow water exchange, i.e. compartmentalization.

There are not many studies done with excised and perfused hearts. Mauss *et al.* [75] did relaxographic measurements on hearts excised from the rats, and hearts perfused, in a 0.47 T MR spectrometer. The perfusate was a Tyrode solution comparable to the KHBB perfusion medium used in the present studies, but where they added Dextran (60 g/l) to avoid edema formation. In the perfused hearts $MnCl_2$ was added to the perfusate in different concentrations, but no Mn^{2+} washout phase was included in the experiments before the T_1 and T_2 measurements took place. Therefore, most likely Mn^{2+}-ions were present both in the ec and ic compartments. The aim of the study by Mauss *et al.* [75] was to show a compartmentalization of the mobile water in perfused and living organs by decomposition of the relaxation curves by adding a paramagnetic agent in the perfusate. They were not able to calculate biexponential T_1 values in control hearts in any of their experiments. As can be read out of their Materials and Methods section they used data points in the range 15-2000 ms, which will most likely cover a short component T_1 value. Assuming a T_1 value of 2700 ms in their perfusate (comparable to the KHBB perfusion medium used in Paper I-III), their short TI range will not render a reliable long T_1 ec value because the lack of representative data points. However, for [$MnCl_2$] larger than 10 μM biexponentiality of T_1 was observed, where the long component R_{1l} increased lineary with increasing [Mn^{2+}]. Since they have no washout period, their observed R_{1l} linearity is most likely due to an increase in ec [Mn^{2+}]. Their T_2 analyses showed two components, and they observed with a linearity between [$MnCl_2$] and R_{2l}, but the short component exhibited no correlation with [$MnCl_2$]. The T_2 results supported what they previously found for T_1's. Their T_1 and T_2 values and population fractions are not comparable to the values in the present studies due to different experimental designs, the main difference being lack of a washout period in the experiments of Mauss *et al.*.

Donahue *et al.* [30-32] perfused rat hearts and used gadolinium based contrast agents to study T_1 and water exchange. In addition, Donahue [29] used $MnCl_2$ in one experiment. T_1 values were estimated from changes in image contrast using an ultrafast gradient echo (GRE) imaging technique at 4.7 T. In the $MnCl_2$ study Donahue [29] used different concentrations (0, 100, 500, 1000, 500 and 0 μM) of $MnCl_2$ where she found biexponential T_1 values above 100 μM. Retention of biexponentiality after the second 0 μM $MnCl_2$ perfusion period supports the findings in this thesis, where this perfusion entry may be considered a washout period. Donahue suggested that this discrepancy between the two 0 μM $MnCl_2$ control perfusion periods was due to cell damage. However, a more likely explanation is that there is a retention of ic Mn^{2+}-ions causing the biexponentiality. Such an interpretation is in agreement with the observations in this thesis.

Based on the studies with ec Gd-agents, Donahue *et al.* concluded with a cellular exchange of $8-27$ Hz corresponding to lifetimes of 125 - 37 ms. Judd *et al.* [51, 52] and Bauer *et al.* [6] also proposed a rapid water exchange across the cardiac cell membrane in their myocardial perfusion studies.

Donahue *et al.* observed monoexponential T_1 in their control hearts. This result was supported by the assumption that the ic and ec T_1 values ($\sim$ 1000 ms) were almost equal. Addition of Gd-based *CA* with a low relaxivity of 4 (s mM)$^{-1}$ resulted in tissue contrast. The corresponding T_1 analysis yielded monoexponential behavior at concentrations below 2 mM.

The most likely explanations for the discrepancies between our results and those from the myocardial perfusion literature, where T_1 is extracted from variations in image contrast, lie in the methods used for assessment of tissue T_1. Extracting bicomponent exponentials for T_1 based on image contrast requires good *SNR*. Relaxography measurements yield good *SNR*, which might be a problem in imaging. Secondly, the dynamic range of the inversion time (TI) has to cover both the T_1 components to be detected, and the number of data points has to be sufficient for accurately fitting the biexponential time constants. In the literature, the data are usually forced into a monoexponential fit with one T_1 component. For example, if only very short TI values are used, it is impossible to differensiate between fast and slow exchange. Since there is not enough time for exchange to take place it cannot have an impact on the magnetization and thus the signal intensity. As discussed by Hazlewood *et al.* [44] the initial slope is the same in a slow and fast exchange situation (Figure 8.2). If a compartment is small, as in the vascular space of the heart or the ec compartment in skeletal muscle tissue, the magnetization will be difficult to detect experimentally if water is in slow exchange with the rest of the tissue. However, for skeletal muscle tissue Landis *et al.* [65, 66] have been able to differentiate between ic and ec tissue water at sufficiently high concentration of ec *CA*.

In Section 6.3.1 a way of selecting the proper TI values is outlined, but this method requires an educated guess about the expected T_1 values that can be investigated with pilot experiments. Therfore, relaxography is the best suited method for T_1 and T_2 measurements in solutions and of tissue samples. Careful planning of the experimental conditions is required if biexponential T_1's are to be extracted from contrast changes as a function of the added relaxation agent.

8.4.1 Physiological determination of τ_{ic}

Most of the studies carried out in this field are done on other organs or tissues than the heart. Many studies have been done on simple erythrocytes [31, 46, 66, 102], yeast cells [64], muscle cells [44, 65, 66, 97] and brain tissue [65,

114]. These cells are different from heart cells in many ways such as size, water permeability of the cell membranes, and the ratios between the ic and ec compartments.

Since the lifetime of water in a tissue compartment is a physiological constant, it can be calculated if the cell volume (V), surface area (A) and the permeability (P) of the cell membrane are known:

$$\frac{1}{\tau} = \frac{P \cdot A}{V} \tag{8.2}$$

In most of the published work on two compartment systems and water exchange erythrocytes have been studied. The "erythrocyte" water exchange is fast (100 Hz) due to an extremely high P for water of the cell membrane, a small intracellular compartment and a large A/V ratio (Table 8.7). The larger the cell, the smaller the A/V ratio.

Mammalian cells are larger than erythrocytes and the value of P is smaller. Labadie *et al.* [64] has studied yeast cells and found a water lifetime of 700 ms and a P value of $1.2 \cdot 10^{-4}$ cm/s. Landis *et al.* [65, 66] calculated an ic lifetime of 1.1 s in skeletal muscle tissue, which would imply a P value of $13 \cdot 10^{-4}$ cm/s , i.e. an order of magnitude larger than for yeast cells, but smaller than for erythrocytes (Table 8.7). They were using Equation 8.2 with the ic volume to calculate the ic water exchange rate (τ_{ic}^{-1}), and the following approximations were done: For an infinitely long cylinder the radius (r) is much smaller than the length (l), i.e. $A/V = 2(\pi \cdot r(r+l))/\pi \cdot r^2 \cdot l \sim 2/r$ (muscle cells). The A/V ratio was approximated with $\sim 3/r$ for a sphere (yeast cells).

Table 8.7: Literature A/V ratios, P, τ_{ic} and τ_{ic}^{-1} values in different cell types. The results are taken from Labadie *et al.* [64] and Landis *et al.* [65, 66].

Parameters		**Erythrocytes**	**Yeast cells**	**Skeletal muscle cells**
A/V	(μm^{-1})	1.7	1.2	0.07
P	(cm/s)	$50 \cdot 10^{-4}$	$1.2 \cdot 10^{-4}$	$13 \cdot 10^{-4}$
τ_{ic}	(s)	0.01	0.7	1.1
τ_{ic}^{-1}	(Hz)	100	1.43	0.91

A confocal microscopic study of rabbit, ferret and rat cardiomyocytes [90] showed that the cell volume of each is almost 500 times that of the yeast cell, meaning a 8 times smaller A/V ratio of 0.15 μm^{-1}. This would increase the value of τ_{ic} with one order of magnitude, i.e. to 6 s (0.18 Hz), which is close to the values found in the present studies (Table 8.5). Cardiomyocytes are large, oblong cells with a diameter of 10-30 μm and length 80-140 μm [83]. When this information is used to calculate the A/V ratio via the approximation used by Landis *et al.*, values from 0.13 to 0.4 μm^{-1} are obtained.

In a study carried out by Rose *et al.* [88] a very small P value in cardiomyocytes ($0.15{\cdot}10^{-4}$ cm/s) of mongrel dogs was calculated. This P value was calculated from the value 4200 cm^2/g for the cardiac surface area, 0.15 ml/g for the interstitial space (V_e), and the sarcolemmal permeability-surface product per unit interstitial space ($k_{m_w} = p_e/V_e$, where p_e is the population fraction of the interstitium) for water of 0.41 Hz. These values give an A/V_e ratio of 0.28 μm^{-1}, which is in concordance with the values above. Donahue [29] in her PhD thesis (p 127-128) discussed the results found by Rose *et al.*. She questioned this low P value, and used the P value of erythrocytes instead together with the assumed A/V ratio to calculate a cellular exchange of 123 Hz. It is highly unlikely the cardiomyocytes are as permeable to water as the erythrocytes. Therefore her estimated exchange frequency has to be wrong. It is not known what the permeability in cardiomycytes is, but the A/V ratio has to be in the range of 0.13-0.4 μm^{-1} as outlined above. When using the cellular exchange rate of 0.1 Hz, a P value of $0.015{\cdot}10^{-4}$ cm/s is found. This is lower than the P values estimated in the other cells in Table 8.7 and by Rose *et al.* [88], but an appropriate value for the *ex vivo* rat hearts in the present studies.

8.5 Physiology and Mn^{2+}-Ca^{2+} relationships

Cell entry mechanisms and intracellular efficacy of Mn^{2+}-ions in ventricular myocardium from rats and guinea pigs were studied with the use of $MnCl_2$ and MnDPDP. In particular, interactions between Mn^{2+} and Ca^{2+} were examined in detail in Paper I and III.

8.5.1 Basic ion physiology

As already stated in Chapter 4 and in Paper I-III, Mn^{2+}-ions compete with other divalent cations in living cells, and with Ca^{2+}-ions in particular [9, 15]. Figure 8.5 shows how ec Mn^{2+} competes with ec Ca^{2+} for influx via L-type Ca^{2+} channels in the sarcolemma. The main reason for this resides in the affinity of Mn^{2+} to binding sites in slow channels, i.e. affinity is higher than for Ca^{2+} but not high enough to cause a total blockade. Thus Mn^{2+}-ions act differently from organic slow channel inhibitors and are true Ca^{2+} competitors [9].

Mn^{2+} enters the cytosolic pool but may distribute to cell organelles. Whereas little is known about entry into sarcoplasmic reticulum, the main Ca^{2+} store, mitochondria are known to accumulate a considerable fraction of cell Mn^{2+}. Thus β-adrenergic stimulation may redistribute Mn^{2+} from a cytosolic pool to mitochondria [49] by promoting Mn^{2+} entry via activated Ca^{2+} uniports. In the matrix 95-98 % of Mn^{2+} is bound to macromolecules and there is reason

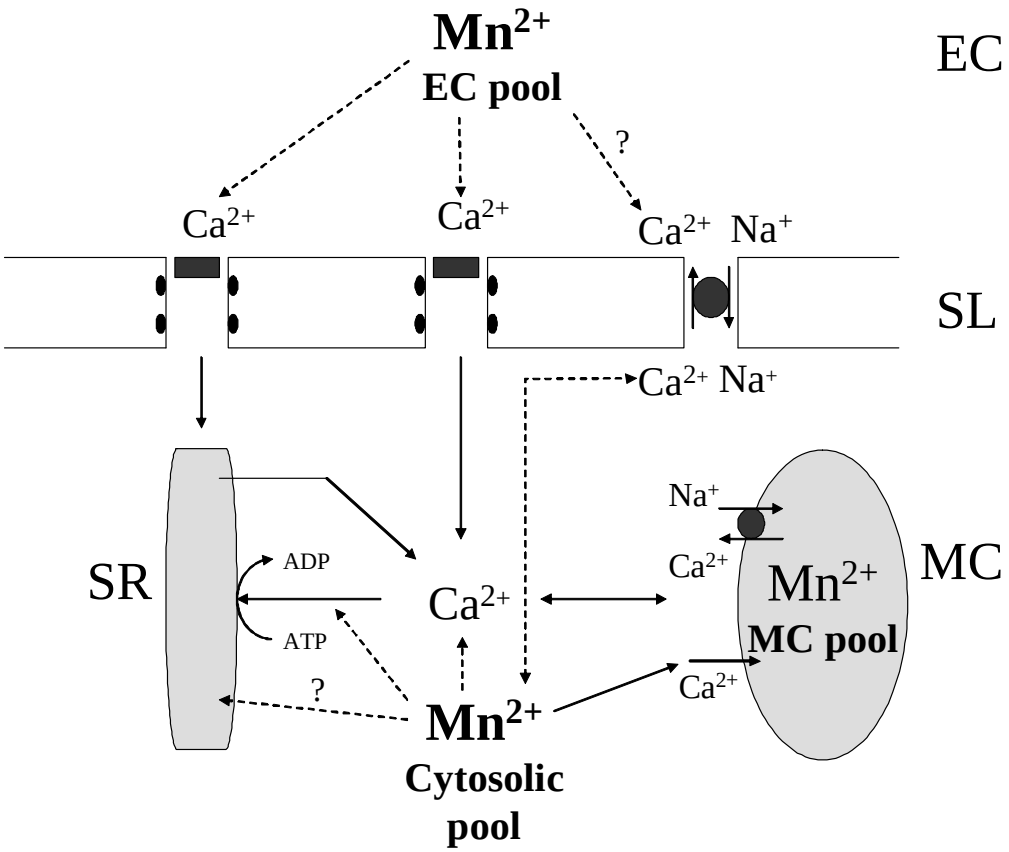

Figure 8.5: Mn^{2+} pathways and cellular distribution. EC: extracellular; SL: sarcolemma; SR: sarcoplasmic reticulum; and, MC: mitochondria.

to believe that $[Mn^{2+}]$ is lower than in cytosol. Together with a high intramitochondrial electronegativity this may explain, at least partly, the ability of cardiomyocytes to retain Mn^{2+}-ions intracellularly for hours.

As indicated in Figure 8.5 Mn^{2+}-ions may also compete with Ca^{2+} for transport via the Na^{+}-Ca^{2+} exchanger (NCX). This transporter mainly works in the antegrade mode, moving Ca^{2+} out of matrix and out of cytosol in exchange with Na^{+}. However, there is ample evidence that the sarcolemmal NCX may act in the reverse mode, i.e. promoting Ca^{2+} influx during the early phase of cell membrane depolarization. It has been reported [9] that Mn^{2+} has a higher affinity than Ca^{2+} for the sarcolemmal NCX.

From the above some major points emerge that were partly confirmed and partly strengthened in the present thesis. Thus these basic properties of Mn^{2+}-ions were apparent in *ex vivo* heart experiments:

- During perfusion with high $[Mn^{2+}]$ negative inotropy was transiently induced, but was rapidly reversed thereafter.
- Even when ec $[Mn^{2+}]$ and ec $[Ca^{2+}]$ were in the μM and the mM range, re-

spectively, there was an avid uptake of Mn^{2+} during once-through coronary perfusion.

- During perfusion with high $[Mn^{2+}]$ combined with high $[Ca^{2+}]$ less negative or even positive inotropy was transiently induced.
- Variations in ec $[Ca^{2+}]$ influenced the myocardial uptake of Mn^{2+}-ions.
- And, finally, myocardial relaxation enhancement reflected the Mn content.

8.5.2 Negative inotropy

Rat hearts (Paper I and II) and guinea pig hearts (Paper III) demonstrated an immediate, but rapidly reversible, depression of LVDP when subjected to high $[Mn^{2+}]$ at physiological $[Ca^{2+}]$. In Figure 8.6 LVDP is significantly depressed at concentrations higher than 25 μM of $MnCl_2$ and 300 μM of MnDPDP. The observed responses are due to Mn^{2+}-Ca^{2+} antagonism and are in concordance to earlier studies [18]. Also, the present data confirm findings indicating that $MnCl_2$ is about ten times more potent in depressing cardiac contractility than MnDPDP [16-18].

In one group of 100 μM $MnCl_2$ hearts, nifidipine was already present in the perfusate thereby promoting a prior inhibition of slow Ca^{2+} channels (Paper I). While Mn accumulation only was inhibited by 70 %, LVDP dropped by 91 %. This supports the hypothesis that Mn uptake into cardiomyocytes may also occur by other pathways. As discussed more thoroughly in Paper I and III divalent metal ion transporter (DMT1) proteins, or more likely the NCX, may be alternative pathways for Mn^{2+}-ions (Figure 8.5).

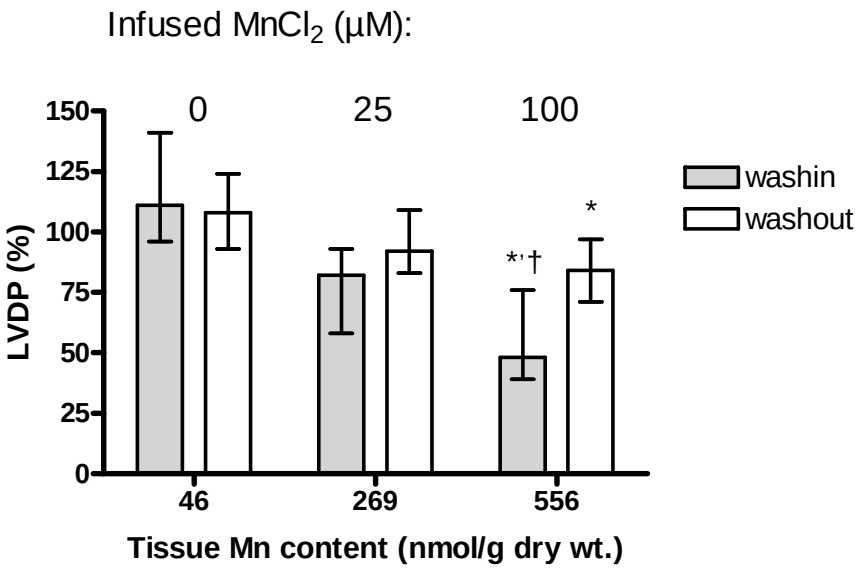

(a)

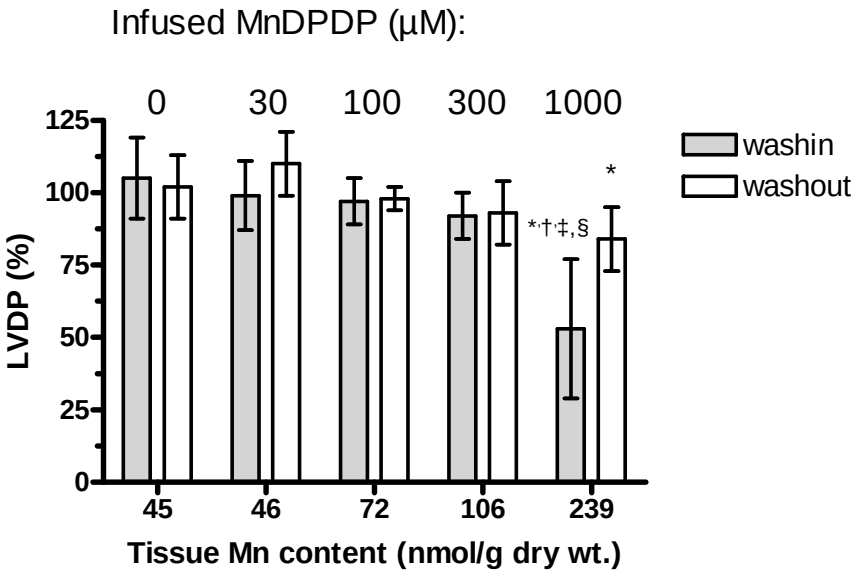

(b)

Figure 8.6: LVDP plotted against tissue Mn content in hearts from Paper I and II. The figure presents LVDP in the last minute of washin and washout of (a) $MnCl_2$ (median and range), and (b) MnDPDP (mean and SD). (a) $\star$ and † represent significant differences from control and 25 μM groups, respectively ($p < 0.05$). (b) $\star$, †, ‡ and § represent significant differences from control, 30, 100 and 300 μM groups, respectively ($p < 0.05$).

8.5.3 Mn^{2+} uptake from the perfusate

Papers I-III demonstrate that hearts take up and retain large amounts of Mn. This confirms earlier studies [17, 19], which also have shown, as demonstrated in Paper III, that accumulated Mn did not impair cellular energy metabolism. The present data also confirm findings showing that hearts receiving $MnCl_2$ accumulate about 8 times more Mn than hearts receiving MnDPDP [16].

At a coronary flow rate of 10 ml/min and an infusion time of 5 minutes, 50 ml perfusate was distributed during the infusion period in rat hearts (Paper I and II). Calculated amounts of Mn^{2+}-ions available for, and taken up into heart cells are presented in Table 8.8 and 8.9. The calculations are based on a mean heart weight of 1 g and a mean wet to dry ratio of 5. The small fractional uptake of Mn^{2+}-ions indicates that transmetallation of MnDPDP with Mn^{2+}-release in *ex vivo* rat hearts is limited, probably only 5-10 %.

Table 8.8: $MnCl_2$: Fractional uptake of Mn^{2+} from the perfusate (Paper I).

$MnCl_2$ (μmol/l)	Available Mn (μmol)	ΔMn content (nmol)	Mn^{2+} uptake (%)
25	1.25	44.6	3.6
100	5	102	2.0

Table 8.9: MnDPDP: Fractional uptake of Mn^{2+} from the perfusate (Paper II).

MnDPDP (μmol/l)	Available Mn (μmol)	ΔMn content (nmol)	Mn^{2+} uptake (%)
30	1.5	0.2	0.01
100	5	5.4	0.11
300	15	12.2	0.81
1000	50	38.8	0.77

Guinea pig hearts in Paper III, that received four repeated doses of $MnCl_2$ (*Manganese*) or $MnCl_2$ combined with Ca-gluconate (*Manganese-Calcium*) that easily dissociate (660 μM in total), accumulated large amounts of manganese. The fractional percentage uptake of Mn^{2+}-ions were 2.3 and 1.0 % for the *Manganese* and *Manganese-Calcium* group, respectively. These values are in the same order of magnitude as the $MnCl_2$ group in Paper I, but the uptake was reduced when calcium was present in the media due to ec competition for cell entry.

Altogether, the results of Paper I-III show that cellular Mn^{2+} uptake is small compared to available [Mn^{2+}]. However, the uptake is avid when competition with Ca^{2+}-ions is considered. Also the rapid once through passage of

perfusate containing Mn^{2+}-ions supports such an conclusion. The presented results originates from an artificial *ex vivo* model where plasma proteins are absent. Consequently, protein binding does not take place. In the *in vivo* situation, however, most ec Mn^{2+} are bound to macromolecules. Therefore, heart cells have access to an even smaller fraction of ec Mn^{2+}-ions.

In the *in vivo* situation, Mn^{2+} is gradually released from MnDPDP by transmetallation with Zn^{2+} in plasma (11-18 μM) [105]. This is a consequence of a lower stability constant for MnDPDP than for ZnDPDP, and thus ZnDPDP will be formed ($\sim$ 15 %) [86]. In *ex vivo* hearts, however, with no Zn^{2+}-ions present in the perfusate a transmetallation with divalent cations like Mg^{2+} ($<$ 5 %) and Ca^{2+} ($\sim$ 10 %) is possible [93]. These values coincide well with an assumed Mn^{2+} release of 5-10 % from MnDPDP in hearts.

8.5.4 Mn^{2+}-Ca^{2+} interactions with media containing low and high [Ca^{2+}]

In Paper I, interactions between Ca^{2+}- and Mn^{2+}-ions were studied by varying ec [Ca^{2+}] and ec [Mn^{2+}]. Figure 8.7 shows how this influenced Mn^{2+} accumulation and LVDP in cardiomyocytes. For 25 μM $MnCl_2$ the figure indicates a competition upon cell entry between Ca^{2+} and Mn^{2+} at different [$CaCl_2$]. Low [Ca^{2+}] led to further Mn^{2+} accumulation compared to normal [Ca^{2+}], whereas high [Ca^{2+}] reduced Mn^{2+} accumulation. When [$MnCl_2$] was increased to 100 μM, the same amount of Mn was retained with varying [Ca^{2+}]. This may be due to some kind of saturation effect, but this is not completely understood.

LVDP was not significantly depressed at 25 μM $MnCl_2$ with normal and high ec [Ca^{2+}] (18 and 9 %), but was, as expected, greatly depressed when ec [Ca^{2+}] was lowered (70 %). Hearts subjected to 100 μM $MnCl_2$ showed the same trend with a 52 % depression of LVDP for normal and high ec [Ca^{2+}] and 87 % for low [Ca^{2+}]. This shows that LVDP variations follow Mn uptake, and that low ec [Ca^{2+}] leads to cardiodepression.

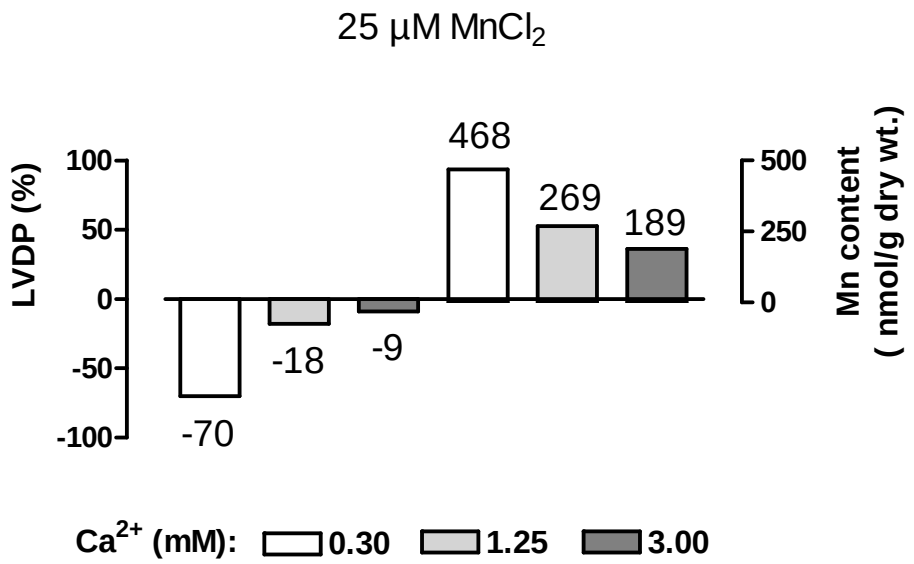

(a)

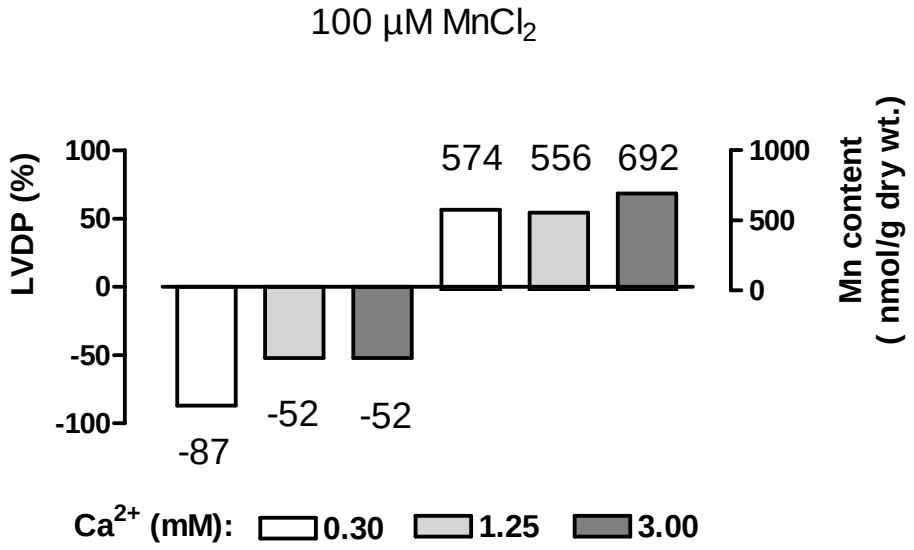

(b)

Figure 8.7: LVDP and tissue Mn content in hearts subjected to (a) 25 μM $MnCl_2$ and (b) 100 μM $MnCl_2$. Data are presented as median values (Paper I).

In Paper III $[Mn^{2+}] \geq 100$ μM significantly depressed LVDP in the *Manganese* ($MnCl_2$) group. In the *Manganese-Calcium* group Ca^{2+} was added to the perfusate (1 Mn^{2+}:10 Ca^{2+}), which led to positive inotropy for all four concen-

trations of the test substance and reduced Mn uptake (Figure 8.8). A likely mechanism is that elevation of ec Ca^{2+}, at least with the highest (100-500 μM) concentrations tested have raised the gradient of Ca^{2+} to Mn^{2+} too far at critical slow channel binding sites and thus reduced the effective Mn^{2+} influx.

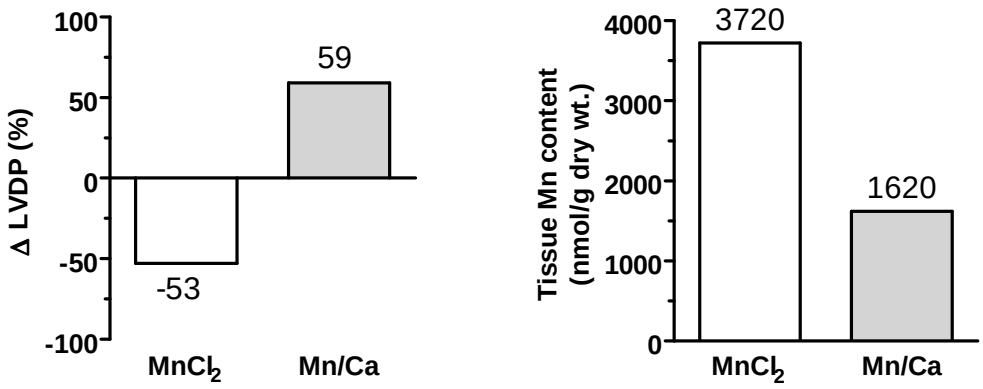

(a) (b)

Figure 8.8: (a) LVDP and (b) tissue Mn content in hearts subjected to *Manganese* (white colums) and *Manganese-Calcium* (gray colums) groups (Paper III).

8.6 Efficacy of Mn^{2+}-ions

Mn^{2+}-ions were found to be extremely efficient as proton relaxation enhancers in the intracellular compartment of rat cardiomyocytes. Since Mn^{2+}-ions are mainly concidered as T_1-agents transversal relaxation results are not discussed in this section.

8.6.1 Mn^{2+} and water interactions in compartementalized tissue

The relaxivity in a homogenous solution is easily determined (Equation 2.56 or Equation 3.2). In tissue the contrast agent distributes to different compartments with varying viscosities, and water exchange across membranes can be slow, intermediate or fast. The water can bring "magnetic memory" about the contrast effect to another compartment in the fast or intermediate exchange situation. In the 2SX model it is assumed that all water molecules within a particular compartment can interact with both *CA* that is bound to proteins or solvated with water. In addition, these processes have to be extremely fast.

The cardiomyocytes are highly structured with two major protein constituents: the myofibril (48 %) and the mitochondria (36 %) [55], of which the latter is the main pool for ic Mn^{2+}-ions [49]. Mitochondria are compartmentalized with a double cell membrane. They comprise more than 40 % of the protein content in the whole cardiomyocyte [110].

If Mn^{2+}-ions bind to proteins in the mitochondria it is very likely that this would lead to long correlation times (τ_c). An increased viscosity of water will also contribute to a reduced mobility and long τ_c. The longitudinal relaxation rate may also decrease if τ_c is large. In Figure 3.3 the relaxation rate constant of the bound water proton (R_{1M}) from the dipole-dipole term at different τ_c values are given. When τ_c is long, R_{1M} will decrease and thus might give a negative contribution to the contrast enhancement.

Lopez *et al.* [72] studied mitocondria from hepatocytes and Ward *et al.* [110] studied mitocondria from hearts. Both found that the "mitochondrial" water exchange is extremely fast, which means that the exchanging water will bring magnetic memory into the cytosol. In the present studies only one component R_{1ic} was found significant in the ic space, which may be due to this assumed fast mitochondrial exchange, but this has to be investigated further.

8.6.2 Relaxivity of Mn^{2+}-ions in cardiac tissue

The Mn content was measured by AAS and ICP, where number of moles was measured per gram dry tissue. Intracellular relaxation rate constants (R_{1ic}) were proportional to Mn content and the relaxivities were determined in the 2SX model. The relaxivity given in (s nmol/g dry wt.)$^{-1}$ was converted into (s mM)$^{-1}$ in the following manner:

(s nmol/g dry wt.)$^{-1}$ = (g dry wt./ s nmol)

(5 g wet wt./s nmol), where 1 g dry wt. $\sim$ 5 g wet wt. in cardiac tissue.

(5 ml/s nmol), where 1 g wet wt. $\sim$ 1 ml tissue.

(5 l/s μmol) = (5/s μM) = (5000/s mM)

In Paper I and II the relaxivities of Mn^{2+}-ions in ic water (r_{1ic}) were as high as 60 (s mM)$^{-1}$ for $MnCl_2$ and 56 (s mM)$^{-1}$ for MnDPDP, which is about 8-9 times and 35-38 times higher than with $MnCl_2$ and MnDPDP in solution, respectively (Table 8.10). The drastic increase in relaxivity is based on the action of free Mn^{2+}-ions in tissue, where most of the accumulated Mn^{2+}-ions are bound to proteins increasing the correlation time with water (Figure 3.4).

As earlier described, *in vitro*, $MnCl_2$ is a pure inner-sphere agent and the stable MnDPDP complex is a pure outer-sphere agent. In tissue, Mn^{2+}-ions that are slowly released from MnDPDP act in the same way as Mn^{2+}-ions quickly released from $MnCl_2$. The free Mn^{2+}-ions enter the contractile my-

Table 8.10: Mn based contrast media with the number of inner-sphere coordinated water molecules (q), *in vitro* and *ex vivo* relaxivities at 0.47 T and 37°C are given.

Mn contrast media	q	*in vitro* r_{1ic} $(\text{s mM})^{-1}$	*ex vivo* r_{1ic} $(\text{s mM})^{-1}$
$MnCl_2$ (Paper I)	6	6.9	60
MnDPDP (Paper II)	0	1.6	56

ocytes, where they distribute and bind to small molecules and large macromolecules. In Figure 8.9 the ic relaxation rates measured in hearts subjected to 0-100 μM $MnCl_2$ and 0-1000 μM MnDPDP are plotted against their calculated Mn^{2+} uptake in μM. The concentration-response graphs are linear for both groups at these low-intermediate Mn concentrations, and MnDPDP was about 8 times less effective than $MnCl_2$. Since the rotational correlation time (τ_R) becomes the dominant relaxation enhancement effect [22], this may explain why almost equal ic relaxivities for $MnCl_2$ and MnDPDP are found .

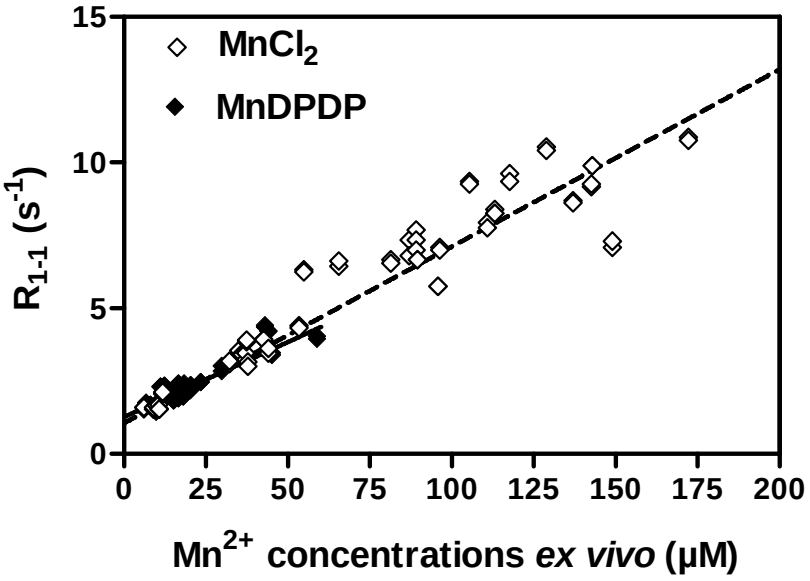

Figure 8.9: Concentration-response graph for Mn^{2+}-ions. R_{1-1} values from $MnCl_2$ and MnDPDP hearts are plotted together to compare their ic efficacy in tissue. The Mn concentrations are converted from nmol/g dry wt. to μmol/l. Each diamond represent one heart. The intrinsic values are depicted as dashed ($MnCl_2$) and fully drawn (MnDPDP) lines.

In a paper by Southon *et al.* [100] the same trend was found in excised liver from rats subjected to $MnCl_2$ or MnDPDP. Based on monoexponential R_1 values the relaxivities (r_1) at 0.47 T and 37°C for both Mn-compounds 2 hours after injection were calculated. The relaxivity was 0.050 $(\text{s nmol/g wet tissue})^{-1}$

for both substances or, by using the approximation that 1 g wet tissue $\sim$ 1 ml, 50 (s mM)$^{-1}$. In addition, they calculated a high r_1 value of 0.036 (s nmol/g wet tissue)$^{-1}$ or 36 (s mM)$^{-1}$ for pig hearts. This value is closer to the calculated r_1 of 21 (s mM)$^{-1}$ for $MnCl_2$ and 33 (s mM)$^{-1}$ for MnDPDP based on the monoexponential T_1 values in Paper I and II, respectively.

Therefore, the increased τ_R between proton and electron (Mn^{2+}) spins, and maintained inner-sphere water access ($q > 0$), make intracellular Mn^{2+}-ions and Mn^{2+}-ion-releasing contrast media surprisingly effective as T_1-agents.

8.6.3 Mn^{2+}-Ca^{2+} interactions and efficacy

The efficacy results from Paper I presented in Table 8.11 are in close concordance with the physiology results discussed in Section 8.5.4. For 25 μM $MnCl_2$ the delta relaxation rate constants (ΔR_{1ic} = R_{1ic} (Mn^{2+}) - R_{1ic} (control)) increased with 71 % when Ca^{2+} was lowered, and decreased with 41 % when Ca^{2+} was raised from its normal value in the perfusate. This corresponds well with the results in Figure 8.7 a, where the Mn content increased with 74 % and decreased with 30 % in the low and high ec Ca^{2+} situation, respectively.

The ΔR_{1ic} between the groups with 100 μM $MnCl_2$ and different ec Ca^{2+} were insignificant (Table 8.11), which corresponded well with the accumulated amount of Mn (Figure 8.7 b). Addition of nifidipine reduced the efficacy drastically (70 %) in agreement with less Mn accumulation in these hearts, i.e. 70 % less than the reference group (Table 1 in Paper I). These results reflected the proportionality between the uptake of Mn^{2+}-ions and intracellular proton relaxation enhancement. The conclusion is that variations in ec Ca^{2+} can affect the efficacy drastically when Mn^{2+} uptake is hindered.

Table 8.11: Results from Paper I: ΔR_{1ic} values for situations with lowered, normal or raised Ca^{2+} or with nifidipine together with 25 or 100 μM $MnCl_2$ in the perfusate.

	25 μM $MnCl_2$	**100 μM $MnCl_2$**
Ca^{2+} (mM)	ΔR_{1ic} (s^{-1})	ΔR_{1ic} (s^{-1})
0.30 (low)	5.30 (+71 %)	6.49
1.25 (normal)	3.10	6.29
3.00 (high)	1.84 (-41 %)	7.21
Nifidipine	-	1.88 (-70 %)

In Paper III the experimental setup was different from those in Paper I and II. Guinea pig hearts were loaded with high concentrations of Mn^{2+}. The study was designed in order to find out whether addition of Ca^{2+}-ions to the contrast media could have positive cardioprotective effects. The efficacy of

pure Mn^{2+}-ions and of Mn^{2+} together with Ca^{2+} at recommended ratios were compared. Since the four concentrations (10, 50, 100, 500 μM) were infused in each heart (660 μM), only the accumulated Mn content in total and the respective relaxation values could be estimated.

The R_{1ic} values before (R_{1pre}) and after (R_{1post}) infusion of the contrast media are compared in Table 8.12, where ΔR_{1ic} is as high as 19.6 s^{-1} for the *Manganese* group and 10.4 s^{-1} for the *Manganese-Calcium* group. These results prove that an addition of Ca^{2+}-ions to the contrast media in the ratio 1 Mn^{2+}:10 Ca^{2+} makes the contrast enhancement less effective than with normal [Ca^{2+}]. Parallel results were found in a Paper of Flacke *et al.* [37] with infarct imaging at 1.5 T, where the efficacy decreased when Ca^{2+} was added to the contrast media in a 1 Mn^{2+}:8 Ca^{2+} ratio (Table 8.12).

MP-680 (Mallinckrodt), which is a slow releaser of Mn^{2+}-ions such as MnDPDP, was used in the same study. From the high dose of MP-680 being used and the smaller ΔR_1 value achieved than for a smaller dose of $MnCl_2$, it was demonstrated that it is less effective in rat imaging analogous with MnDPDP contra $MnCl_2$ in relaxography experiments.

Table 8.12: Maximal longitudinal relaxation enhancement in viable rat myocardium: $\Delta R_1 = R_{1post} - R_{1pre}$.

Test substance	**Dose**	ΔR_1 (s^{-1})
$MnCl_2$	15 μmol/kg	$1.33 \pm 0.03^{\star}$
1 $MnCl_2$:8 Ca	15 μmol/kg	$0.46 \pm 0.05^{\star}$
MP-680	45 μmol/kg	$1.00 \pm 0.07^{\star}$
$MnCl_2$	660 μM	$19.6 \pm 3.4^{\dagger}$
1 $MnCl_2$:10 Ca	660 μM	$10.4 \pm 1.3^{\dagger}$

*Flacke *et al.*: Infarct imaging (1.5 T) of rat myocardium. Peak 65 minutes after injection.
†Paper III: Ic relaxation rate constant from relaxography (0.47 T) of guinea pig myocardium.

Even though the main purpose of Paper III was not to study water exchange in guinea pig hearts, the ic relaxivity was calculated on the basis of the collected data. However, the calculated r_{1ic} of 31 (s mM)$^{-1}$ is very uncertain due to various factors. Since *Manganese* and *Manganese-Calcium* both are salts that easily dissociate, the R_{1-1} values from these two groups together with the control group were used in the 2SX model to calculate this r_{1ic}. High doses of the contrast media elevated the Mn content (Figure 8.8) and increased the relaxation rate constants (Table 8.12) in guinea pig hearts drastically, but r_{1ic} was half as large as in rat hearts. This may be due to the fact that T_1 data of low and intermediate Mn concentrations were lacking in the present study and that saturation effects had occured at the high concentrations used.

The various factors to be considered are: Only high concentrations of Mn^{2+}-ions are used; few points (three) are used to evaluate the linearity; the Mn control values are most probably below the detection limit (<40 nmol/g dry wt.) of the method being used to measure Mn content; and, a saturation both in the Mn uptake and for R_{1-1} may have occured. R_{1-1} had increased by as much as 85-92 % and was possibly saturated. Since the hearts were loaded with Mn^{2+}-ions, this could have led to saturation of Mn-protein binding sites in cytosol or most probably in the mitochondria and long correlation times with water, which may explain the assumed saturation effect that led to the smaller ic efficacy.

8.6.4 Mn^{2+}-ions as ic T_1-agent

Mn^{2+}-ions have a high affinity to slow Ca^{2+} channels and probably also to other transport mechanisms in the cardiac cell membrane in rat and guinea pig hearts. This uptake is crucial for the efficacy of all the presented Mn-compounds. The contrast media MnDPDP is an effective hepatobilary agent due to uptake in normal hepatocytes and no or little uptake in metastatic liver tumors [35]. Most of the MnDPDP is distributed to the liver (9.7 %) and only a minor fraction is distributed to the myocardium (0.1 %) via the supplying coronary arteries [50]. Nevertheless, since the cardiomyocytes are excitable cells provided with many slow Ca^{2+} channels large available Mn^{2+}-ions enter easily. Their Mn^{2+} retention capacity is also particularly good as they are crowded with mitochondria, where the metal ions are retained for hours.

The toxicity of free Mn^{2+}-ions is reduced upon chelation of the Mn^{2+}-ions to MnDPDP. However, since the stable complex has no inner-sphere relaxation properties and low relaxivity it would have been a poor relaxation agent if it had remained 100 % stable in tissue. However, *ex vivo* and *in vivo*, agents like MnDPDP are slow releasers of Mn^{2+}-ions, where the dominant relaxation mechanism is the same as for $MnCl_2$ and Mn^{2+}/Ca^{2+}-compounds, i.e. increased τ_R due to ic protein binding. While the dissociation of MnDPDP is limited, $MnCl_2$ and Mn^{2+}/Ca^{2+} dissociate completely. Since the mechanisms leading to powerful ic relaxation enhancement principally are the same for all the three Mn-componds, accumulation of Mn^{2+}-ions seems to be the main limiting efficacy factor. From the findings in Paper I and II it can be derived that a 10 times higher dose of MnDPDP compared to $MnCl_2$ is both 10 times less cardiotoxic and 8 times less effective as an ic contrast agent, i.e. in the same order of magnitude. Since low concentrations of $MnCl_2$ have been proven sufficient to increase relaxivity without inducing cardiodepression in *ex vivo* rat hearts, more *in vivo* studies with this agent alone is thereby suggested. If higher concentrations are required *in vivo*, cardiodepression can possibly be avoided by a controlled and slow infusion of $MnCl_2$. The *in vivo* conditions are discussed further in Paper III.

In imaging, it is reasonable to use a slow releaser of Mn^{2+}-ions (MnDPDP and MP-680) because of the delayed maximal enhancement effect (30 minutes) [37]. It is also important to have constant contrast between viable and infarcted myocardium to allow keeping imaging parameters constant over a longer period of time. In contrast to non-specific ec Gd-agents, Mn-agents are both tissue specific and display a long "imaging window" [37]. Animal studies [14, 37, 62, 111] have shown that Mn-compounds are promising as viability agents in the heart due to an increased contrast in viable versus diseased tissue. Figure 8.10 shows an example from a recent human heart study on healthy volunteers carried out at the MR centre in Trondheim [96]. The images are T_1-weighted and the myocardium is signal intense ("positive" contrast) in the Mn-enhanced image.

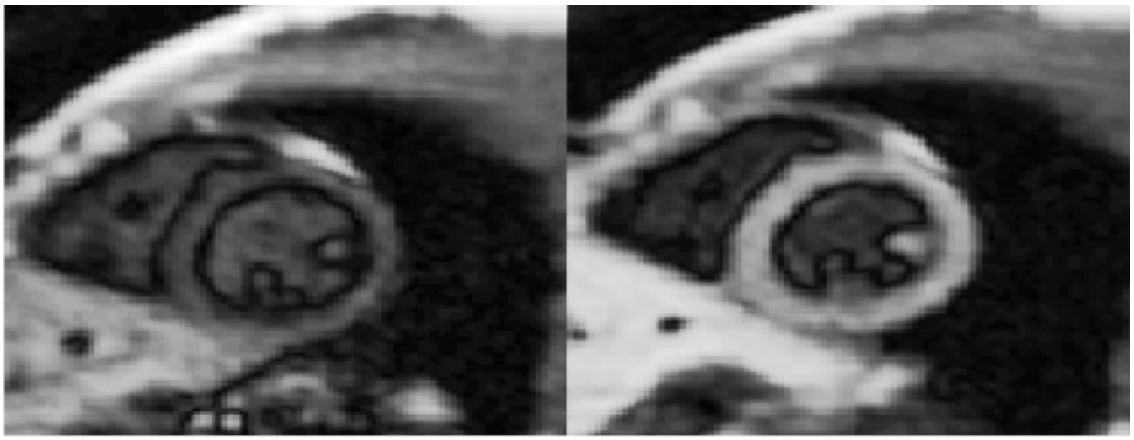

Figure 8.10: Human myocardial short-axis images at a 1.5 T Siemens Symphony scanner. Measured with a IR-turbo-FLASH sequence with TI = 0.9 s before and 30 minutes after slow intravenous infusion (30 min) of 5 μmol/kg body wt. MnDPDP [96].

Mn-compounds are good candidates to Gd-chelates as with the Mn blood pool agents discussed in the Paper of Aime *et al.* (Section 3.4.4) [1]. Mn-compounds that are linked to large macromolecules with maintained inner-sphere access are promising as blood pool agents for MR angiography.

REFERENCES

1. Aime S, Anelli L, Botta M, Brocchetta M, Canton S, Fedeli F *et al.*. Relaxometric evaluation of novel manganese(II) complexes for application as contrast agents in magnetic resonance imaging. *J Biol Inorg Chem* 2002; 7(1-2), 58-67.

2. Aisen P, Enns C, Wessling-Resnick M. Chemistry and biology of eukaryotic iron metabolism. *Int J Biochem Cell Biol* 2001; 33(10), 940-59.

3. Asplund A, Grant D, Karlsson JOG. Mangafodipir (MnDPDP)- and $MnCl_2$-induced endothelium-dependent relaxation in bovine mesenteric arteries. *J Pharmacol Exp Ther* 1994; 271(2), 609-18.

4. Bache RJ *et al.*. In: Hearse DJ, Yellon DM, editors. Therapeutic approaches to myocardial infarct size limitation. New York: Raven Press; 1984.

5. Bain AD. The choise of parameters in an NMR experiment. Application to the inversion-recovery T_1 method. *Journal of Magnetic Resonance* 1990; 89, 153-60.

6. Bauer WR, Hiller KH, Roder F, Rommel E, Ertl G, Haase A. Magnetization exchange in capillaries by microcirculation affects diffusion-controlled spin-relaxation: a model which describes the effect of perfusion on relaxation enhancement by intravascular contrast agents. *Magn Reson Med* 1996; 35(1), 43-55.

7. Belton PS, Ratcliffe RG. NMR and compartmentation in biological tissue. *Progress in NMR spectroscopy* 1985; 17, 241-79.

8. Bergmann SR *et al.*. In: Iskandrian AS, van der Wall EE, editors. Myocardial viability. Detection and clinical relevance. Dordrecht, The Netherlands: Kluwer Academic Publishers; 1994; 154.

9. Bers DM. Excitation-Contraction coupling and cardiac contractile force. Dordrecht, The Netherlands: Kluwer Academic Publisher; 1991, 119-48.

10. Bjørnerud A, Bjerner T, Johansson LO, Ahlström HK. Assessment of myocardial blood volume and water exchange: theoretical considerations and in vivo results. *Magn Reson Med* 2003; 49(5), 828-37.

11. Bloch F. Nuclear induction. *Physical Review* 1946; 70(7-8), 460-74.

12. Bloembergen N. Proton relaxation times in paramagnetic solutions. *J Chem Phys* 1957; 27(2), 572-3.

13. Bloembergen N, Morgan LO. Proton relaxation times in paramagnetic solutions effects of electron spin relaxation. *J Chem Phys* 1961; 34(3), 842-50.

14. Bremerich J, Saeed M, Arheden H, Higgins CB, Wendland MF. Normal and infarcted myocardium: differentiation with cellular uptake of manganese at MR imaging in a rat model. *Radiology* 2000; 216(2), 524-30.

15. Brurok H. Manganese and the Heart. A Magic Metal with Diagnostic and Therapeutic Possibilities. PhD Thesis. Trondheim: NTNU 1999.

16. Brurok H, Berg K, Sneen L, Grant D, Karlsson JOG, Jynge P. Cardiac metal contents after infusions of manganese. An experimental evaluation in the isolated rat heart. *Invest Radiol* 1999; 34(7), 470-6.

17. Brurok H, Schjøtt J, Berg K, Karlsson JO, Jynge P. Effects of manganese dipyridoxyl diphosphate, dipyridoxyl diphosphate^{2-}, and manganese chloride on cardiac function. An experimental study in the Langendorff perfused rat heart. *Invest Radiol* 1995; 30(3), 159-67.

18. Brurok H, Schjøtt J, Berg K, Karlsson JOG, Jynge P. Manganese and the heart: acute cardiodepression and myocardial accumulation of manganese. *Acta Physiologica Scandinavia* 1997; 159(1), 33-40.

19. Brurok H, Schjøtt J, Berg K, Karlsson JOG, Jynge P. Effects of MnDPDP, DPDP^{2-}, and $MnCl_2$ on cardiac energy metabolism and manganese accumulation. An experimental study in the isolated perfused rat heart. *Invest Radiol* 1997; 32(4), 205-11.

20. Brurok H, Skoglund T, Berg K, Skarra S, Karlsson JOG, Jynge P. Myocardial manganese elevation and proton relaxivity enhancement with manganese dipyridoxyl diphosphate. Ex vivo assessments in normally perfused and ischemic guinea pig hearts. *NMR Biomed* 1999; 12(6), 364-72.

21. Caravan P, Cloutier NJ, Greenfield MT, McDermid SA, Dunham SU, Bulte JW *et al.*. The interaction of MS-325 with human serum albumin and its effect on proton relaxation rates. *J Am Chem Soc* 2002; 124(12), 3152-62.

22. Caravan P, Ellison JJ, McMurry TJ, Lauffer RB. Gadolinium(III) Chelates as MRI Contrast Agents: Structure, Dynamics, and Applications. *Chem Rev* 1999; 99(9), 2293-352.

23. Carr HY, Purcell EM. Effects of diffusion on free precession in nuclear magnetic resonance experiments. *Physical Review* 1954; 3, 630-8.

24. Cieslar J, Huang MT, Dobson GP. Tissue spaces in rat heart, liver, and skeletal muscle in vivo. *Am J Physiol* 1998; 275, R1530-6.

25. Clarke K, Anderson RE, Nedelec JF, Foster DO, Ally A. Intracellular and extracellular spaces and the direct quantification of molar intracellular

concentrations of phosphorus metabolites in the isolated rat heart using ^{31}P NMR spectroscopy and phosphonate markers. *Magn Reson Med* 1994; 32(2), 181-8.

26. Cotton FA, Wilkinson G. Advanced inorganic chemistry. 4 ed. New York: Wiley; 1994.

27. Delahayes JF. Depolarization-induced movement of Mn^{2+} cations across the cell membrane in the guinea pig myocardium: its effect on the mechanical response. *Circ Res* 1975; 36(6), 713-8.

28. Dobson GP, Cieslar JH. Intracellular, interstitial and plasma spaces in the rat myocardium in vivo. *J Mol Cell Cardiol* 1997; 29(12), 3357-63.

29. Donahue KM. Studies of Gd-DTPA relaxivity and proton exchange rates in tissue with implications for MR imaging of regional myocardial perfusion. PhD Thesis. Massachusetts: MIT 1993.

30. Donahue KM, Burstein D, Manning WJ, Gray ML. Studies of Gd-DTPA relaxivity and proton exchange rates in tissue. *Magn Reson Med* 1994; 32(1), 66-76.

31. Donahue KM, Weisskoff RM, Burstein D. Water diffusion and exchange as they influence contrast enhancement. *J Magn Reson Imaging* 1997; 7(1), 102-10.

32. Donahue KM, Weisskoff RM, Parmelee DJ, Callahan RJ, Wilkinson RA, Mandeville JB *et al.*. Dynamic Gd-DTPA enhanced MRI measurement of tissue cell volume fraction. *Magn Reson Med* 1995; 34(3), 423-32.

33. Dudek H, Pytkowski B. Effects of in vivo manganese administration on calcium exchange and contractile force of rat ventricular myocardium. *Basic Res Cardiol* 1991; 86(6), 515-22.

34. Earls JP, Ho VB, Foo TK, Castillo E, Flamm SD. Cardiac MRI: recent progress and continued challenges. *J Magn Reson Imaging* 2002; 16(2), 111-27.

35. Elizondo G, Fretz CJ, Stark DD, Rocklage SM, Quay SC, Worah D *et al.*. Preclinical evaluation of MnDPDP: new paramagnetic hepatobiliary contrast agent for MR imaging. *Radiology* 1991; 178(1), 73-8.

36. Farrar TC. NMR pulse experiments. Introduction to Pulse Nmr Spectroscopy. Chicago, Madison: Farragut Press 1987, 35-54.

37. Flacke S, Allen JS, Chia JM, Wible JH, Periasamy MP, Adams MD *et al.*. Characterization of viable and nonviable myocardium at MR imaging: comparison of gadolinium-based extracellular and blood pool contrast materials versus manganese-based contrast materials in a rat myocardial infarction model. *Radiology* 2003; 226(3), 731-8.

38. Gavin CE. Mn^{2+} sequestration by mitochondria and inhibition of oxidative phosphorylation. *Toxicol Appl Pharmacol* 1992; 115(1), 1-5.

39. Grant D, Zech K, Holtz E. Biodistribution and in vivo stability of manganese dipyridoxyl diphosphate in relation to imaging efficacy. *Invest Radiol* 1994; 29 Suppl 2, S249-50.

40. Gunshin H, Mackenzie B, Berger UV, Gunshin Y, Romero MF, Boron WF *et al.*. Cloning and characterization of a mammalian proton-coupled metal-ion transporter. *Nature* 1997; 388, 482-8.

41. Haacke EM, Brown RW, Thompson MR, Venkatesan R. Magnetic Resonance Imaging. Physical Principles and Sequence Design. New York: John Wiley & Sons 1999.

42. Hahn EL. Spin echoes. *Physical Review* 1950; 80(4), 580-94.

43. Hashemi RH, Bradley Jr WG. MRI The Basics. Baltimore: Williams and Wilkins 1997.

44. Hazlewood CF, Chang DC, Nichols BL, Woessner DE. Nuclear magnetic resonance transverse relaxation times of water protons in skeletal muscle. *Biophys J* 1974; 14(8), 583-606.

45. Higgins C, de Roos A. Cardiovascular MRI and MRA. Philadelphia, PA: Lippincott Williams & Wilkins; 2003.

46. Hills BP, Belton PS. NMR studies of membrane transport. *Annu Rep NMR Spectros* 1989; 21, 99-159.

47. Holm RH, Kennephol P, Solomon EI. Structural and functional aspects of metal sites in biology. *Chem Rev* 1996; 96, 2239-314.

48. Hu TC, Pautler RG, MacGowan GA, Koretsky AP. Manganese-enhanced MRI of mouse heart during changes in inotropy. *Magn Reson Med* 2001; 46(5), 884-90.

49. Hunter DR, Haworth RA, Berkoff HA. Cellular manganese uptake by the isolated perfused rat heart: a probe for the sarcolemma calcium channel. *J Mol Cell Cardiol* 1981; 13(9), 823-32.

50. Hustvedt SO, Grant D, Southon TE, Zech K. Plasma pharmacokinetics, tissue distribution and excretion of MnDPDP in the rat and dog after intravenous administration. *Acta Radiol* 1997; 38, 690-9.

51. Judd RM, Atalay MK, Rottman GA, Zerhouni EA. Effects of myocardial water exchange on T_1 enhancement during bolus administration of MR contrast agents. *Magn Reson Med* 1995; 33(2), 215-23.

52. Judd RM, Reeder SB, May-Newman K. Effects of water exchange on the measurement of myocardial perfusion using paramagnetic contrast agents. *Magn Reson Med* 1999; 41(2), 334-42.

53. Jynge P, Brurok H, Asplund A, Towart R, Refsum H, Karlsson JOG. Cardiovascular safety of MnDPDP and $MnCl_2$. *Acta Radiol* 1997; 38, 740-9.

54. Kang YS, Gore JC. Studies of tissue NMR relaxation enhancement by manganese. Dose and time dependences. *Invest Radiol* 1984; 19(5), 399-407.

55. Katz AM. Structure of the heart. In: Weinberg RW, LaPlante M, Lerman E, editors. Physiology of the heart. Philadelphia MO: Lippincott Williams and Wilkins; 2001.

56. Keen CL, Lønnerdal B, Hurley LS. Manganese. In: Friden E, editor. Biochemistry of the Essential Ultra Trace Elements. New York: Plenum Press; 1984, 89-132.

57. Kim RJ, Fieno DS, Parrish TB, Harris K, Chen EL, Simonetti O *et al.*. Relationship of MRI delayed contrast enhancement to irreversible injury, infarct age, and contractile function. *Circulation* 1999; 100(19), 1992-2002.

58. König SH, Baglin C, Brown 3rd RD, Brewer CF. Magnetic field dependence of solvent proton relaxation induced by $Gd^{3+}$and Mn^{2+}complexes. *Magn Reson Med* 1984; 1(4), 496-501.

59. König SH, Brown 3rd RD. Relaxation of solvent protons by paramagnetic ions and its dependence on magnetic field and chemical environment: implications for NMR imaging. *Magn Reson Med* 1984; 1(4), 478-95.

60. König SH, Spiller M, Brown 3rd RD, Wolf GL. Investigation of the biochemical state of paramagnetic ions in vivo using the magnetic field dependence of $1/T_1$ of tissue protons (NMRD profile): applications to contrast agents for magnetic resonance imaging. *Int J Rad Appl Instrum B* 1988; 15(1), 23-9.

61. Krebs HA, Henseleit K. Untersuchungen über die Harnstoffbildung im Tierkörper. *Hoppe Seylers Z Physiol Chem* 1932; 210, 33-66.

62. Krombach GA, Saeed M, Higgins CB, Novikov V, Wendland MF. Contrast-enhanced MR delineation of stunned myocardium with administration of $MnCl_2$ in rats. *Radiology* 2004; 230(1), 183-90.

63. Kruk D, Kowalewski J. Field-dependent proton relaxation in aqueous solutions of some manganese(II) complexes: a new interpretation. *J Biol Inorg Chem* 2003; 8(5), 512-8.

64. Labadie C, Lee JH, Vetek G, Springer Jr CS. Relaxographic Imaging. *J Magn Reson*1994; 105(2), 99-112.

65. Landis CS, Li X, Telang FW, Coderre JA, Micca PL, Rooney WD *et al.*. Determination of the MRI contrast agent concentration time course in vivo following bolus injection: Effect of equilibrium transcytolemmal water exchange. *Magn Reson Med* 2000; 44(4), 563-74.

66. Landis CS, Li X, Telang FW, Molina PE, Palyka I, Vetek G *et al.*. Equilibrium Transcytolemmal Water-Exchange Kinetics in Skeletal Muscle In Vivo. *Magn Reson Med* 1999; 42, 467-78.

67. Langendorff O. Untersuchungen am Überlebenden Säugtierherzen. *Pflügers Arch Physiol* 1895; 61, 291-332.

68. Lauffer RB. Paramagnetic metal complexes as water proton relaxation agents for NMR imaging: theory and design. *Chemical Review* 1987; 87, 901-27.

69. Lauterbur PC, Mendonca Dias MH, Rudin AM. Augmentation of water proton spin-lattice relaxation rates by the *in vitro* addition of paramagnetic ions. In: Duton P, editor. Frontiers of Biological Energetics. New York: Academic Press; 1978, 752-9.

70. Leigh JS. Relaxation times in systems with chemical exchange: some exact solutions. *Journal of Magnetic Resonance* 1971; 4(3), 308-11.

71. Lin YJ. Manganese ion enhances T_1-weighted MRI during brain activation: an approach to direct imaging of brain function. *Magn Reson Med* 1997; 38(3), 378-88.

72. López-Beltrán EA, Maté MJ, Cerdán S. Dynamics and environment of mitochondrial water as detected by ^{1}H NMR. *J Biol Chem* 1996; 271(18), 10648-53.

73. Luterotti A, Zanic-Grubisic T, Juretic DA. A rapid and simple method for the detection of copper, manganese, and zinc in rat liver by direct flame atomic absorption spectrometry. *Analyst* 1992; 117, 141-3.

74. Martin ML, Martin GJ, Delpuech J-J. Systematic errors resulting from off-resonance effects and maladjustments of the pulse angles. Practical NMR Spectroscopy. London: Heyden & Son; 1980, 267-72.

75. Mauss Y, Grucker D, Fornasiero D, Chambron J. NMR compartmentalization of free water in the perfused rat heart. *Magn Reson Med* 1985; 2(3), 187-94.

76. McConnell HM. Reaction Rates by Nuclear Magnetic Resonance. *The Journal of Chemical Physics* 1958; 28(3), 430-1.

77. McLauglin AC, Leigh Jr JS. Relaxation times in systems with chemical exchange: approximate solutions for the nondilute case. *J Magn Reson Imaging* 1973; 9, 296-304.

78. Meiboom S, Gill D. Modified spin-echo method for measuring nuclear relaxation times. *Rev Sci Instrum* 1958; 29(8), 688-91.

79. Mizzelwitz B, Mühler A, Weinmann HJ. A toxicological risk for using manganese complexes. A literature survey of existing data through several medical specialities. *Invest Radiol* 1995; 30, 611-20.

80. Murry CE, Jennings RB, Reimer KA. Preconditioning with ischemia: a delay of lethal cell injury in ischemic myocardium. *Circulation* 1986; 74(5), 1124-36.

81. Nordhøy W, Anthonsen WH, Bruvold M, Brurok H, Skarra S, Krane J *et al.*. Intracellular manganese ions provide strong T_1 relaxation in rat myocardium. *Magn Reson Med* 2004.

82. Nordhøy W, Anthonsen WH, Bruvold M, Jynge P, Krane J, Brurok H. Manganese ions as intracellular contrast agents: proton relaxation and calcium interactions in rat myocardium. *NMR Biomed* 2003; 16(2), 82-95.

83. Piper HM, Volz A, Schwarz P. Adult ventricular rat heart muscle cells. In: Piper HM, editor. Cell culture techniques in heart and vessel research. Berlin Heidelberg: Springer-Verlag; 1990, 36-60.

84. Press WH, Flannery BP, Teukolsky SA, Vetterling WT. Numerical Recipes in C: The art of Scientific Computing. Cambridge: Cambridge University Press; 1993.

85. Rahimtoola SH. The hibernating myocardium. *Am Heart J* 1989; 117, 211-21.

86. Rocklage SM, Cacheris WP, Quay SC, Hahn FE, Raymond KN. Manganese (II) N,N'-Dipyridoxylethylenediamine-N,N'-diacetate 5,5'-Bis(phosphate). Synthesis and Characterization of a Paramagnetic Chelate for Magnetic Resonance Imaging Enhancement. *Inorg Chem* 1989; 28, 477-85.

87. Rocklage SM, Watson A, Carvlin MJ. Contrast agents in magnetic resonance imaging. In: Stark DD, Bradley WG, editors. Magnetic resonance imaging. St Louis MO: Mosby Year Book; 1994, 372-437.

88. Rose CP, Goresky CA. Constraints on the uptake of labeled palmitate by the heart. The barriers at the capillary and sarcolemmal surfaces and the control of intracellular sequestration. *Circ Res* 1977; 41(4), 534-45.

89. Saeed M, Wendland MF, Takehara Y, Higgins CB. Reversible and irreversible injury in the reperfused myocardium: differentiation with contrast material-enhanced MR imaging. *Radiology* 1990; 175(3), 633-7.

90. Satoh H, Delbridge LM, Blatter LA, Bers DM. Surface:volume relationship in cardiac myocytes studied with confocal microscopy and membrane capacitance measurements: species-dependence and developmental effects. *Biophys J* 1996; 70(3), 1494-504.

91. Schaefer S, Lange RA, Gutekunst DP, Parkey RW, Willerson JT, Peshock RM. Contrast-enhanced magnetic resonance imaging of hypoperfused myocardium. *Invest Radiol* 1991; 26(6), 551-6.

92. Schaefer S, Schwartz GG, Gober JR, Massie B, Weiner MW. Magnetic resonance spectroscopy. Evaluation of ischemic heart disease. *Invest Radiol* 1989; 24(12), 969-72.

93. Schmidt PP, Toft KG, Skotland T, Andersson K. Stability and transmetallation of the magnetic resonance contrast agent MnDPDP measured by EPR. *J Biol Inorg Chem* 2002; 7(3), 241-8.

94. Seland JG, Sørland GH, Anthonsen HW, Krane J. Combining PFG and CPMG NMR Measurements for Separate Characterization of Oil and Water Simultaneously Present in a Heterogeneous System. *Applied Magnetic resonance* 2003; 24, 41-53.

95. Shaw D. Summary of the clinical experience with S-095 injection (Manganese Dipyridoxyl Diphosphate, MnDPDP). In: Rinck P, Muller R, editors. New Developments in Contrast Agent Research. Proceedings of the 3rd Special Topic Seminar of the European Magnetic Resonance Forum; 1993, 15-26.

96. Skjold A, Vangberg TR, Kristoffersen A, Haraldseth O, Jynge P, Larsson HBW. Relaxation enhancing properties of MnDPDP in human myocardium. *J Magn Reson Imaging*, In Press.

97. Sobol WT, Jackels SC, Cothran RL, Hinson WH. NMR spin-lattice relaxation in tissues with high concentration of paramagnetic contrast media: evaluation of water exchange rates in intact rat muscle. *Med Phys* 1991; 18(2), 243-50.

98. Solomon I. Relaxation processes in a system of 2 spins. *Physical review* 1955; 99(2), 559-65.

99. Sørland GH, Anthonsen HW, Seland JG, Anthonsen F, Widerøe HC. Exploring the separate NMR responses from crude oil and water simultaneously present in a rock core. *Applied Magnetic Resonance* 2004; 26, 1-9.

100. Southon TE, Grant D, Bjørnerud A, Moen OM, Spilling B, Martinsen I *et al.*. NMR relaxation studies with MnDPDP. *Acta Radiol* 1997; 38, 708-16.

101. Spiller M, Brown 3rd RD, Koenig SH, Wolf GL. Longitudinal proton relaxation rates in rabbit tissues after intravenous injection of free and chelated Mn^{2+}. *Magn Reson Med* 1988; 8(3), 293-313.

102. Stanisz GJ. Water dynamics in human blood via combined measurements of T_2 relaxation and diffusion in the presence of gadolinium. *Magn Reson Med* 1998; 39(2), 223-33.

103. Storey P, Danias PG, Post M, Li W, Seoane PR, Harnish PP *et al.*. Preliminary evaluation of EVP 1001-1: a new cardiac-specific magnetic resonance contrast agent with kinetics suitable for steady-state imaging of the ischemic heart. *Invest Radiol* 2003; 38(10), 642-52.

104. Tirkkonen B, Aukrust A, Couture E, Grace D, Haile Y, Holm KM *et al.*. Physicochemical characterisation of mangafodipir trisodium. *Acta Radiol* 1997; 38, 780-9.

105. Toft K, Friisk G, Skotland T. Mangafodipir trisodium injection, a new contrast medium for magnetic resonance imaging: detection and quantitation of the parent compound MnDPDP and metabolites in human plasma by high performance liquid chromatography. *J Pharm Biomed Anal* 1997; 15, 973-81.

106. Toft KG, Hustvedt SO, Grant D, Martinsen I, Gordon PB, Friisk GA *et al.*. Metabolism and pharmacokinetics of MnDPDP in man. *Acta Radiol* 1997; 38, 677-89.

107. Tofts PS, Brix G, Buckley DL, Evelhoch JL, Henderson E, Knopp MV *et al.*. Estimating kinetic parameters from dynamic contrast-enhanced T_1-weighted MRI of a diffusable tracer: standardized quantities and symbols. *J Magn Reson Imaging* 1999; 10(3), 223-32.

108. Van der Elst L, Colet JM, Muller RN. Spectroscopic and metabolic effects of $MnCl_2$ and MnDPDP on the isolated and perfused rat heart. *Invest Radiol* 1997; 32(10), 581-8.

109. Wacker CM, Wiesmann F, Bock M, Jakob P, Sandstede JJW, Lehning A *et al.*. Determination of regional blood volume and intra-extracapillary water exchange in human myocardium using Feruglose: First clinical results in patients with coronary artery disease. *Magn Reson Med* 2002; 47(5), 1013-6.

110. Ward K, Schussheim AE, Balaban RS. Contribution of mitochondria to cardiac muscle water/macromolecule proton magnetization transfer. *Magn Reson Med* 2003; 50(6), 1312-6.

111. Wendland MF, Saeed M, Bremerich J, Arheden H, Higgins CB. Thallium-like test for myocardial viability with MnDPDP-enhanced MRI. *Acad Radiol* 2002; 9(1), 82-3.

112. Winkler H, Mitchel S. Exchange processes in nmr. *Adv Colloid Interface Sci* 1985; 23, 149-77.

113. Woessner DE. Nuclear transfer effects in nuclear magnetic resonance pulse experiments. *J Chem Phys* 1961; 35, 41-8.

114. Yankeelov TE, Rooney WD, Li X, Springer Jr CS. Variation of the relaxographic "shutter-speed" for transcytolemmal water exchange affects the CR bolus-tracking curve shape. *Magn Reson Med* 2003; 50(6), 1151-69.

115. Zimmerman JR, Brittin WE. Nuclear magnetic resonance studies in multiple phase systems: Lifetime of a water molecule in an absorbing phase on silica gel. *Adv Colloid Interface Sci* 1957; 61, 1328-33.

116. Zuo CS, Seoane P, Lanigan T, Harnish P, Prasad PV, Storey P *et al.*. T_1 efficacy of EVP-ABD: a potential manganese-based MR contrast agent for hepatic vascular and tissue phase imaging. *J Magn Reson Imaging* 2002; 16(6), 668-75.

Paper I

Nordhøy, Wibeke ; Anthonsen, Henrik W ; Bruvold, Morten ; Jynge, Per ; Krane, Jostein ; Brurok, Heidi: Manganese as intracellular contrast agents: proton relaxation and calcium interactions in rat myocardium. *NMR in biomedicine*, 16(2003), 82-95

Paper II

Nordhøy, Wibeke ; Anthonsen, Henrik W ; Bruvold, Morten ; Brurok, Heidi ; Skarra, Sissel ; Krane, Jostein ; Jynge, Per: Intracellular manganese ions provide strong T1 relaxation in rat myocardium. *MRM*, 52(2004), 506-514

Paper III

Manganese-calcium interactions with contrast media for cardiac MRI: A study of manganese chloride supplemented with calcium gluconate in isolated guinea pig hearts.

Morten Bruvold MSc*†, Wibeke Nordhøy MSc*†, Henrik W. Anthonsen PhD, Heidi Brurok PhD*, Per Jynge PhD MD*.**

* Department of Circulation and Medical Imaging, Faculty of Medicine, Norwegian University of Science and Technology, Medisinsk Teknisk Forskningssenter, N-7489 Trondheim, Norway.

** Department of Chemistry, Faculty of Natural Sciences and Technology, Norwegian University of Science and Technology, Høgskoleringen 5, Realfagsbygget, N-7491 Trondheim, Norway.

† These two main authors have contributed equally to the study.

Correspondence and request for reprints to:
Professor Per Jynge
Department of Circulation and Medical Imaging
Faculty of Medicine
Norwegian University of Science and Technology
Medisinsk Teknisk Forskningssenter
N-7489 Trondheim
Tel: +4773598809
Fax: +4773598613
E-mail: per.jynge@medisin.ntnu.no

Acknowledgements

The support by The Research Council of Norway, The Research Council for Cardiovascular Disease and Amersham Health are greatfully acknowledged.